

STRUCTURAL ANALYSIS OF IMPLANTABLE BIOMEDICAL
HEART ASSIST DEVICE FIXATION

A DISSERTATION
SUBMITTED TO THE FACULTY OF
UNIVERSITY OF MINNESOTA
BY

Thomas James Conway

IN PARTIAL FULFILLMENT OF THE REQUIREMENTS
FOR THE DEGREE OF
DOCTOR OF PHILOSOPHY

Ephraim M. Sparrow, Adviser

December 2013

© Thomas James Conway 2013

Acknowledgements

I have been blessed to know and work with Professor Eph Sparrow, my adviser, for many years. His heart and hard work have no bounds.

I would also like to thank my family and friends for their great support and understanding.

Dedication

I dedicate my dissertation to my Dad.

Abstract

This thesis presents how experimentation, numerical simulation, optimization, and mathematical analysis, can be applied to study and improve the fixation of left-ventricle leads within a cardiac vein. Left-ventricle cardiac leads for implantable pacemakers can lose fixation within a cardiac vein and dislodge. A common lead-fixation mechanism for left-ventricle leads was investigated that used a two- or three-dimensional shape at the distal end. The lead and the distal end are constructed from a metal coil that is pre-formed into a two- or three-dimensional shape.

Analytical beam approximations of a coil were developed to determine how coil stiffness is affected by coil geometry and material. In-vitro experimentation with a radial force tester was used to measure the overall force between a two- or three-dimensional distal shape within a straight cylindrical tube. Data processing techniques using a moving average were applied to interpret the force data. Numerical simulation using a beam approximation for the coil determined the overall force between a distal shape and a straight cylindrical tube. The distribution of force along the distal shape, including tip force was also obtained from the simulation. The simulation models were validated with experimental data. Using numerical simulation, the model of the distal shape was changed to a spiral shape and then optimized. Since actual cardiac veins are curved, the simulation model was updated with a curved tube to determine how the distal shapes would perform. A mathematical analysis using engineering principles was also applied to obtain a simple analytical equation relating a deformed distal shape to force.

Table of Contents

List of Tables.....	vii
List of Figures	ix
Chapter 1 Introduction	1
1.1 Motivation	1
1.2 Implantable Pacemaker Systems	2
1.3 Disease States	4
1.3.1 Bradyarrhythmia.....	4
1.3.2 Tachyarrhythmia	4
1.3.3 Heart Failure.....	5
1.4 Implantable Cardiac Lead Construction.....	6
1.5 Left Ventricle Lead Distal End	7
1.6 Thesis Plan	8
Chapter 2 Analytical Beam Approximation Of A Coil.....	11
2.1 Introduction	11
2.2 Elastic Bending Stiffness Calculation	13
2.3 Elastic Torsional Stiffness Calculation	21
2.4 Elastic Axial Stiffness Calculation.....	24
2.5 Elastic Stiffness Summary and Comparison	28
Chapter 3 Radial Force Experimentation Implementation And Results	30
3.1 Introduction	30
3.2 Distal Lead Samples.....	32
3.2.1 Elastic Coil Stiffness	33
3.2.2 Distal Two-Dimensional Pre-Formed Shape.....	35
3.3 Experimentation Procedure	36
3.3.1 Tare (Empty) Force Measurement Before And After Experimentation.....	36
3.3.2 Sample Setup.....	36
3.3.3 Experimental Procedure	37
3.4 Results	40
3.4.1 Tare or Empty Radial Tester Forces.....	40

3.4.2	Sample Data	43
3.4.3	Data Analysis	47
Chapter 4	Use of Experimental Results for Numerical Model Validation.....	50
4.1	Introduction	50
4.2	Distal Lead Shape Model	53
4.3	Boundary and Loading Conditions.....	56
4.4	Mesh Refinement Evaluation	58
4.4.1	Mesh Background Information.....	58
4.4.2	Mesh Refinement Results.....	59
4.5	Friction Evaluation	62
4.5.1	Friction Background Information.....	62
4.5.2	Friction Results.....	63
4.6	Proximal Straight-End Length Evaluation	67
4.6.1	Proximal Straight-End Length Background	67
4.6.2	Proximal Straight-End Length Results.....	68
4.7	Experimental Validation of Simulation Model	70
4.7.1	Experimental Validation Background	70
4.7.2	Experimental Validation of Simulation Model Results.....	71
4.7.3	Simulation Model Updated with Friction.....	82
4.7.4	Simulation Model Results with Friction.....	83
4.8	Simulation Model for Spiral Evaluation	85
4.8.1	Simulation Model for Spiral Evaluation Background	85
4.8.2	Simulation Model for Spiral Evaluation Results.....	88
4.9	Spiral Shape DOE	93
4.9.1	Spiral Shape DOE Background.....	93
4.9.2	Spiral Shape DOE Results.....	95
4.10	Summary	106
Chapter 5	Numerical Simulation Model of Curved Blood Vessels	112
5.1	Introduction	112
5.2	Curved Tube Background	112

5.3	Curved Tube Results	114
5.4	Summary	122
Chapter 6	Analytical Approximation for Fixation Force	124
6.1	Introduction	124
6.2	Analytical Derivation	125
6.3	Comparison of Analytical and Simulation Model	128
6.4	Comparison of Models	130
Chapter 7	Concluding Remarks	132
7.1	Introduction	132
7.2	Analytical Beam Approximation of a Coil	133
7.3	Experimentation	133
7.4	Numerical Simulation	134
7.5	Numerical Simulation Validation with Experiments	135
7.6	Numerical Simulation of a Spiral Distal Shape	136
7.7	Mathematical Analysis	138
7.8	Conclusion	139
Bibliography	140
Appendix	146

LIST OF TABLES

Table 2-1 Analytically Derived Equivalent Stiffnesses for a Coil	28
Table 2-2 Equivalent Elastic Beam Properties	28
Table 2-3 Material Properties for Simulation Models.....	29
Table 3-1 MP35N Material Properties	33
Table 3-2 Coil Design Parameters.....	34
Table 3-3 Bending Stiffness of Coil Designs	35
Table 3-4 Radial Force Average Comparison at Given Tube Diameter (Experiment)	49
Table 3-5 Coil Design Comparison with Coil Stiffness and Radial Force.....	49
Table 4-1 Coil Geometry.....	55
Table 4-2 Material Properties for Simulation Models.....	55
Table 4-3 Change In Elastic Modulus among Coil Designs	55
Table 4-4 Mesh Refinement Results	59
Table 4-5 Friction Evaluation Results.....	64
Table 4-6 Proximal Straight-End Length Results	68
Table 4-7 Total Radial Force – Coil Design vs. Tube Diameter.....	73
Table 4-8 Maximum Radial Force (Distal Tip) – Coil Design vs. Tube Diameter	74
Table 4-9 Axial Tube Length of Contact – Coil Design vs. Tube Diameter.....	77
Table 4-10 Total Radial Force Simulation Model vs. Experimental Average (Coil A).....	80
Table 4-11 Total Radial Force Simulation Model vs. Experimental Average (Coil B).....	81
Table 4-12 Total Radial Force Simulation Model vs. Experimental Average (Coil C).....	81
Table 4-13 Total Radial Force with Simulation Model Updated with Friction (Coil A)	83
Table 4-14 Geometry of Distal Shape	87
Table 4-15 Total Radial Force Comparison between Circular and Spiral Distal Shape	90
Table 4-16 Axial Tube Length of Contact Comparison between Circular and Spiral Distal Shape	93
Table 4-17 Factors with High and Low Values.....	94
Table 4-18 Spiral Designs	95
Table 4-19 Spiral Design DOE Results.....	95
Table 4-20 Spiral Designs for Maximum Total Radial Force & Minimum Tip Force	105
Table 4-21 Locally Optimized Three-Dimensional Spiral	106
Table 4-22 Axial Tube Length of Contact for Locally Optimized Three-Dimensional Spiral	106
Table 4-23 Distal Shapes and Radial Forces (4-mm Tube)	109
Table 4-24 Axial Tube Length of Contact Comparison between Distal Shapes (4-mm Tube)	110
Table 4-25 Axial Tube Length of Contact with Percentile for Distal Shapes	110
Table 5-1 Distal Shapes.....	113
Table 5-2 Circular Distal Shape Radial Forces within Straight and Curved Tubes	117

Table 5-3 Locally Optimized Spiral Shape within Straight and Curved Tubes	120
Table 6-1 Comparison of Radial Forces from the Analytical and Simulation Models	129
Table 6-2 Comparison of Total Radial Force between Chapter 6 and Chapter 4 Models	131
Table A-1 Coil Geometry.....	147
Table A-2 Material Properties.....	147

LIST OF FIGURES

Figure 1-1 Plastic Tines on Distal Tip of Lead	6
Figure 1-2 Pre-Shaped Spiral on Distal Tip of Lead.....	6
Figure 1-3 Multi Filar Coil (Example Shows Four Filars or Wire Strands).....	6
Figure 1-4 Plastic or Rubber Tines on Distal Lead Tip.....	7
Figure 1-5 Left Ventricle Lead Pre-Shaped Distal Tip	8
Figure 2-1 Simplified Model of a Metal Coil within a Silicone Tube	11
Figure 2-2 Loading Conditions on the Coil and on the Beam.....	12
Figure 2-3 Coil Loading in Bending	14
Figure 2-4 Coil Geometry	15
Figure 2-5 Free Body Diagram of Coil Subjected to Bending Moment M	16
Figure 2-6 Moments of Inertia for Inner Core and Outer Sleeve Wire	18
Figure 2-7 Angular Deflection of a Single Coil Turn	18
Figure 2-8 Free Body Diagram of a Coil Subjected to Axial Torque T	21
Figure 2-9 Free Body Diagram of Coil Subjected to Axial Load F	25
Figure 3-1 Simplified Experimental Samples	32
Figure 3-2 Coil Design Parameters (4 Filar Shown).....	34
Figure 3-3 Coil Sample with Distal Shape for Radial Force Tester.....	35
Figure 3-4 Radial Force Tester Setup.....	37
Figure 3-5 Contraction and Expansion of a Single Cycle	37
Figure 3-6 Radial Force Test Cycle vs. Time – Startup Cycle Highlighted.....	39
Figure 3-7 Average Radial Forces (Before and After) in Empty Tester	41
Figure 3-8 Tare (or Empty) Force Measurement (Before and After).....	42
Figure 3-9 Sample Measurement Corrected by Subtracting the Tare Force	42
Figure 3-10 Coil A Force Measurements	44
Figure 3-11 All Three Samples Averaged (Moving Average with All Cycles Combined)	44
Figure 3-12 All Three Samples Averaged with Tare (Empty) Forces Subtracted	44
Figure 3-13 Coil B Force Measurements	45
Figure 3-14 All Three Samples Averaged (Moving Average with All Cycles Combined)	45
Figure 3-15 All Three Samples Averaged with Tare (Empty) Forces Subtracted	45
Figure 3-16 Coil C Force Measurements	46
Figure 3-17 All Three Samples Averaged (Moving Average with All Cycles Combined)	46
Figure 3-18 All Three Samples Averaged with Tare (Empty) Forces Subtracted	46
Figure 3-19 Coil Designs (Contraction and Expansion)	47
Figure 3-20 Coil A Radial Force and Average.....	48
Figure 3-21 Coil B Radial Force and Average.....	48
Figure 3-22 Coil C Radial Force and Average.....	48
Figure 4-1 Flowchart of Numerical Simulation	52

Figure 4-2 Comparison of Simplified Experimental Samples (Top) to Computer Model (Bottom)	54
Figure 4-3 Simulation Model Geometry (Side & Isometric View).....	56
Figure 4-4 Initial State, Step 1, Step 2	57
Figure 4-5 Comparison of Radial Forces with Global Element Size	60
Figure 4-6 Deformed Distal Shape with Contact Forces – Coil A (2-mm Diameter Tube).....	61
Figure 4-7 Radial Force Distribution along the Axial Direction (Mesh Refinement).....	62
Figure 4-8 Comparison of Radial Forces for Different Coefficients of Friction.....	64
Figure 4-9 Deformed Distal Shape with Contact Forces for Coil A (6 -mm Diameter Tube). 65	
Figure 4-10 Radial Force Distribution along the Axial Direction with and without Friction ..	66
Figure 4-11 Comparison of Distal-End Radial Forces with Proximal Straight-End Length....	69
Figure 4-12 Radial Force Distribution along the Axial Direction for Parametric Values of the Proximal Straight-End Length.....	70
Figure 4-13 Deformed Distal Shape for Various Tube Diameters (Coil A)	72
Figure 4-14 Comparison of Total Radial Force with Coil Design and Tube Diameter	74
Figure 4-15 Comparison of Maximum Radial Force with Coil Design and Tube Diameter ...	75
Figure 4-16 Radial Force Distribution along the Axial Direction (Coil A)	76
Figure 4-17 Total Radial Force Simulation Model and Experimental (Coil A).....	77
Figure 4-18 Total Radial Force Simulation Model and Experimental (Coil B).....	78
Figure 4-19 Total Radial Force Simulation Model and Experimental (Coil C).....	78
Figure 4-20 Total Radial Force Simulation Model and Experimental Average (Coil A)	79
Figure 4-21 Total Radial Force Simulation Model and Experimental Average (Coil B)	80
Figure 4-22 Total Radial Force Simulation Model and Experimental Average (Coil C)	80
Figure 4-23 Total Radial Force Simulation Model with Friction and Experimental Average. 84	
Figure 4-24 Deformed Distal Shape for Various Coefficients of Friction (Coil A).....	85
Figure 4-25 Helix Geometry	86
Figure 4-26 Initial Distal Shape	88
Figure 4-27 Deformed Spiral Distal Shape for Various Tube Diameters (Coil A).....	89
Figure 4-28 Comparison of Total Radial Force between Circular and Spiral Distal Shape.....	90
Figure 4-29 Radial Force Distribution along the Axial Direction (Coil A)	92
Figure 4-30 Spiral Distal Shape Representation with Distal Length.....	94
Figure 4-31 Cube Plot for DOE Results in a 4-mm Diameter Tube	96
Figure 4-32 Pareto Chart of Effects for Total Radial Force.....	97
Figure 4-33 Main Effects Plot of Total Radial Force with Center Points	98
Figure 4-34 Interaction Plot of Total Radial Force with Center Points.....	99
Figure 4-35 Contour Plot for Total Radial Force with Radius Held Constant at 4 mm	100
Figure 4-36 Pareto Chart of Effects for Radial Tip Force.....	101
Figure 4-37 Main Effects Plot of Radial Tip Force with Center Points	102
Figure 4-38 Interaction Plot of Radial Tip Force with Center Points	103
Figure 4-39 Contour Plot for Radial Tip Force with Pitch Held Constant at 4-mm	104

Figure 4-40 Progression of Distal Shape to Maximize Total Radial Force and Minimize Tip Force.....	107
Figure 4-41 Radial Force Distribution along the Axial Direction for Distal Shapes	108
Figure 4-42 Comparison of Radial Forces between Distal Designs.....	109
Figure 5-1 Deformed Distal Shapes Inside 4-mm Diameter Tube with a 6-cm Diameter Curvature.....	115
Figure 5-2 Deformed Distal Shapes Inside 4-mm Diameter Tube with a 9-cm Diameter Curvature.....	116
Figure 5-3 Comparison of Circular Distal Shape Radial Forces For Curved and Straight Tubes	117
Figure 5-4 Radial Force Distribution along the Axial Direction for a Circular Distal Shape (4-mm Tube)	119
Figure 5-5 Comparison of Spiral Distal Shape Radial Forces for Curved and Straight Tubes	120
Figure 5-6 Radial Force Distribution along the Axial Direction for a Spiral Distal Shape (4-mm Tube)	122
Figure 6-1 Axial View of Coil Before and After Radially Compression	126
Figure 6-2 Comparison of Radial Force between Analytical and Simulation Model	129

CHAPTER 1

INTRODUCTION

1.1 MOTIVATION

Cardiac resynchronization therapy (CRT) is an effective treatment for patients with moderate to severe heart failure (HF). This treatment involves implanting a pacemaker with a lead fixated to the heart. CRT prolongs patient survival and improves the quality of life [1]. These benefits depend on the proper implantation and fixation of the left ventricle lead to stay in place to deliver effective and uninterrupted resynchronization. The recommended position for the left ventricle (LV) lead is outside the left ventricle in lateral or posterolateral cardiac veins. Clinical practice is a transvenous LV lead implantation through a side branch of the coronary sinus (CS) [2]. Dislodgement of LV pacing leads is a common clinical complication requiring an additional surgery for lead repositioning with concomitant surgical risks. The acute dislodgment rate is 5.4% [3], while the chronic dislodgement rate is 8.6% [4]. To reduce dislodgements, a structural analysis of cardiac lead fixation will be performed in this thesis. The distal fixation will be evaluated by a method of experimentation, computer simulation, and an analytical first principles model.

There is a clear need for this work analyzing lead fixation based upon review of current literature. The implantation of cardiac pacemakers and leads can be traced back to the 1950's. For the next several decades, structural analysis of the cardiac leads involved examining the stress and fatigue of the metal components [5 – 10]. The structural analysis of

the lead fixation or attachment to the heart has been limited. Recently this has been examined [11 – 13] but this has been limited to forces exerted on straight leads wedged into veins. The use of a stent for fixation has been examined as well but then lead extraction could be difficult [14]. The current LV leads have been designed to incorporate two- or three-dimensional shaped distal ends [15]. These shapes allow the lead to spring back against the heart and vessel wall at any location in the vein.

In this thesis, the fixation force of an implantable cardiac lead within a cardiac vein outside the left ventricle will be examined. This distal end fixation force or resistance to movement within the vein keeps the electrodes in place against the heart and prevents dislodgements of the distal electrodes. Lead dislodgements and poor electrode contact can interrupt or reduce the effectiveness of therapy from implantable cardiac pacemakers for patients with heart failure disease over the device lifespan within a patient [16]. Specifically, the two- or three-dimensional pre-shaped distal end will be examined to determine the forces the lead exerts on the vein wall to keep it in position.

There are two main objectives. One is to determine a geometric distal shape with the highest fixation forces to reduce lead dislodgements. The second is to minimize the contact force at the tip of the lead to reduce potential damage to the heart wall or vein.

1.2 IMPLANTABLE PACEMAKER SYSTEMS

An implantable pacemaker system consists of a pulse generator that is connected to the heart by leads that deliver electrical signals to the heart. An implantable pacemaker is a computer

with an electrical pulse generator and battery that sends and receives electrical signals from the heart along a lead. Due to the beating of the heart, the leads are in constant motion with the heart. Typically the lifespan of a pacemaker system is five to ten years [17 – 19]. On average, the heart contracts seventy beats per minute with a maximum of over two hundred beats per minute [20]. The lead flexes and bends with each beat of the heart so fixation against the heart is important to maintain therapy to the patient.

The proximal end of the lead connects [21] to an implantable pacemaker and transmits electrical impulses to and from the heart through electrodes on the distal end of the lead. These distal electrodes are held in contact with the heart wall via a fixation mechanism or force. Fixation of the lead guarantees constant transmission of these electrical pulses and proper operation of the implantable pacemaker providing the patient with cardiac synchrony, proper heart rate, and improved cardiac output.

A pacemaker is implanted if a patient's heart can no longer properly control the pumping of blood. Many factors can cause this to occur; genetic disorder, heart attack, age, etc. [22, 23]. These devices are typically characterized into three groups respectively corresponding to the specific disease states; bradyarrhythmia, tachyarrhythmia, and heart failure.

Depending upon the disease state being treated, the implantable pacemaker system can consist of a pulse generator and multiple leads, varying from one to three. Some systems only have one lead that connects to the right atrium or right ventricle. Others will have two leads that connect to both the right atrium and right ventricle [24]. Systems used to treat heart failure can have three leads connecting to the right atrium, right ventricle, and left ventricle [25].

The fixation mechanism of the lead to the heart differs depending upon the location of the lead. The left ventricle lead has higher dislodgement rates compared to the leads in the right atrium and right ventricle [16]. This thesis examines the fixation with the heart that is used by the left ventricle lead.

1.3 DISEASE STATES

1.3.1 BRADYARRHYTHMIA

Bradycardia is a condition when the heart beats too slowly. The pacemaker senses this slow rhythm and sends electrical signals that make the heart beat faster. One or two leads are implanted for this system.

The distal tip of the cardiac lead delivers these electrical signals inside the right atrium and/or right ventricle. The distal fixation mechanism is typically a metal threaded screw that screws into the heart wall of the right atrium or right ventricle [26]. Another distal fixation method is plastic tines that hook into the trabecular heart tissue in the apex of the right ventricle [27].

1.3.2 TACHYARRHYTHMIA

Tachycardia is a condition when the heart beats too fast. The pacemaker senses this fast rhythm and sends electrical signals to the heart that attempt to make the heart beat slower. If the pacemaker cannot pace the heart out of the faster rate, the pacemaker will send an electrical shock to defibrillate the heart to cardiovert or reset the heart into a normal rhythm.

The distal tip of the cardiac lead delivers these electrical signals inside the right atrium and/or

right ventricle. Again the fixation mechanism is typically either a metal threaded screw screwed into the heart wall in the right atrium [28] or right ventricle; or plastic tines that hook into the trabecular heart tissue in the apex of the right ventricle. The distal end of the cardiac lead has an extra shocking coil in addition to the distal pacing and sensing electrodes.

1.3.3 HEART FAILURE

Heart failure is a condition that prevents the heart from pumping efficiently and is usually caused by the left ventricle not beating in synchrony with the right ventricle. This results in poor or inefficient cardiac output or blood pumping. Heart failure devices are pacemakers that treat both bradyarrhythmia and tachyarrhythmia with the additional capability to pace and sense the left ventricle. Since these devices resynchronize the left and right ventricle, it is commonly called cardiac resynchronization therapy (CRT) [29].

In addition to the leads in the right atrium and right ventricle, an additional lead is placed in a vein outside the left ventricle. This left ventricle lead is not placed inside the left ventricle but is inserted into an outside vein after guided through the coronary sinus into the great cardiac vein or other branch vein [30, 31]. The coronary sinus is on the posterior of the heart and turns into the great cardiac vein towards the apex of the heart on the anterior of the heart. The locations provide good locations for the pacing and sensing electrodes.

The fixation mechanism for the left ventricle lead is plastic tines (Figure 1-1) that wedge in the vein, or alternatively the distal end of the lead is pre-shaped (Figure 1-2) in a two- or three-dimensional shape that push against the vein and heart [32].

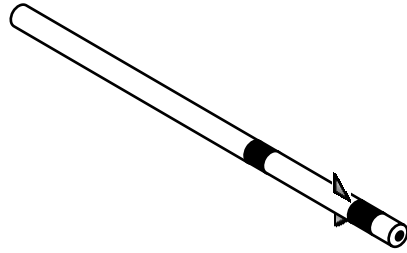


Figure 1-1 Plastic Tines on Distal Tip of Lead



Figure 1-2 Pre-Shaped Spiral on Distal Tip of Lead

This thesis examines the fixation of the left-ventricle lead when the distal end is pre-shaped (Figure 1-2) into a two- or three-dimensional shape.

1.4 IMPLANTABLE CARDIAC LEAD CONSTRUCTION

The lead body construction is typically made of coils, cables, and plastic tubing. These can be arranged in single lumen, multi-lumen, or coaxial configuration. Also the coils are typically multi-filar or made from multiple wire strands coiled together (Figure 1-3). The individual filars can be insulated and used in a co-radial design.

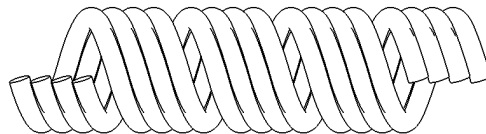


Figure 1-3 Multi Filar Coil (Example Shows Four Filars or Wire Strands)

Typical conductors used in the coils and cables are a metal Nickel-Chromium alloy wire (MP35N). The MP35N wire can have a core of silver (Ag) or Tantalum (Ta) to increase electrical conductivity [6]. The stiffness and stresses within the coils are determined by the

material and geometry of the coil including pitch, wire diameter, coil diameter, and the number of filars or wire strands wound to form the coil. The number of filars in a coil can be one or more with the limitation typically being the bending stress generated in the coil. The typical wire diameter used in a coil varies from 0.0254- to 0.254-mm. Surrounding the coils is a silicone or polyurethane tubing that has an inside diameter that ranges from 0.762- to 1.524-mm with wall thickness from 0.127- to 0.254-mm.

1.5 LEFT VENTRICLE LEAD DISTAL END

For left-ventricle leads, the distal end in contact with the heart can have plastic or rubber tines (Figure 1-4) that wedge into the vein against the heart. The distal end contains the electrodes that are connected to the coil or cables. Typically the use of tines on the distal end only allows the lead tip to be positioned and wedged into the end of a vein. This only allows the left ventricle lead to be positioned in only one location at the end of the vein.

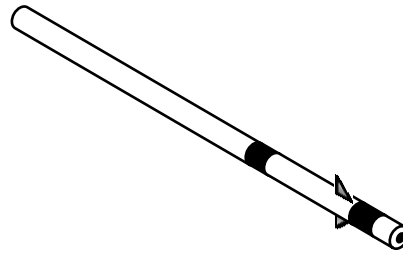


Figure 1-4 Plastic or Rubber Tines on Distal Lead Tip

Left-ventricle leads can also use a pre-shaped two- or three-dimensional distal tip (Figure 1-5) to allow the lead and electrodes to wedge against heart in the vessel [33]. The use of a pre-shaped distal tip allows the left-ventricle lead to be positioned at any location along the vein.

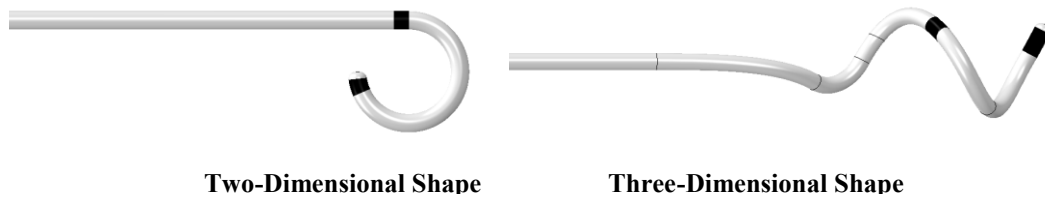


Figure 1-5 Left Ventricle Lead Pre-Shaped Distal Tip

The coil inside the left-ventricle lead allows a guidewire or stylet to be inserted into the coil to guide the lead into the coronary sinus and great cardiac vein via fluoroscopy. As a guidewire or stylet is inserted, the two- or three-dimensional shape of the distal end straightens out.

The straightened lead can then be guided to the targeted vein outside the left ventricle and once in the proper vessel location for sensing and pacing, the guide wire or stylet is removed. The distal end then tries to revert back to its two- or three-dimensional shape but is prevented by the vessel and cardiac wall. The distal shape pushes against the vessel and heart to fixate the lead at this location. This distal fixation provides electrode contact with the heart for sensing and pacing.

1.6 THESIS PLAN

The two- and three-dimensional shape of the distal tip of the left-ventricle lead will be examined to determine how this shape influences contact forces between the lead and the vessel/heart wall. This examination will use numerical simulation to understand the forces occurring at the distal end of the lead. Validating the simulation models will be accomplished with experimentation and analytical solutions of simpler boundary conditions.

The left-ventricle leads investigated are constructed of coils, and in Chapter 2 an analytical derivation of the bending, torsional, and axial elastic stiffness of coils will be presented to provide a comparison between coil designs. This analytical derivation of the stiffnesses will also allow simulation models to be constructed to examine various geometric distal shapes and the radial forces that they generate.

In Chapter 3, *in-vitro* experimentation with a radial force tester and samples will provide data on the overall radial force for a given tube diameter size. Samples of different stiffness will be used to determine how lead stiffness affects radial force. The limitation with experimentation will be that only an overall radial force can be obtained for each sample. The instrumentation also only allows straight rigid cylindrical tubes to be examined.

Numerical simulation used to replicate the experimentation from Chapter 3 will be explained in Chapter 4. The simulation models the interaction of the samples with a straight rigid cylindrical tube. These simulation models give an overall radial force that was measured experimentally. This overall force allows validation of the simulation model. This validation compares the absolute radial forces between the model and experimentation. The relationship between radial forces and stiffness will also be investigated. The benefit of the numerical simulation over experimentation is that the model can report radial forces along the entire distal end of the sample including the tip force.

Since left-ventricle leads are inserted into curved blood vessels that wrap around the heart, curvature is added to the numerical simulation in Chapter 5. The simulation model will show the interaction of the samples with a curved rigid tube. The curvature chosen is explained and

results presented. The addition of curvature makes experimentation very difficult or impossible.

Chapter 6 will show a mathematical or analytical analysis based upon engineering principles to derive the fixation force of the distal lead shape that is inserted into a rigid cylindrical tube. This analysis will include a derivation of the analytical representation or equations used to calculate lead fixation forces within a straight rigid cylindrical tube. Concluding remarks will follow in Chapter 7.

CHAPTER 2

ANALYTICAL BEAM APPROXIMATION OF A COIL

2.1 INTRODUCTION

For numerical simulation of the leads, simplified models will be used that have their stiffness derived analytically. The simplification will replace the three-dimensional complexity of a coil and tubing with an equivalent stiffness in a one-dimensional beam element. These equivalent stiffnesses can be measured experimental or analytically calculated. The analytical approach is what follows.

The simplest representation of a lead is a metal coil within a silicone tube (Figure 2-1) with the distal end of the coil pre-formed into a two- or three-dimensional shape for fixation.

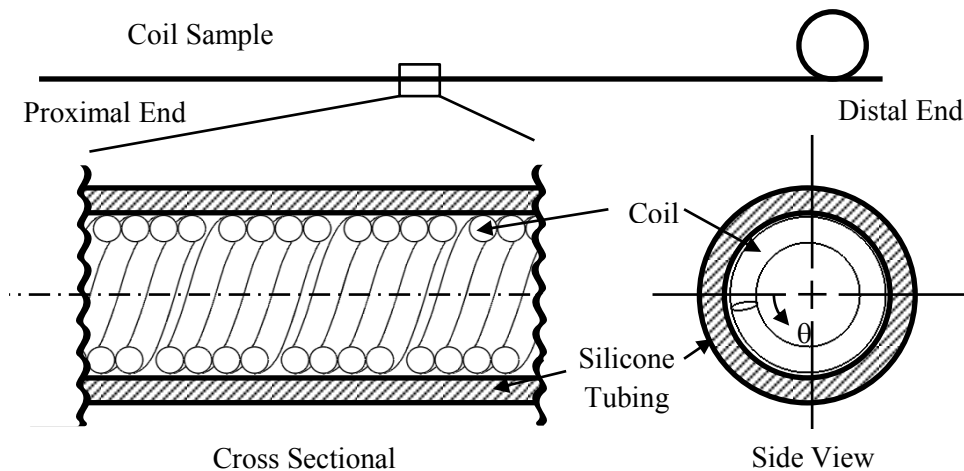


Figure 2-1 Simplified Model of a Metal Coil within a Silicone Tube

This metal coil has elastic bending, torsional, and axial stiffnesses that are dependent upon coil material and geometry. These elastic stiffnesses can be calculated analytically and compared for various coil designs. Numerical simulation is also simplified by using beam elements that have these stiffness characteristics. Detail simulation models of the coils are avoided resulting in smaller models and faster analysis times.

Figure 2-2 shows the three loading conditions (bending, torsional, and axial) that the coil can undergo. A simple beam with the same elastic stiffness characteristics can then represent the coil to determine fixation forces in a simulation model. Loading is assumed to occur in the elastic range and permanent deformation does not occur. For convenience, the beam representation will be assumed circular with a diameter D_{beam} equal to the mean diameter of the coil D_{mean} and the length L_{beam} is the same as that of the coil L_{coil} .

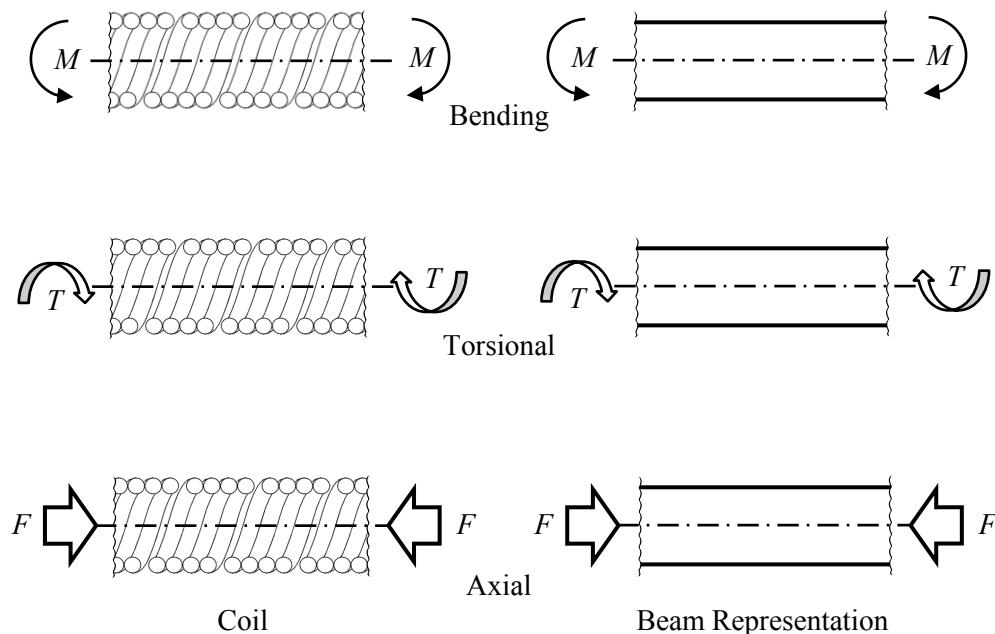


Figure 2-2 Loading Conditions on the Coil and on the Beam

Structurally, the lead is essentially a metal coil with the distal end of the coil pre-formed into a two- or three-dimensional shape for fixation. The lead is straightened by sliding a guidewire into the coil and then inserting it into a vein. Fixation against the cardiac vein occurs when the straightened distal end tries to revert back to its two- or three-dimensional shape but is prevented from doing so by the vein. This fixation generates bending and torsional loads on the lead as the lead pushes and twists against the vein. Axial loading is minimal. Since the loading is mainly bending and torsional, only the stiffnesses related to them will be used in the subsequent numerical simulation. An equivalent modulus of elasticity E_{beam} and shear modulus G_{beam} will be determined. Poisson's ratio ν is the ratio of transverse to axial strain and can be determined from the modulus of elasticity E_{beam} and shear modulus G_{beam} for a material ($E_{beam} = 2(1 + \nu)G_{beam}$).

These equivalent stiffnesses are calculated using strain energy and Castigliano's theorem [34]. The strain energy for a coil can be determined by integrating the applied load (bending moment, torque, or axial force on the ends of the coil) along the path of the coil. The bending moment M is applied perpendicular to the coil axis to induce bending. M varies with the angle θ around the coil axis. For the torque T and axial force W the corresponding loading does not vary with the angle θ around the coil axis.

2.2 ELASTIC BENDING STIFFNESS CALCULATION

The elastic bending stiffness of a coil can be calculated from the coil geometry and material properties. When a coil has a bending moment M applied to an axis perpendicular to the coil axis (Figure 2-3) the elastic bending stiffness of the coil can be calculated [5]. The Meagher

and Altman paper present the derivation for determining the stress within a coil undergoing bending. As part of their derivation the elastic bending stiffness is obtained. Their derivation of the elastic bending stiffness is presented in this section. The stress derivation is not shown but can be referenced in their paper [5, 6, and 10]. Their derivation assumes that the wire consists of two materials, a core material surrounded by a tubular jacket or sleeve material (Figure 2-4). For the work presented subsequently only a wire consisting of a single wire will be used, so their derivation will be simplified.

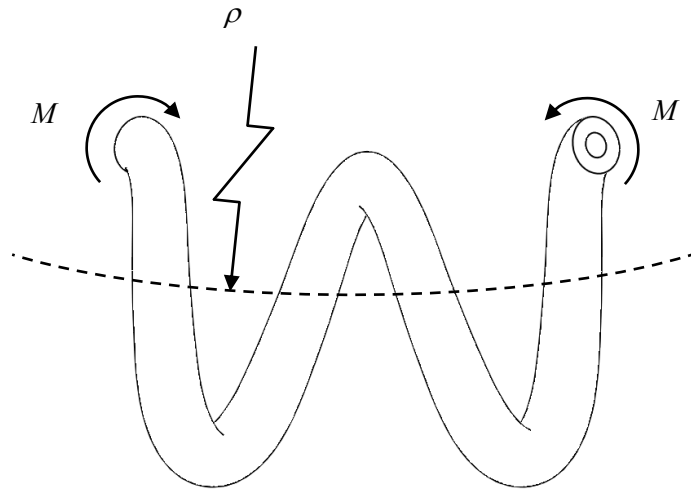


Figure 2-3 Coil Loading in Bending

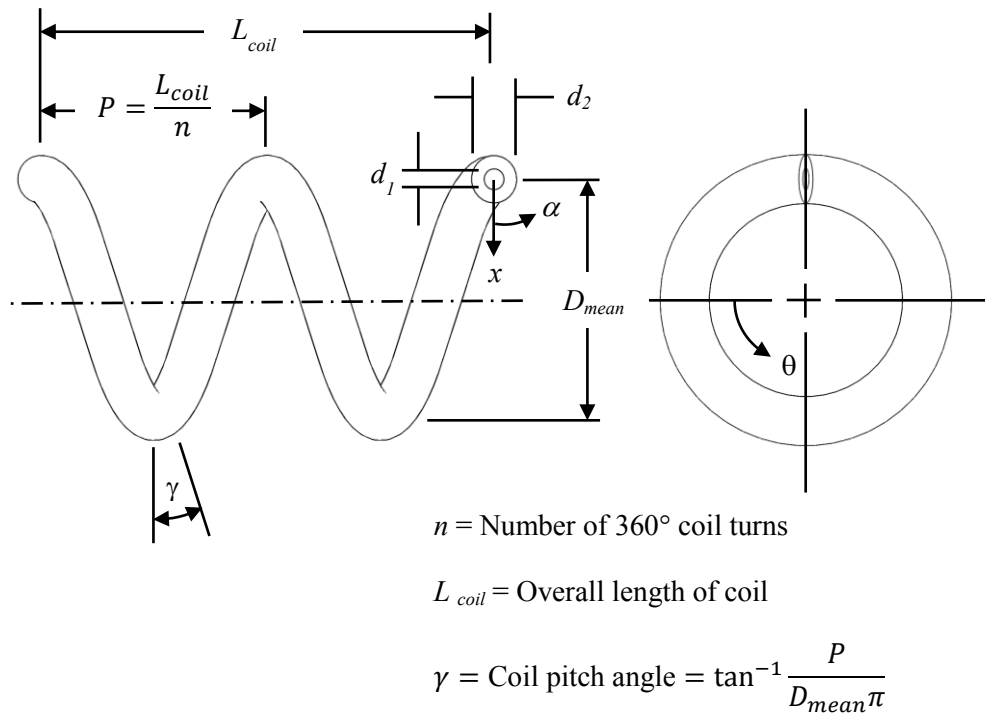


Figure 2-4 Coil Geometry

The Meagher and Altman paper [5] show how using a free body diagram (Figure 2-5), the loading condition on the coil can be resolved into internal loads at any cross section perpendicular to the wire axis. The applied bending moment M can be resolved into a torsional load T_θ and two bending moments M_R , M_Z . The torsion about the wire axis T_θ is perpendicular to the wire cross section. The bending moment M_R axis lies within this plane while the other bending moment M_Z axis lies about the third orthogonal axis within this cross section. The angle θ is measured in the plane perpendicular to the coil axis, angle γ is the coil pitch angle, and n is the number of coil turns (Figure 2-4) along the entire length of the coil L_{coil} .

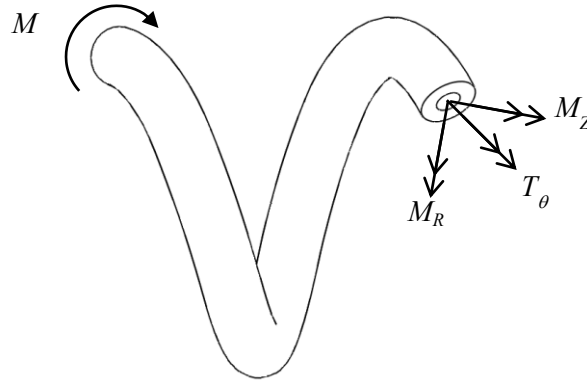


Figure 2-5 Free Body Diagram of Coil Subjected to Bending Moment M

The coil-pitch angle is given by

$$\gamma = \tan^{-1} \frac{P}{D_{mean}\pi} \quad (2-1)$$

Meagher and Altman [5] show how the applied bending moment M can be transformed into resultant loads at any coil cross section location by Eq. (2-2). These resultant loads change with the coil cross section around the axis of the coil θ .

$$T_{\theta} = M \sin \theta \cos \gamma \quad M_R = M \cos \theta \quad M_Z = M \sin \gamma \sin \theta \quad (2-2)$$

Meagher and Altman [5] describe how the fraction of total internal torque T_T or the moment M_T at the cross-section supported by the inner core or outer sleeve is determined using beam approximations for composite beams [35] and is shown in Eq. (2-3) and Eq.(2-4). Then, equilibrium of loads and compatibility of displacement is used to determine the torque and moment on the core (T_1, M_1) and on the outer sleeve (T_2, M_2).

$$T_1 = T_T \left(\frac{G_1 J_1}{G_1 J_1 + G_2 J_2} \right) \quad T_2 = T_T \left(\frac{G_2 J_2}{G_1 J_1 + G_2 J_2} \right) \quad (2-3)$$

$$M_1 = M_T \left(\frac{E_1 I_1}{E_1 I_1 + E_2 I_2} \right) \quad M_2 = M_T \left(\frac{E_2 I_2}{E_1 I_1 + E_2 I_2} \right) \quad (2-4)$$

As shown in Meagher and Altman paper [5] the bending and torsion on the core and outer sleeve are expressed as functions of the area moment of inertia I , shear modulus G , modulus of elasticity E , and polar area moment of inertia J .

$$M_{R1} = M \cos \theta \left(\frac{E_1 I_1}{E_1 I_1 + E_2 I_2} \right) \quad (2-5a)$$

$$M_{R2} = M \cos \theta \left(\frac{E_2 I_2}{E_1 I_1 + E_2 I_2} \right) \quad (2-5b)$$

$$M_{Z1} = M \sin \gamma \sin \theta \left(\frac{E_1 I_1}{E_1 I_1 + E_2 I_2} \right) \quad (2-5c)$$

$$M_{Z2} = M \sin \gamma \sin \theta \left(\frac{E_2 I_2}{E_1 I_1 + E_2 I_2} \right) \quad (2-5d)$$

$$T_{\theta 1} = M \sin \theta \cos \gamma \left(\frac{G_1 J_1}{G_1 J_1 + G_2 J_2} \right) \quad (2-5e)$$

$$T_{\theta 2} = M \sin \theta \cos \gamma \left(\frac{G_2 J_2}{G_1 J_1 + G_2 J_2} \right) \quad (2-5f)$$

Formulas for the area moment of inertia I and polar area moment of inertia J for the inner core and outer sleeve are shown in Figure 2-6 [36]. The subscripts 1 and 2 refer to the core and outer sleeve, respectively.

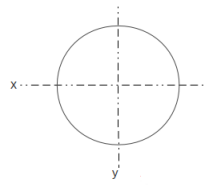
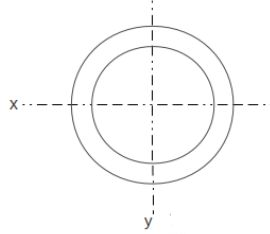
Inner Core	Outer Sleeve
	
$I_1 = I_x = I_y = \frac{\pi d_1^4}{64}$	$I_2 = I_x = I_y = \frac{\pi(d_2^4 - d_1^4)}{64}$
$J_1 = I_x + I_y$	$J_2 = I_x + I_y$

Figure 2-6 Moments of Inertia for Inner Core and Outer Sleeve Wire

Meagher and Altman use Castigliano's method [37] to determine the angular deflection λ in the plane of bending for a single turn of the coil (Figure 2-7).

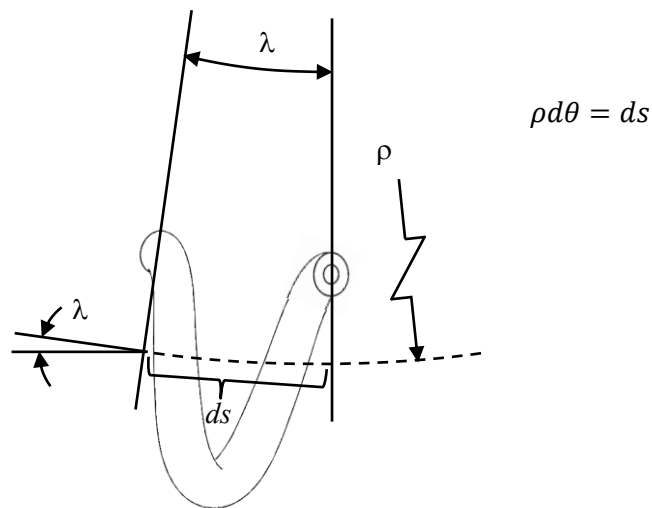


Figure 2-7 Angular Deflection of a Single Coil Turn

The six terms integrated in Eq. (2-6) by Meagher and Altman [5] result from the strain

energy due to bending about two axes and torsion about the third for the inner core and outer sleeve. The terms are integrated along one turn of a coil. Instead of integrating the angle θ from 0 to 2π radians, the equivalent integral is used with limits from 0 to $\frac{\pi}{2}$ radians and then multiplied by 4.

$$\lambda = 4 * \left[\int_0^{\pi/2} \frac{M_{Z1}R}{E_1 I_1 \cos \gamma} \frac{\partial M_{Z1}}{\partial M} d\theta + \int_0^{\pi/2} \frac{M_{Z2}R}{E_2 I_2 \cos \gamma} \frac{\partial M_{Z2}}{\partial M} d\theta + \int_0^{\pi/2} \frac{M_{R1}R}{E_1 I_1 \cos \gamma} \frac{\partial M_{R1}}{\partial M} d\theta \right. \\ \left. + \int_0^{\pi/2} \frac{M_{R2}R}{E_2 I_2 \cos \gamma} \frac{\partial M_{R2}}{\partial M} d\theta + \int_0^{\pi/2} \frac{T_{\theta 2}R}{G_1 J_1 \cos \gamma} \frac{\partial T_{\theta 1}}{\partial M} d\theta + \int_0^{\pi/2} \frac{T_{\theta 2}R}{G_2 J_2 \cos \gamma} \frac{\partial T_{\theta 2}}{\partial M} d\theta \right] \quad (2-6)$$

After integrating, Meagher and Altman [5] find the angular deflection per unit length of coil ϕ by dividing the angular deflection of one turn λ by the coil pitch (P or L_{coil}/n).

$$\phi = \frac{\lambda}{P} = \frac{\lambda n}{L_{coil}} \quad (2-7)$$

Meagher and Altman combined this expression Eq. (2-7) with the relationship Eq. (2-8) between the arc length ds and the radius of curvature of the coil ρ to obtain the curvature in terms of angular deflection λ .

$$\rho\phi = ds = 1 = \rho \frac{\lambda n}{L_{coil}} \quad (2-8)$$

$$\frac{1}{\rho} = \frac{\lambda n}{L_{coil}} \quad (2-9)$$

$$\beta = E_{beam} I_{beam} = \frac{M}{\frac{1}{\rho}} \quad (2-10)$$

Meagher and Altman [5] substitute for λ from Eq. (2-6) and rearrange which yields the elastic bending stiffness β Eq. (2-11). Again the subscripts 1 and 2 refer to the core and outer sleeve, respectively. This expression assumes the coil only has a single filar ($N=1$) or wire.

$$\beta = \frac{M}{\frac{1}{\rho}} = \frac{2(E_1 I_1 + E_2 I_2)(G_1 J_1 + G_2 J_2) P \cos \gamma}{D_{mean} \pi [(G_1 J_1 + G_2 J_2)(1 + \sin^2 \gamma) + (E_1 I_1 + E_2 I_2) \cos^2 \gamma]} \quad (2-11)$$

If the coil consists of more than one filar ($N > 1$), the elastic bending stiffness is multiplied by the number of filars N .

$$\beta = \frac{M}{\frac{1}{\rho}} = N * \frac{2(E_1 I_1 + E_2 I_2)(G_1 J_1 + G_2 J_2) P \cos \gamma}{D_{mean} \pi [(G_1 J_1 + G_2 J_2)(1 + \sin^2 \gamma) + (E_1 I_1 + E_2 I_2) \cos^2 \gamma]} \quad (2-12)$$

Having a single material for the wire filar simplifies the elastic bending stiffness β .

$$\beta = E_{beam} I_{beam}$$

$$\beta = N * \frac{2(E_{filar} I_{filar})(G_{filar} J_{filar}) P \cos \gamma}{D_{mean} \pi [(G_{filar} J_{filar})(1 + \sin^2 \gamma) + (E_{filar} I_{filar}) \cos^2 \gamma]} \quad (2-13)$$

After rearranging and using Eq. (2-1) for the coil pitch angle γ , the elastic bending stiffness for a coil undergoing bending is determined as.

$$\beta = E_{beam} I_{beam} = N * \frac{2 P \cos \gamma}{D_{mean} \pi \left[\frac{1}{E_{filar} I_{filar}} + \frac{\sin^2 \gamma}{E_{filar} I_{filar}} + \frac{\cos^2 \gamma}{G_{filar} J_{filar}} \right]}$$

$$\beta = E_{beam} I_{beam} = N * \frac{2 \tan \gamma \cos \gamma}{\left[\frac{1}{E_{filar} I_{filar}} + \frac{\sin^2 \gamma}{E_{filar} I_{filar}} + \frac{\cos^2 \gamma}{G_{filar} J_{filar}} \right]} \quad (2-14)$$

2.3 ELASTIC TORSIONAL STIFFNESS CALCULATION

The elastic torsional stiffness of a coil can be determined from the coil geometry and material properties and this derivation is covered in many machine design textbooks including the one cited by Hearn [38]. When a torque T is applied to a coil about its axis, the elastic torsional stiffness of the coil can be determined. The following derivation assumes the wire consists of a single material.

With a free body diagram, the loading condition on the coil can be resolved into internal resultant loads at any cross section perpendicular to the wire axis (Figure 2-8). Hearn [38] describes how the resultant loads can be resolved into a torsional load and a bending moment. The applied torque has a torsional component T_{AX} about the AX axis of the wire and a bending component M_{AY} about the AY axis.

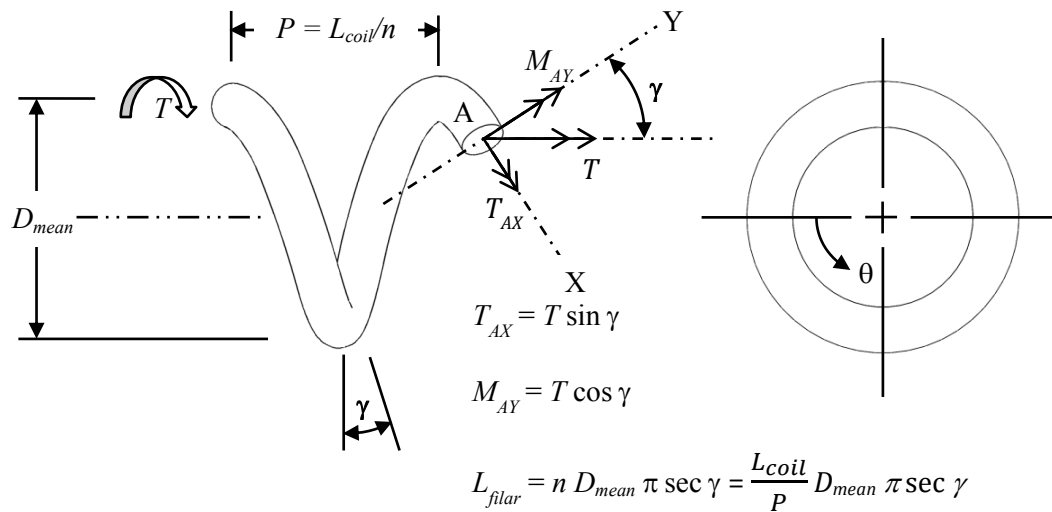


Figure 2-8 Free Body Diagram of a Coil Subjected to Axial Torque T

Hearn [38] shows how the total strain energy for this coil has two components, torsional ($T_{AX} = T \sin \gamma$) and bending ($M_{AY} = T \cos \gamma$). Substituting these relations into the strain energy equation results in Eq. (2-15).

$$\begin{aligned}
 \text{Strain Energy } U &= \frac{T_{AX}^2 L_{filar}}{2G_{filar}J_{filar}} + \frac{M_{AY}^2 L_{filar}}{2E_{filar}I_{filar}} \\
 &= \frac{L_{filar}}{2} \left[\frac{(T \sin \gamma)^2}{G_{filar}J_{filar}} + \frac{(T \cos \gamma)^2}{E_{filar}I_{filar}} \right] \\
 &= \frac{T^2 L_{filar}}{2} \left[\frac{\sin^2 \gamma}{G_{filar}J_{filar}} + \frac{\cos^2 \gamma}{E_{filar}I_{filar}} \right] \tag{2-15}
 \end{aligned}$$

The applied torque T causes the coil to rotate θ about its axis. This external work can be determined by Eq. (2-16).

$$\text{Work } W = \frac{1}{2} T \theta \tag{2-16}$$

Hearn shows that the strain energy is equal to the work W done by the torque T on the coil [38]. The angle of rotation θ about the coil axis is determined by setting Eq. (2-15) equal to Eq. (2-16).

$$\begin{aligned}
 \frac{1}{2} T \theta &= \frac{T^2 L_{filar}}{2} \left[\frac{\sin^2 \gamma}{G_{filar}J_{filar}} + \frac{\cos^2 \gamma}{E_{filar}I_{filar}} \right] \\
 \theta &= T L_{filar} \left[\frac{\sin^2 \gamma}{G_{filar}J_{filar}} + \frac{\cos^2 \gamma}{E_{filar}I_{filar}} \right] \tag{2-17}
 \end{aligned}$$

The length of the filar L_{filar} can be related to the coil pitch P , coil mean diameter D_{mean} , and the overall coil length L_{coil} .

$$L_{filar} = n D_{mean} \pi \sec \gamma = \frac{L_{coil}}{P} D_{mean} \pi \sec \gamma \quad (2-18)$$

Substituting Eq. (2-18) into Eq. (2-17) results in the angle of rotation θ about the coil axis.

$$\theta = T \frac{L_{coil}}{P} D_{mean} \pi \sec \gamma \left[\frac{\sin^2 \gamma}{G_{filar} J_{filar}} + \frac{\cos^2 \gamma}{E_{filar} I_{filar}} \right] \quad (2-19)$$

For an equivalent beam under a torsional load, the rotation θ about the axis of the beam can be determined by Eq. (2-20) with the applied torque T , material G_{beam} , beam length L_{beam} , and polar moment of inertia of beam cross section J_{beam} .

$$\theta = \frac{T L_{beam}}{G_{beam} J_{beam}} \quad (2-20)$$

Setting the rotation angle θ equal to each other for Eq. (2-19) and Eq. (2-20), the torsional stiffness for an equivalent beam can be determined that will match the coil's torsional stiffness.

$$\frac{T L_{beam}}{G_{beam} J_{beam}} = T \frac{L_{coil}}{P} D_{mean} \pi \sec \gamma \left[\frac{\sin^2 \gamma}{G_{filar} J_{filar}} + \frac{\cos^2 \gamma}{E_{filar} I_{filar}} \right] \quad (2-21)$$

After rearranging, the elastic torsional stiffness α for a coil undergoing a torque is determined.

This expression assumes the coil only has a single filar ($N=1$) or wire.

$$\alpha = G_{beam} J_{beam} = \frac{P \cos \gamma}{D_{mean} \pi \left[\frac{\sin^2 \gamma}{G_{filar} J_{filar}} + \frac{\cos^2 \gamma}{E_{filar} I_{filar}} \right]} \quad (2-22)$$

If the coil consists of more than one filar ($N>1$), the elastic torsional stiffness is multiplied by

the number of filars N .

$$\alpha = G_{beam}J_{beam} = N * \frac{P \cos \gamma}{D_{mean} \pi \left[\frac{\sin^2 \gamma}{G_{filar}J_{filar}} + \frac{\cos^2 \gamma}{E_{filar}I_{filar}} \right]} \quad (2-23)$$

After rearranging and using Eq. (2-1) for the coil pitch angle γ , the elastic torsion stiffness for a coil undergoing a torque is determined as

$$\alpha = G_{beam}J_{beam} = N * \frac{\tan \gamma \cos \gamma}{\left[\frac{\sin^2 \gamma}{G_{filar}J_{filar}} + \frac{\cos^2 \gamma}{E_{filar}I_{filar}} \right]} \quad (2-24)$$

2.4 ELASTIC AXIAL STIFFNESS CALCULATION

The elastic axial stiffness of a coil will not be used in the computer models but the derivation is shown for completeness. The elastic axial stiffness of a coil can be calculated from the coil geometry and material properties and this derivation is covered in many machine design textbooks including the one cited by Hearn [38]. When an axial load F is applied to a coil along its axis, the elastic axial stiffness of the coil can be calculated. The following derivation assumes the wire consists of a single material.

With a free body diagram, the loading condition on the coil can be resolved into internal resultant loads at any cross section perpendicular to the wire axis (Figure 2-9). Hearn [38] describes how the resultant loads can be resolved into a torsional load and a bending moment. The applied torque has a torsional component T_{AX} about the AX axis of the wire and a bending component M_{AY} about the AY axis. The shearing load of F across the wire cross section is assumed to be very small compared with the bending and torsional load and is neglected.

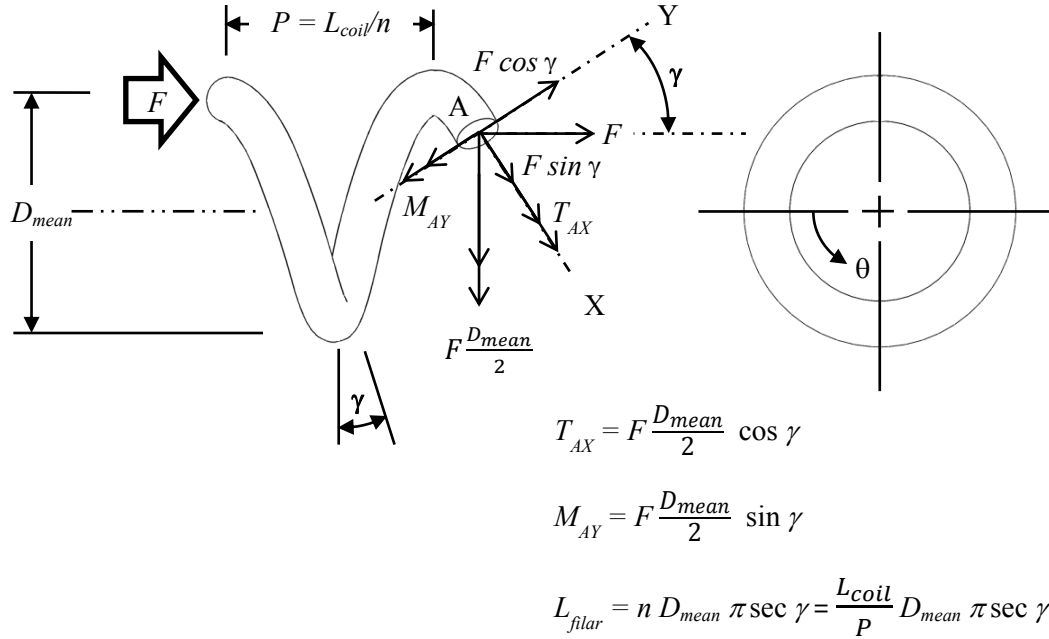


Figure 2-9 Free Body Diagram of Coil Subjected to Axial Load F

Hearn [38] shows how the strain energy for this coil has two components, torsional

($T_{AX} = F \frac{D_{mean}}{2} \cos \gamma$) and bending ($M_{AY} = F \frac{D_{mean}}{2} \sin \gamma$). Substituting these relations into

the strain energy equation results in Eq. (2-25).

$$\begin{aligned} \text{Strain Energy } U &= \frac{T_{AX}^2 L_{filar}}{2G_{filar}J_{filar}} + \frac{M_{AY}^2 L_{filar}}{2E_{filar}I_{filar}} \\ &= \frac{L_{filar}}{2} \left[\frac{\left(F \frac{D_{mean}}{2} \cos \gamma \right)^2 L_{filar}}{G_{filar}J_{filar}} \right. \\ &\quad \left. + \frac{\left(F \frac{D_{mean}}{2} \sin \gamma \right)^2 L_{filar}}{E_{filar}I_{filar}} \right] \\ &= \frac{F^2 D_{mean}^2 L_{filar}}{8} \left[\frac{\cos^2 \gamma}{G_{filar}J_{filar}} + \frac{\sin^2 \gamma}{E_{filar}I_{filar}} \right] \end{aligned} \quad (2-25)$$

The applied force F causes the coil to deflect δ along its axis. This external work can be determined by Eq. (2-26).

$$\text{Work } W = \frac{1}{2} F \delta \quad (2-26)$$

Hearn shows that the strain energy is equal to the work W done by the force F on the coil [38].

Setting Eq. (2-25) equal to Eq. (2-26), the deflection δ along the coil axis is determined.

$$\begin{aligned} \frac{1}{2} F \delta &= \frac{F^2 D_{mean}^2 L_{filar}}{8} \left[\frac{\cos^2 \gamma}{G_{filar} J_{filar}} + \frac{\sin^2 \gamma}{E_{filar} I_{filar}} \right] \\ \delta &= \frac{F D_{mean}^2 L_{filar}}{4} \left[\frac{\cos^2 \gamma}{G_{filar} J_{filar}} + \frac{\sin^2 \gamma}{E_{filar} I_{filar}} \right] \end{aligned} \quad (2-27)$$

The length of the filar L_{filar} can be related to the coil pitch P , coil mean diameter D_{mean} , and the overall coil length L_{coil} .

$$L_{filar} = n D_{mean} \pi \sec \gamma = \frac{L_{coil}}{P} D_{mean} \pi \sec \gamma \quad (2-28)$$

Substituting Eq. (2-28) into Eq. (2-29) results in the deflection δ along the coil axis.

$$\delta = F \frac{L_{coil}}{4P} D_{mean}^3 \pi \sec \gamma \left[\frac{\cos^2 \gamma}{G_{filar} J_{filar}} + \frac{\sin^2 \gamma}{E_{filar} I_{filar}} \right] \quad (2-29)$$

For an equivalent beam under an axial load, the deflection δ along the axis of the beam can be determined by Eq. (2-30) with the applied axial load F , material E_{beam} , beam length L_{beam} , and beam cross sectional area A_{beam} .

$$\epsilon = \frac{\delta}{L_{beam}} = \frac{\delta}{L_{coil}} \quad \sigma = E\epsilon = \frac{F}{A} \quad \delta = \frac{F L_{beam}}{E_{beam} A_{beam}} \quad (2-30)$$

Setting the deflection δ equal to each other for Eq. (2-29) and Eq. (2-30), the axial stiffness for an equivalent beam can be determined that will match the coil's axial stiffness.

$$\frac{F L_{beam}}{E_{beam} A_{beam}} = F \frac{L_{coil}}{4P} D_{mean}^3 \pi \sec \gamma \left[\frac{\cos^2 \gamma}{G_{filar} J_{filar}} + \frac{\sin^2 \gamma}{E_{filar} I_{filar}} \right] \quad (2-31)$$

After rearranging, the elastic axial stiffness for a coil κ undergoing an axial force is determined. This expression assumes the coil only has a single filar ($N=1$) or wire.

$$\kappa = \frac{E_{beam} A_{beam}}{L_{beam}} = \frac{4P \cos \gamma}{L_{coil} D_{mean}^3 \pi \left[\frac{\cos^2 \gamma}{G_{filar} J_{filar}} + \frac{\sin^2 \gamma}{E_{filar} I_{filar}} \right]} \quad (2-32)$$

If the coil consists of more than one filar ($N>1$), the elastic axial stiffness is multiplied by the number of filars N .

$$\kappa = \frac{E_{beam} A_{beam}}{L_{beam}} = N * \frac{4P \cos \gamma}{L_{coil} D_{mean}^3 \pi \left[\frac{\cos^2 \gamma}{G_{filar} J_{filar}} + \frac{\sin^2 \gamma}{E_{filar} I_{filar}} \right]} \quad (2-33)$$

After rearranging and using Eq. (2-1) for the coil pitch angle γ , the elastic axial stiffness for a coil undergoing a axial force is determined as

$$\kappa = \frac{E_{beam} A_{beam}}{L_{beam}} = N * \frac{4 \tan \gamma \cos \gamma}{L_{coil} D_{mean}^2 \left[\frac{\cos^2 \gamma}{G_{filar} J_{filar}} + \frac{\sin^2 \gamma}{E_{filar} I_{filar}} \right]} \quad (2-34)$$

2.5 ELASTIC STIFFNESS SUMMARY AND COMPARISON

The elastic stiffnesses have been determined and are summarized in Table 2-1. They are functions of the pitch angle γ , the number of filars in the coil N , filar modulus of elasticity E_{filar} , filar shear modulus G_{filar} , filar moment of inertia I_{filar} , and filar polar moment of inertia J_{filar} .

Table 2-1 Analytically Derived Equivalent Stiffnesses for a Coil

Bending	$\beta = E_{beam} I_{beam} = N * \frac{2 \tan \gamma \cos \gamma}{\left[\frac{1}{E_{filar} I_{filar}} + \frac{\sin^2 \gamma}{E_{filar} I_{filar}} + \frac{\cos^2 \gamma}{G_{filar} J_{filar}} \right]} \quad (2-14)$
Torsional	$\alpha = G_{beam} J_{beam} = N * \frac{\tan \gamma \cos \gamma}{\left[\frac{\sin^2 \gamma}{G_{filar} J_{filar}} + \frac{\cos^2 \gamma}{E_{filar} I_{filar}} \right]} \quad (2-24)$
Axial	$\kappa = \frac{E_{beam} A_{beam}}{L_{beam}} = N * \frac{4 \tan \gamma \cos \gamma}{L_{coil} D_{mean}^2 \left[\frac{\cos^2 \gamma}{G_{filar} J_{filar}} + \frac{\sin^2 \gamma}{E_{filar} I_{filar}} \right]} \quad (2-34)$

The stiffnesses can be rearranged and the elastic properties can be determined (Table 2-2).

Table 2-2 Equivalent Elastic Beam Properties

Elastic Modulus	$E_{beam} = \frac{N}{I_{beam}} * \frac{2 \tan \gamma \cos \gamma}{\left[\frac{1}{E_{filar} I_{filar}} + \frac{\sin^2 \gamma}{E_{filar} I_{filar}} + \frac{\cos^2 \gamma}{G_{filar} J_{filar}} \right]} \quad (2-35)$
Shear Modulus	$G_{beam} = \frac{N}{J_{beam}} * \frac{\tan \gamma \cos \gamma}{\left[\frac{\sin^2 \gamma}{G_{filar} J_{filar}} + \frac{\cos^2 \gamma}{E_{filar} I_{filar}} \right]} \quad (2-36)$

The coil mean diameter D_{mean} , is assumed for the beam element diameter D_{beam} , and the area and polar area moment of inertias (I_{beam} and J_{beam}) can be calculated. Then, the elastic

modulus E_{beam} , and shear modulus G_{beam} , can be determined from Eq. (2-35) and (2-36).

Table 2-3 lists the material properties that will be used in the numerical simulation. The

Appendix has a sample analytical beam approximation calculation.

Table 2-3 Material Properties for Simulation Models

	Number of Filars in Coil	Wire Diameter	Mean Diameter	Coil Pitch per filar	Calculated Elastic Modulus	Calculated Elastic Shear Modulus
	N	d_{filar} (mm)	D_{mean} (mm)	P (mm)	E_{beam} (MPa)	G_{beam} (MPa)
Coil A	4	0.127	0.635	0.610	363	211
Coil B	6	0.102	0.610	0.635	283	163
Coil C	5	0.102	0.610	0.635	236	137

CHAPTER 3

RADIAL FORCE EXPERIMENTATION IMPLEMENTATION AND RESULTS

3.1 INTRODUCTION

Experimentation is needed to measure the force between the lead and the cardiac vein wall. This force is caused by the vein wall preventing the distal tip from returning to its two- or three-dimensional shape after insertion. This experimentation provided validation for the numerical simulation used later in the thesis. Two approaches are *in-vivo* animal model experimentation with living hearts, or *in-vitro* bench experimentation simulating the heart anatomy.

For the *in-vivo* experiments the lead would be positioned in a vein outside the left ventricle with a force gage connected to the terminal or proximal end of the lead. The lead could then be extracted at a certain rate and direction with the force measured versus time or displacement. This approach has the advantage of providing a realistic force measurement for lead dislodgment. Disadvantages of this approach for *in-vivo* experimentation are the high cost of animal studies with multiple studies needed for each distal end design. Also, the variation in the cardiac and circulatory system for each animal introduces variability by changing the size and torturous path in which the lead is placed in for each experiment.

In-vitro experimentation can be performed in several different ways. The distal end of the lead could be inserted into glass tubes with varying diameters to visualize the appearance of the lead as it is prevented from returning to its pre-formed shape. The glass tubes would only provide qualitative data of how the lead looks. Disadvantages would be the lack of quantitative force data from this approach.

Another *in-vitro* experiment could be to insert the leads into tubes and attach a force gage to the proximal end to extract the lead from the tubes. This would provide an extraction force for the leads and an indirect measurement of the fixation force in the tube since friction would need to be accounted for. The disadvantage of this approach is that the fixation force of the lead is not measured directly and friction would have a strong influence on the results. Friction between the distal lead tip, which is typically silicone rubber, and the tubing wall could be influenced by external factors such as temperature and humidity which could be difficult to control.

The *in-vitro* experiment adopted in this thesis is a radial force tester to quantify the fixation forces exerted by a left-ventricle lead when a wall prevents it from returning to its original shape. This instrumentation simulates a rigid tube and measures the overall radial force exerted on the tube for a given diameter. Radial force testers are used to measure and record radial force during expansion and compression of interventional devices such as expandable stents and other radial expanding devices [39].

A radial force tester from Machine Solutions Inc., Flagstaff, AZ was used for the experiment.

A radial force tester has a movable mechanical iris that contracts and expands to different

diameters as it measures the overall radial force that an object exerts on the iris. Typically radial force testers record radial force measurements as they contract and expand at certain rate. Rate can be varied to determine if this affects the measurement.

In this thesis, *in-vitro* experimentation with a radial force tester was used. Samples with a two- or three- dimensional distal shape were completely straightened with a guidewire and inserted into a radial force tester. The guidewire was then removed allowing the sample to return to its pre-formed shape but the walls of the tester prevented this. The tester then measured the radial force that the sample exerted on the walls.

3.2 DISTAL LEAD SAMPLES

Simplified experimental samples were fabricated (Figure 3-1). These samples consisted of a coil inside silicone tubing as described below.

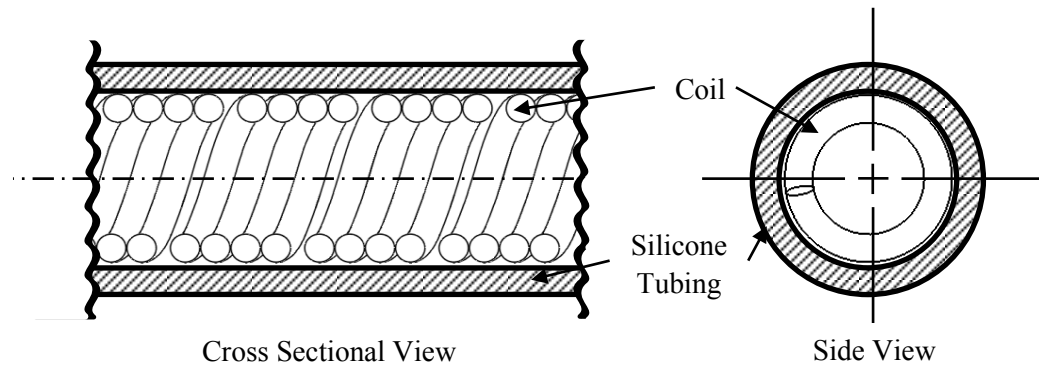


Figure 3-1 Simplified Experimental Samples

The use of a coil reduced the cost of experimenting with actual leads. The other benefit is that

samples can be created with various coil stiffnesses. The stiffness of the coils can be varied by changing their geometry. The stiffness is affected by the number of wire filars used to make the coil, filar diameter, filar pitch, and coil diameter. The MP35N material for the wire was used for all samples (Table 3-1). The silicone tubing will have an inner diameter of 1.118-mm with a wall thickness of 0.254-mm.

Table 3-1 MP35N Material Properties

Material	Young's Modulus (GPa)	Shear Modulus (GPa)
MP35N	234	81

3.2.1 ELASTIC COIL STIFFNESS

To determine whether elastic coil stiffness affects the radial force for the same two-dimensional distal shape, three different coil designs were evaluated (Table 3-2). The designs varied in stiffness by having different wire diameter, number of filars, and coil pitch. Coils can be wound with a single filar (wire) or multiple filars. Coil pitch is defined as the axial distance along the centerline for one filar to wrap 360 degrees. These coil designs (Figure 3-2) were slight variations on coils used in actual leads [6]. The inside coil diameter is dictated by guidewire diameters that are inserted into the leads.

Table 3-2 Coil Design Parameters

	Material	Wire Diameter d_{filar} (mm)	Number of Filars N	Coil Inner Diameter D_{inner} (mm)	Coil Pitch per Filar P (mm)
Coil A	MP35N	0.127	4	0.508	0.610
Coil B	MP35N	0.102	6	0.508	0.635
Coil C	MP35N	0.102	5	0.508	0.635

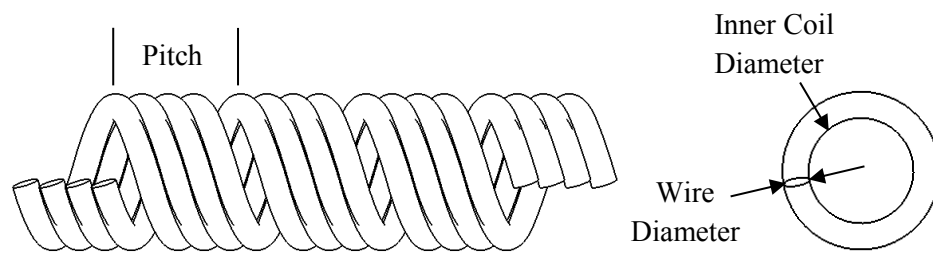


Figure 3-2 Coil Design Parameters (4 Filar Shown)

The coil design was varied (Table 3-2) to change the elastic stiffness of the coil. Chapter 2 showed the derivation of how the elastic stiffness of a coil is determined and the results are shown in Table 3-3. The elastic bending stiffness is calculated by multiplying the modulus of elasticity E of the material by its moment of inertia I about the bending axis. An assumption is that the radial force is related to the coil stiffness and so Table 3-3 compares the stiffness of Coil B and Coil C with Coil A.

Table 3-3 Bending Stiffness of Coil Designs

	Wire Diameter	Number of Filars in Coil	Coil Pitch per filar	Elastic Bending Stiffness	Analytically Derived Bending Stiffness Change Relative to Coil A %
	d_{filar} (mm)	N	P (mm)	E_{beam} (MPa x mm ⁴)	%
Coil A	0.127	4	0.610	2.90	NA
Coil B	0.102	6	0.635	1.92	- 34
Coil C	0.102	5	0.635	1.60	- 45

3.2.2 DISTAL TWO-DIMENSIONAL PRE-FORMED SHAPE

The samples had a pre-formed shape at the distal tip of the coil that was a flat two-dimensional circular loop as illustrated in Figure 3-3. This loop was created by tightly winding the coil around a mandrel. This distal end loop had an inner diameter of 13-mm and a 360 degree wrap angle. The tip of the sample had a straight length of 1-mm which is used to minimize the contact force at the tip of the lead to reduce potential damage to the heart wall or vein.

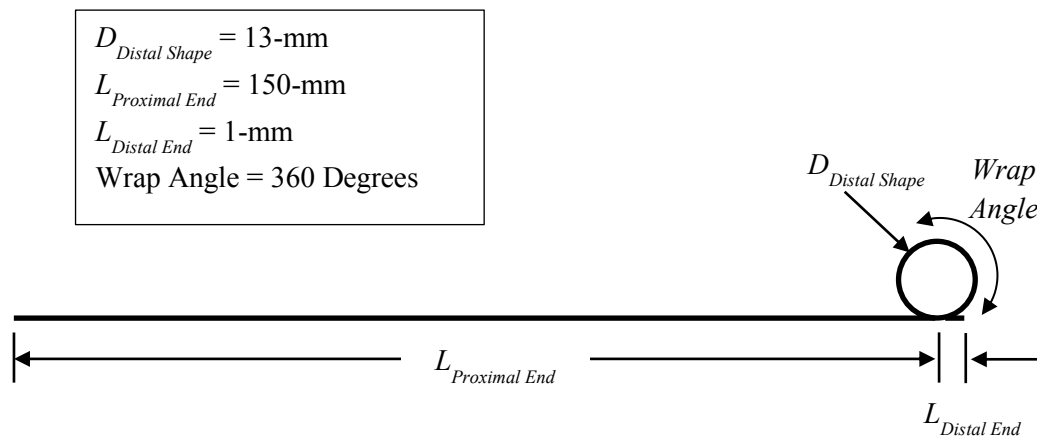


Figure 3-3 Coil Sample with Distal Shape for Radial Force Tester

3.3 EXPERIMENTATION PROCEDURE

3.3.1 TARE (EMPTY) FORCE MEASUREMENT BEFORE AND AFTER

EXPERIMENTATION

The frictional forces or tare of forces must be measured before and after the experiment while the instrumentation is empty. This tare force can then be subtracted from the forces measured with the sample to give the actual forces. This was done before and after the experiment to see if the radial force tester varied with time and to check that the equipment did not experience any anomalous behavior.

3.3.2 SAMPLE SETUP

Proper sample placement in the radial tester reduces variability during testing. For experimentation a guidewire is inserted into the sample, and then the distal end of the straightened sample is placed into the iris of the tester along the axial center line (Figure 3-4). During loading, the radial force tester has the mechanical iris set to the largest diameter used for testing. A raised platform outside the tester serves to align the sample with the centerline of the iris. A one kilogram weight is placed on the proximal end of the sample to prevent axial movement of that end during experimentation. To reduce slack in the sample, the platform with the weight is placed as close as possible to the radial force tester. After the straightened sample has been positioned, the guidewire is removed to allow the lead to return to its pre-formed shape but since the mechanical iris prevents this a force against the tester walls is created.

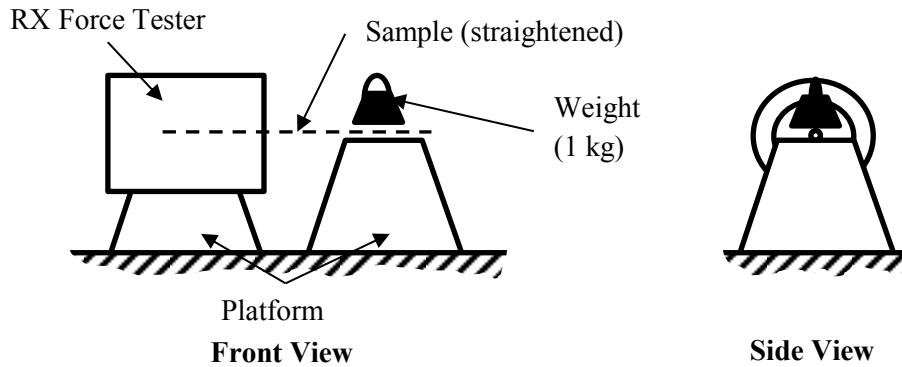


Figure 3-4 Radial Force Tester Setup

3.3.3 EXPERIMENTAL PROCEDURE

The radial force tester dynamically contracts and expands the mechanical iris between two diameters and then dwells or idles for a certain length of time at these diameters as it transitions and changes direction (Figure 3-5). The appropriate diameter range and rate of contraction and expansion with dwell time were determined.

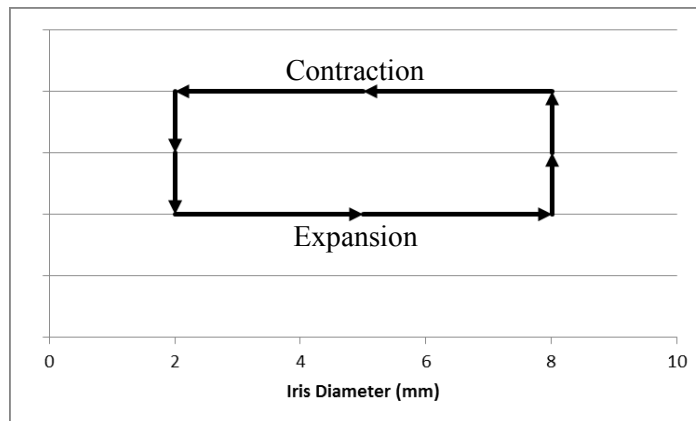


Figure 3-5 Contraction and Expansion of a Single Cycle

The diameter range to evaluate lead fixation forces should be typical of the blood vessels the

leads will be placed into outside the left ventricle. Literature searches have found that the diameter of the coronary sinus and other veins outside the left ventricle can range from 2- to 8-mm in diameter [40, 41].

The rate of contraction and expansion of the radial force tester can range from 0.01 to 5.0 mm/sec. The rate was varied in this range and force measurements were found not to vary significantly with rate. A rate of 1 mm/sec was chosen for the speed that the iris contracts and expands around the samples. Force measurements were taken every 240 milliseconds.

As the iris contracts and expands it dwells or stops for a certain duration at the maximum and minimum iris diameter. This dwell time allows the iris to change direction between contraction and expansion. At these transition times the forces driving the iris change magnitude and direction. After a second of dwell time the forces stabilize around a steady value. A dwell time of three seconds was chosen.

The radial force tester uses a mechanical iris which is composed of multiple wedges that slide against each other as it contracts and expands. These wedges are subject to frictional forces that act on each other even when the tester is empty and can produce noise in the measurements.

To reduce noise in the data, a simple moving average Eq. (3-1) was used on the force measurements. A simple moving average is the mean taken from an equal number of data points on either side of the central value. A moving average of 1-mm before and after the central value was used. For example, at 4-mm the forces will be averaged from 3- to 5-mm.

F_{4mm} Moving Average

$$= \frac{F_{3mm} + F_{3.25mm} + F_{3.5mm} + F_{3.75mm} + F_{4mm} + F_{4.25mm} + F_{4.5mm} + F_{4.75mm} + F_{5mm}}{n} \quad (3-1)$$

For data collection, three samples were used for each coil design and each sample was cycled multiple times. For each sample, the iris diameter contracted to 2-mm and expanded to 8-mm for four cycles at a rate of 1-mm per second (Figure 3-5). Radial forces were measured every 240 milliseconds or about 4 times per second (Figure 3-6). The moving average calculation at the contraction and expansion transition (2- and 8-mm) was modified to average the all forces at the transition diameter, 2- or 8-mm, together. The first cycle at startup was not used since frictional forces are higher at startup with the iris not moving. The experiment was performed at room temperature and humidity was not controlled.

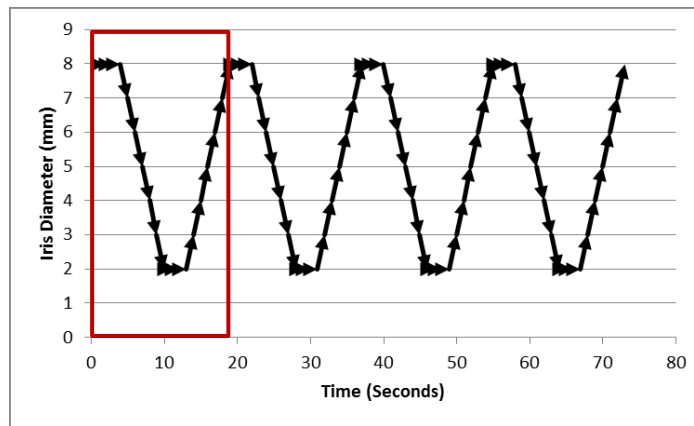


Figure 3-6 Radial Force Test Cycle vs. Time – Startup Cycle Highlighted

3.4 RESULTS

3.4.1 TARE OR EMPTY RADIAL TESTER FORCES

The first force measurements were performed with the radial force tester empty. This baseline force with the tester empty (i.e., tare force) is needed so it can be subtracted from actual sample measurements. Two baselines with the tester empty were measured, once at the beginning prior to the samples being measured and then again at the end after all sample measurements had been completed.

Experimental data for the tare force is displayed in Figure 3-7. The first column shows the force measurement before the samples were tested. The second column shows the force measurement after the samples were tested. Before and after tare measurements were performed to check for anomalous behavior during the experiment that could affect the force measurements.

Radial force measurements versus iris diameter are shown in the sub-figures that comprise Figure 3-7. The plots show a loop as the force was measured during iris contraction and expansion for three cycles. Arrows on the plot show the counterclockwise direction of the iris contraction and expansion.

For each column in Figure 3-7 three plots are shown. The top plot shows the raw force data which has scatter, variation, or noise. To reduce these intrusive features a simple moving average was performed on the data with the outcome shown in the middle plots. A moving average with a 1-mm interval before and after was used Eq. (3-1). The bottom plots show the

force measurement after all three cycles were averaged together. The plots show that the force measurement before and after the experiment were not significantly different and that the equipment did not experience any anomalous behavior.

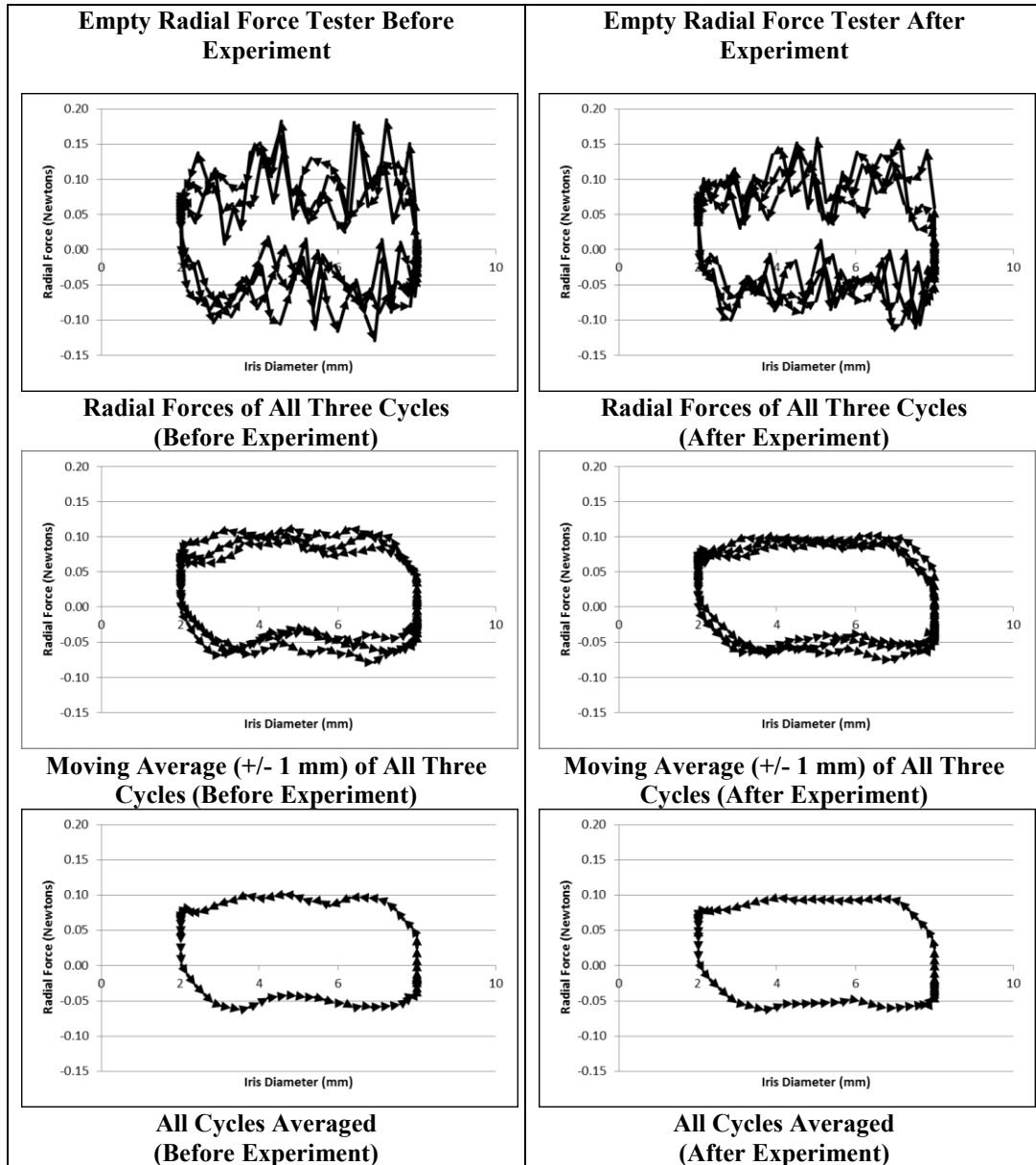


Figure 3-7 Average Radial Forces (Before and After) in Empty Tester

The tare (or empty) force measurements were needed so that they could be subtracted from the forces measured from the samples. Figure 3-8 shows the average tare force combined from before and after the experiment.

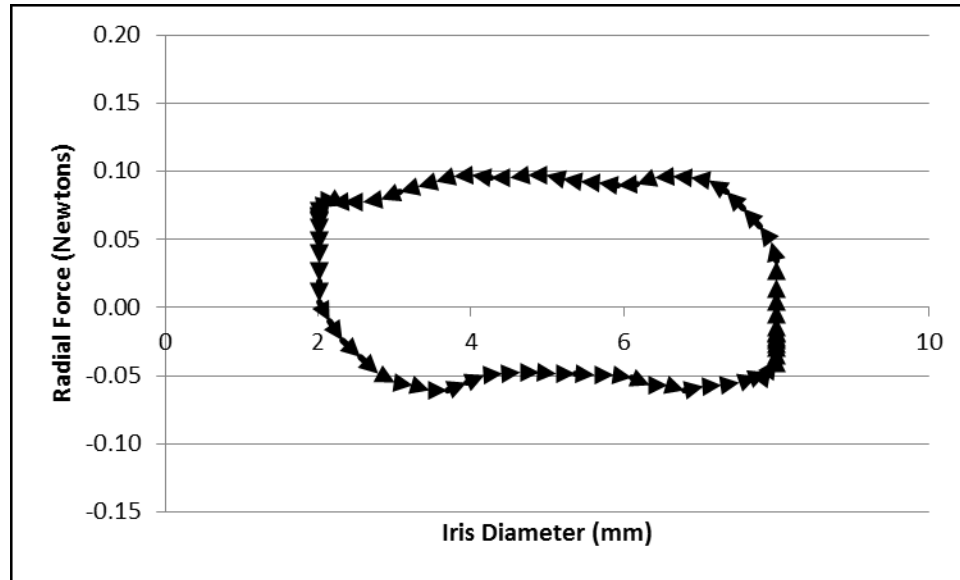


Figure 3-8 Tare (or Empty) Force Measurement (Before and After)

Figure 3-9 pictorially shows the tare force being subtracted from the sample measurement resulting in the corrected sample measurement shown in the rightmost plot.

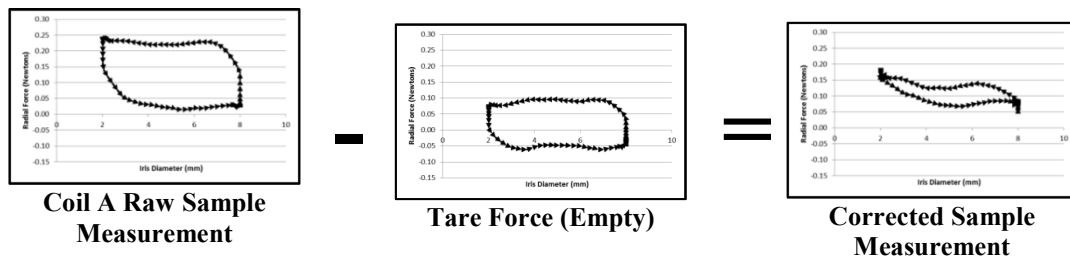


Figure 3-9 Sample Measurement Corrected by Subtracting the Tare Force

3.4.2 SAMPLE DATA

The force measurements taken for all three coil designs A, B, and C are conveyed in Figure 3-10 through Figure 3-18. Each coil design was represented by three samples, and each sample was cycled four times, however only the last three cycles are presented.

For the graphs, each column corresponds to a single sample and shows the three measured cycles. The top graph shows the raw force data which has variation or noise. Noise/variation reduction was achieved by use of a moving average, with the outcome shown in the middle tier. The bottom tier of plots shows the force measurements after all three cycles were averaged together for each sample. Finally all three samples are averaged together in the lower left graph and then the tare (empty) forces are subtracted.

Chapter 3

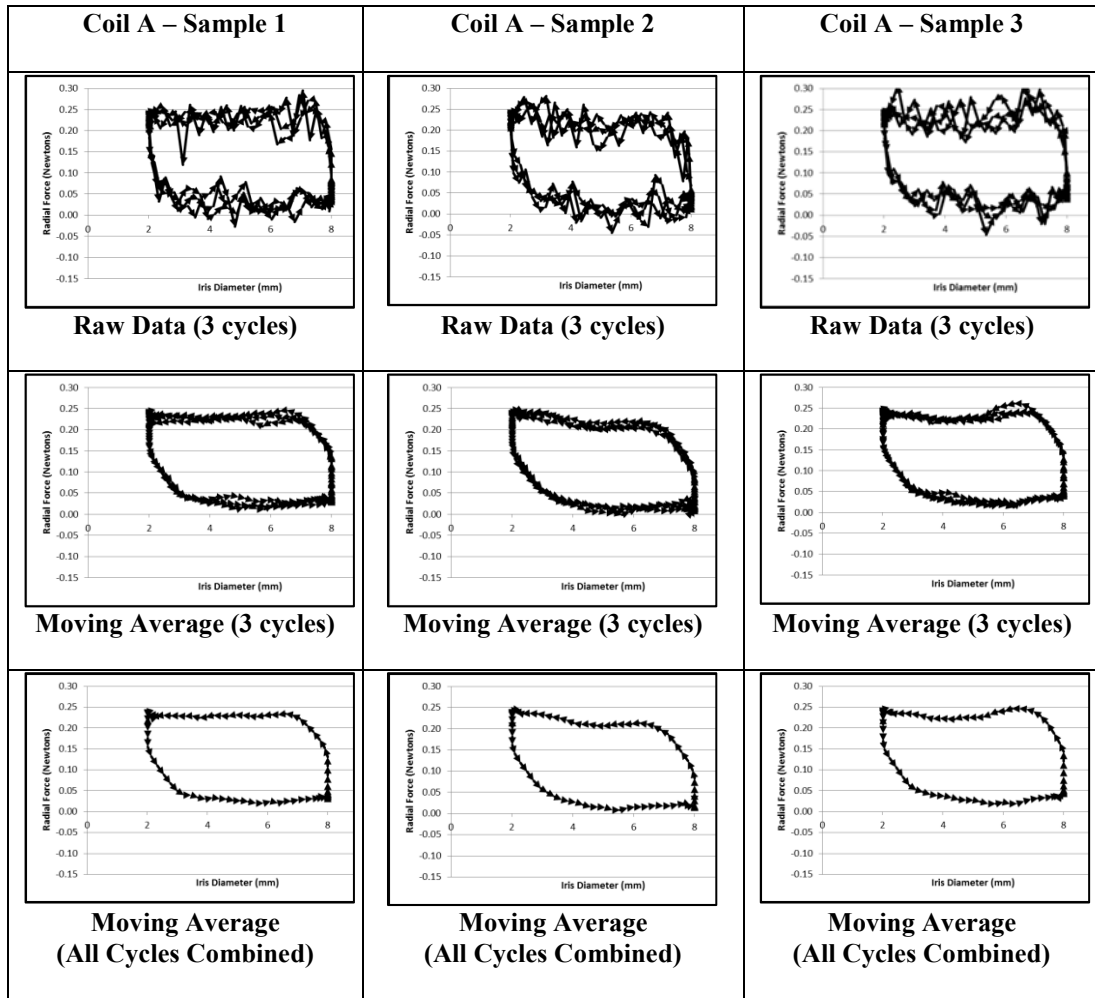


Figure 3-10 Coil A Force Measurements

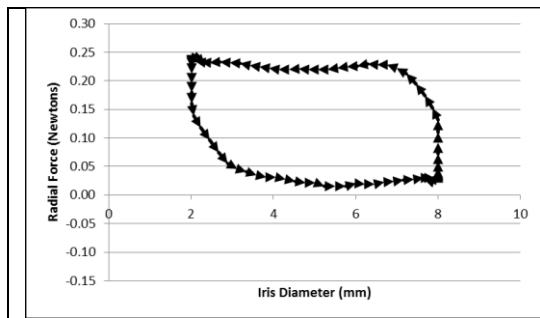


Figure 3-11 All Three Samples Averaged
(Moving Average with All Cycles Combined)

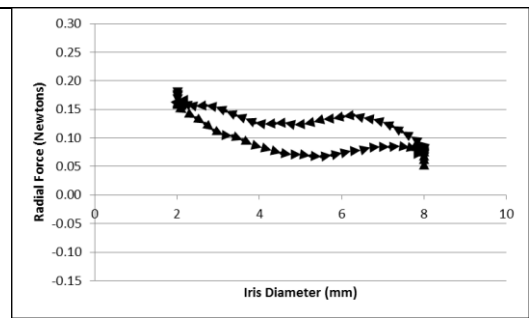


Figure 3-12 All Three Samples Averaged
with Tare (Empty) Forces Subtracted

Chapter 3

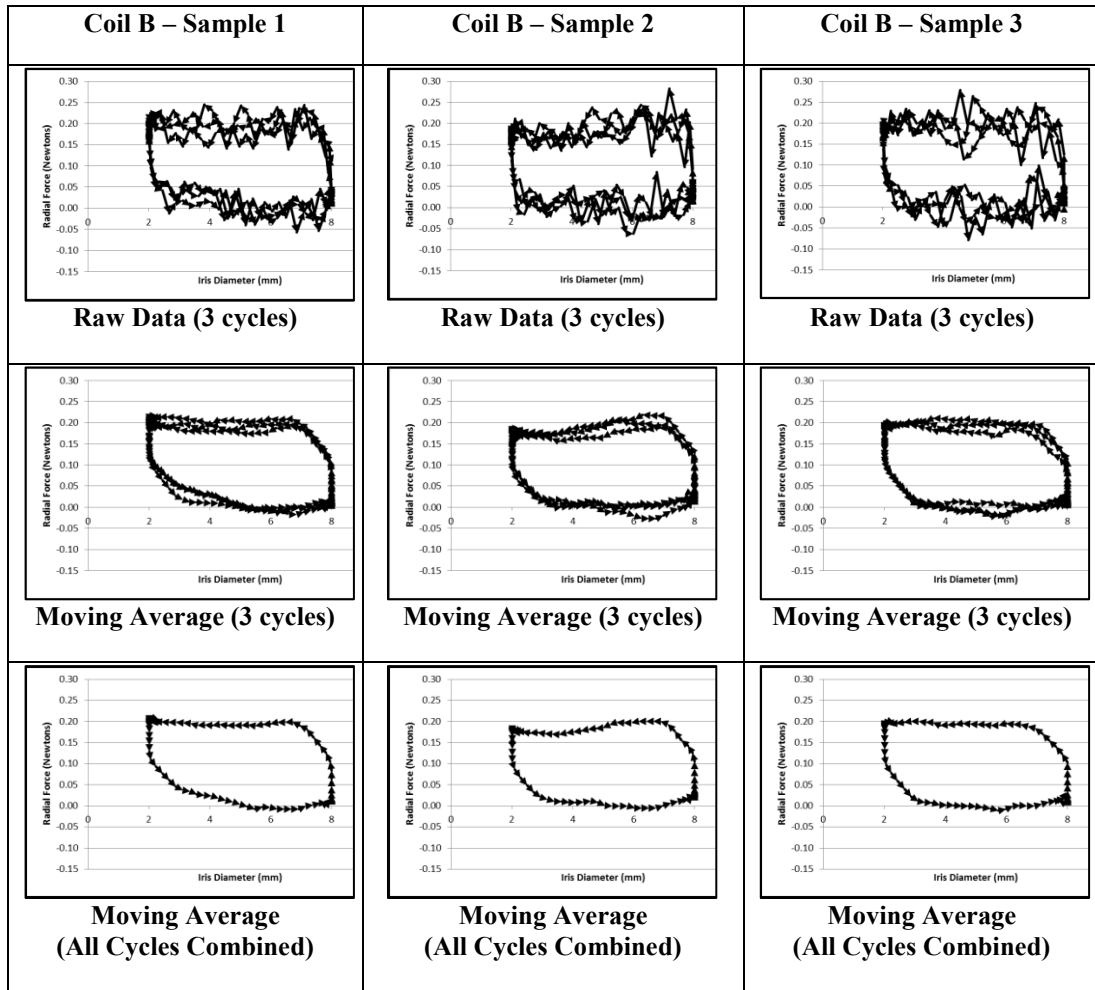


Figure 3-13 Coil B Force Measurements

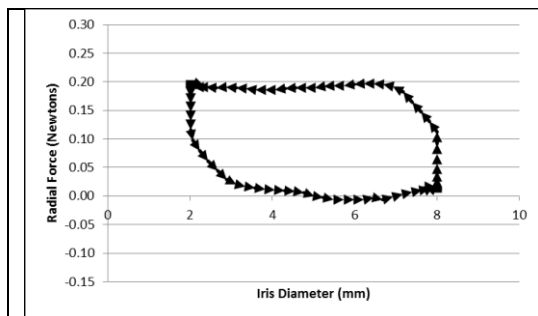


Figure 3-14 All Three Samples Averaged
(Moving Average with All Cycles Combined)

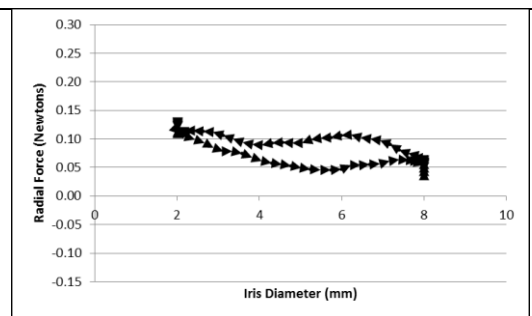


Figure 3-15 All Three Samples Averaged
with Tare (Empty) Forces Subtracted

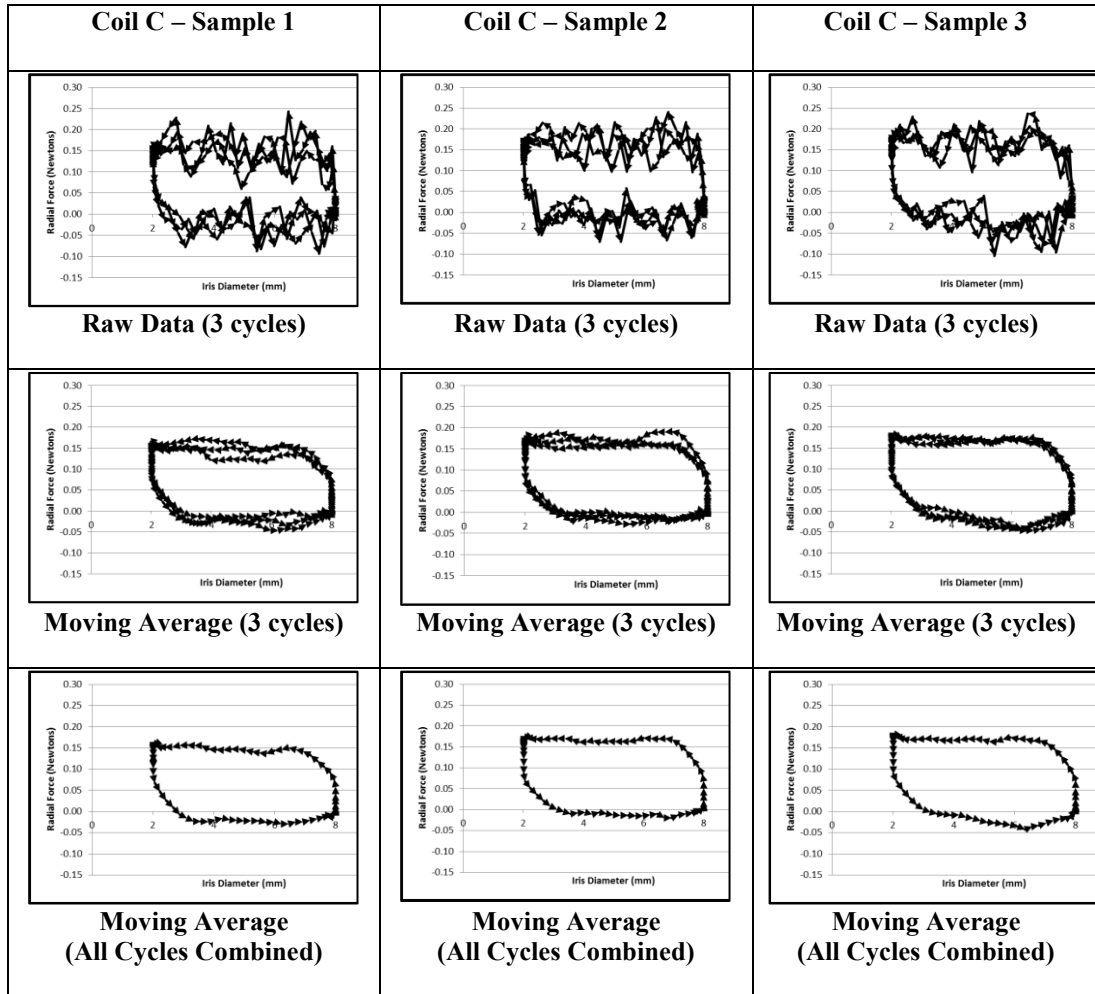


Figure 3-16 Coil C Force Measurements

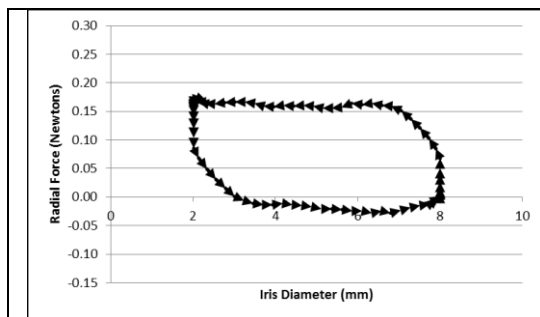


Figure 3-17 All Three Samples Averaged
(Moving Average with All Cycles Combined)

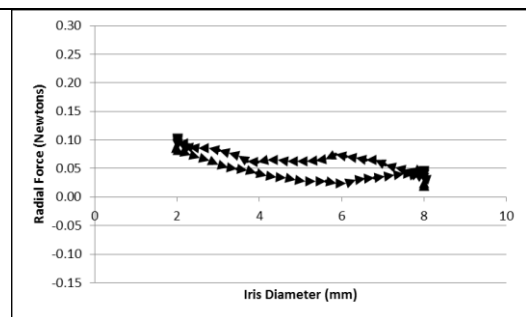


Figure 3-18 All Three Samples Averaged
with Tare (Empty) Forces Subtracted

3.4.3 DATA ANALYSIS

When the radial force results for all three coil designs are compared to each other it is apparent that the respective radial force measurements are different (Figure 3-19). Coil A has the highest radial force followed by Coil B and then Coil C.

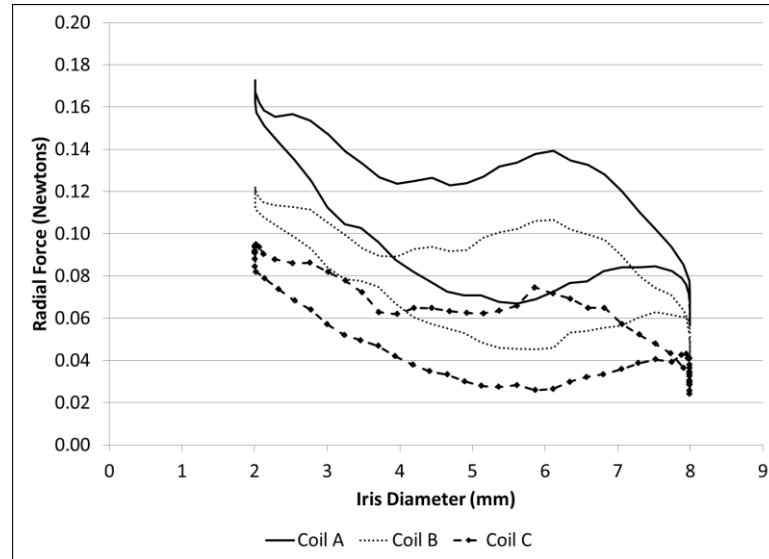


Figure 3-19 Coil Designs (Contraction and Expansion)

To allow a quantitative comparison between the coil designs, each coil had its contraction and expansion values averaged together at a given iris diameter of 2-, 4-, 6- and 8-mm (Figure 3-20 through Figure 3-22)

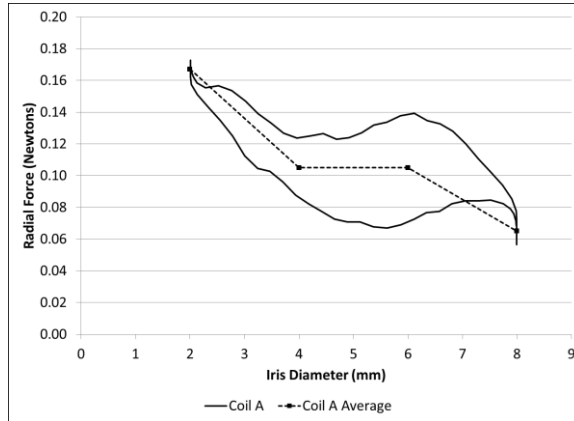


Figure 3-20 Coil A Radial Force and Average

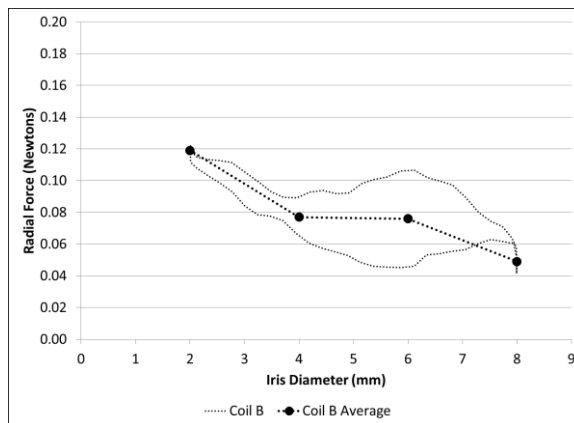


Figure 3-21 Coil B Radial Force and Average

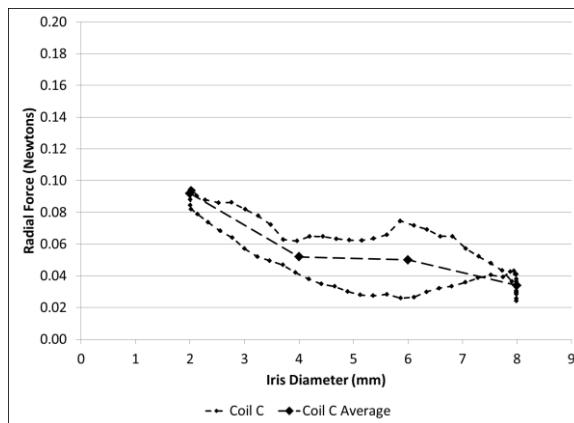


Figure 3-22 Coil C Radial Force and Average

Table 3-4 lists the average radial force for each coil at a given tube diameter and then compares the radial force of Coil B and C with Coil A.

Table 3-4 Radial Force Average Comparison at Given Tube Diameter (Experiment)

Tube Diameter (mm)	Coil A Average (N)	Coil B Average (N)	Radial Force Change Between Coil B and Coil A (%)	Coil C Average (N)	Radial Force Change Between Coil C and Coil A (%)
2	0.167	0.119	-29	0.092	-45
4	0.105	0.077	-27	0.052	-50
6	0.105	0.076	-28	0.050	-52
8	0.065	0.049	-25	0.034	-48

Coil A generates the highest radial force over the range of tube diameters. Coil B has a 25 % to 29 % lower radial force compared to Coil A, and Coil C has a 45 % to 52 % lower radial force compared to Coil A (Table 3-4). Table 3-5 compares the coil stiffness (Table 3-3) with the radial forces and shows coil stiffness has a direct influence on radial force.

Table 3-5 Coil Design Comparison with Coil Stiffness and Radial Force

	Elastic Bending Stiffness (MPa x mm⁴)	Analytically Derived Stiffness Change Relative to Coil A (%)	Radial Force Change Relative to Coil A (%)
Coil A	2.90	NA	NA
Coil B	1.92	- 34	- 25 to - 29
Coil C	1.60	- 45	- 45 to - 52

CHAPTER 4

USE OF EXPERIMENTAL RESULTS FOR NUMERICAL MODEL VALIDATION

4.1 INTRODUCTION

Numerical simulation will be used to determine the force between the distal shape of the lead and the wall of the cardiac vein. For the simulations, a simplified representation of the lead distal shape will be used. To simulate the wall of the cardiac vein, a simplification will be to use a straight rigid cylindrical tube in the model. This simplification allows the interaction force between the lead distal shape and vein to be determined. This simplification is also similar to the experimentation completed in Chapter 3.

The stresses within the lead itself are out of the present scope, although they can be calculated as part of the analytical elastic stiffness derivation [5]. A more thorough evaluation of the coil stresses would need to include fatigue, corrosion, and other design conditions which could be evaluated later. The coil designs evaluated here are similar to coils that have been used and implanted for ten to twenty years [6].

This simulation model provides forces that the lead distal shape exerts against a straight tube. The overall radial force can be compared to that of experiment to provide validation of the numerical simulation based on simplifications and assumptions. The experiment in Chapter 3

used a radial force tester that was a straight rigid tube and the experimental samples were similar to the simulation model. The simulation will also provide the distribution of the radial force along the axis of the lead, including the tip force. In addition, the relationship between radial forces and lead stiffness will be examined, as well as the effect of friction on radial force between the lead and the tube wall. ABAQUS, a commercial finite element analysis code, will be used for the numerical simulation. A flow chart of the numerical simulation setup is shown in Figure 4-1 with a detailed description in the Appendix.

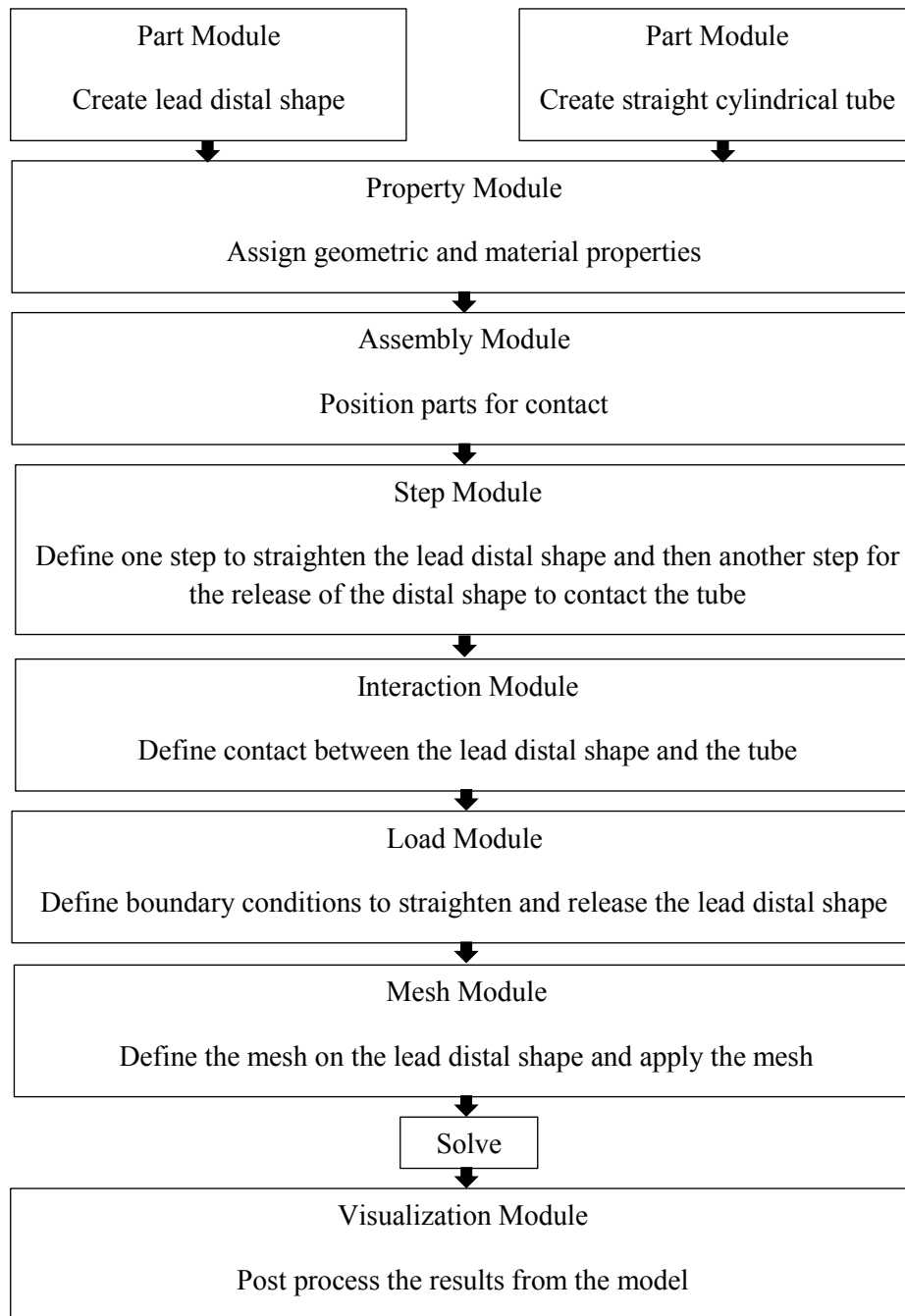


Figure 4-1 Flowchart of Numerical Simulation

4.2 DISTAL LEAD SHAPE MODEL

The simulation model of the lead will use the finite element method to discretize the geometry into elements. Three-dimensional beam elements will be used to simulate the lead distal shape. The radial force that the lead distal shape exerts on a straight tube with various diameters ranging from 2- to 8-mm will be determined to compare with the experimental results.

For the experiment, a radial force tester took continuous measurements as the mechanical iris or tube surrounding the lead distal shape was contracted and expanded between 2- and 8-mm. For the simulation model, continuous measurement with the tube expanding and contracting would be time consuming and difficult, so radial force measurements will be extracted at discrete tube diameters of 2-, 4-, 6-, and 8-mm and compared to the experimental results.

A simplified model of the lead was used. As noted previously, the lead is constructed of various coils, plastic tubing, cables, and electrodes. For experimentation, samples consisted of a coil inside silicone tubing as described previously (Section 3.2). For the simulation model, simple three-dimensional beam elements were used. Beam elements are line elements used to create a one-dimensional idealization of a three-dimensional structure. For convenience, the adopted beam elements had a circular cross section with an outer diameter that matched the experimental coil mean diameter (Figure 4-2). The simulation model of the rigid tube contacting the beam elements was adjusted to account for the offset of using the coil mean diameter instead of the outer diameter of the coil.

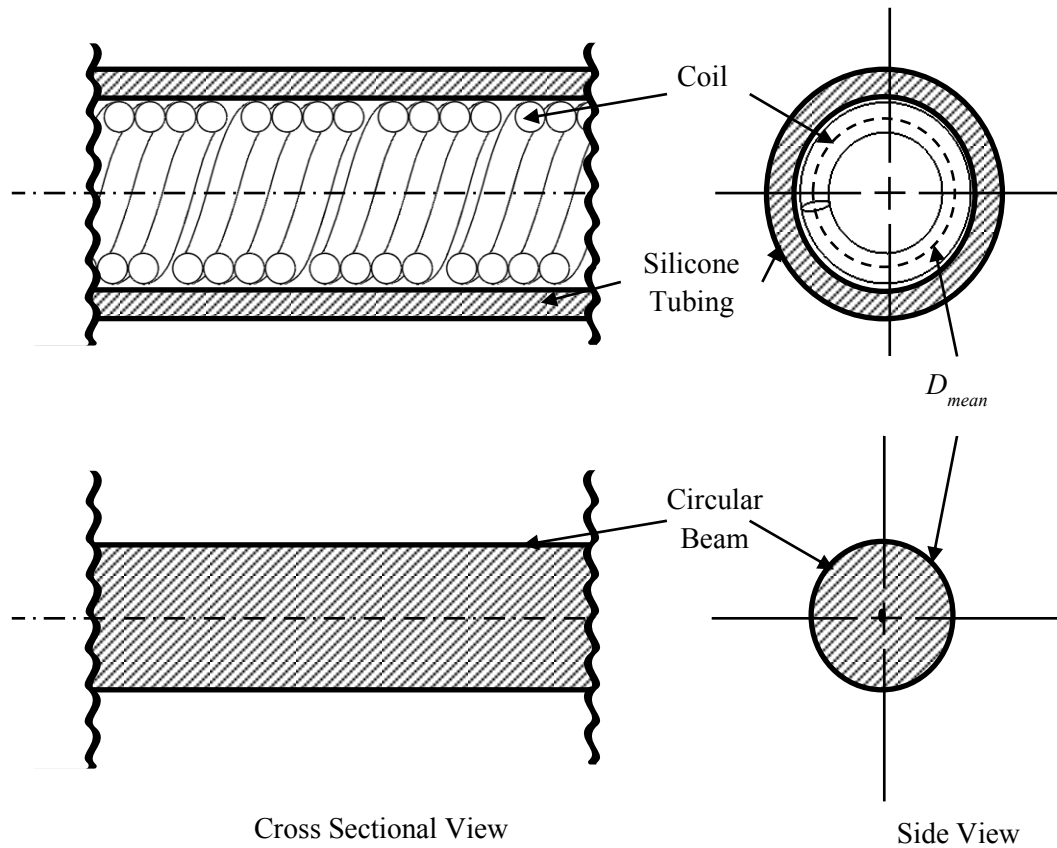


Figure 4-2 Comparison of Simplified Experimental Samples (Top) to Computer Model (Bottom)

The elastic properties of the beam were calculated based on the elastic bending stiffness, EI (Section 2.2) and elastic torsion stiffness, GJ (Section 2.3) of the coil with the assumed cross sectional diameter. Based upon the coil geometry (Table 4-1), the calculated elastic modulus E_{beam} and shear modulus G_{beam} are listed in Table 4-2. For comparison, Coil A was chosen as the baseline in Table 4-3 and lists the change in stiffness between each coil based upon their geometry of construction, when compared to Coil A.

Table 4-1 Coil Geometry

	Number of Filars in Coil	Wire Diameter	Mean Coil Diameter	Coil Pitch per filar
	N	d_{filar} (mm)	D_{mean} (mm)	P (mm)
Coil A	4	0.127	0.635	0.610
Coil B	6	0.102	0.610	0.635
Coil C	5	0.102	0.610	0.635

Table 4-2 Material Properties for Simulation Models

	Calculated Elastic Bending Stiffness $E_{\text{beam}} I$	Calculated Elastic Torsional Stiffness $G_{\text{beam}} J$	Area Moment of Inertia	Polar Area Moment of Inertia	Calculated Elastic Modulus	Calculated Elastic Shear Modulus
	β (MPa x mm ⁴)	α (MPa x mm ⁴)	I (mm ⁴)	J (mm ⁴)	E_{beam} (MPa)	G_{beam} (MPa)
Coil A	2.90	3.37	0.00798	0.0160	363	210
Coil B	1.92	2.22	0.00678	0.0136	283	163
Coil C	1.60	1.85	0.00678	0.0136	236	136

Table 4-3 Change In Elastic Modulus among Coil Designs

	Calculated Elastic Modulus	Elastic Modulus Change from Coil A	Calculated Elastic Shear Modulus	Elastic Shear Modulus Change from Coil A
	E_{beam} (MPa)	(%)	G_{beam} (MPa)	(%)
Coil A	363	NA	210	NA
Coil B	283	22	163	22
Coil C	236	35	136	35

The simulation model of the distal lead shape matches the geometry of the experimental samples (Figure 4-3). The isometric view at the upper right of Figure 4-3 shows the outline of the rigid tube overlaid on top of the distal lead shape. This tube is perfectly rigid and cannot deform in response to any force applied to it. This simple cylindrical shape is represented as

an analytical rigid surface in the software and as such does not need to be discretized and meshed.

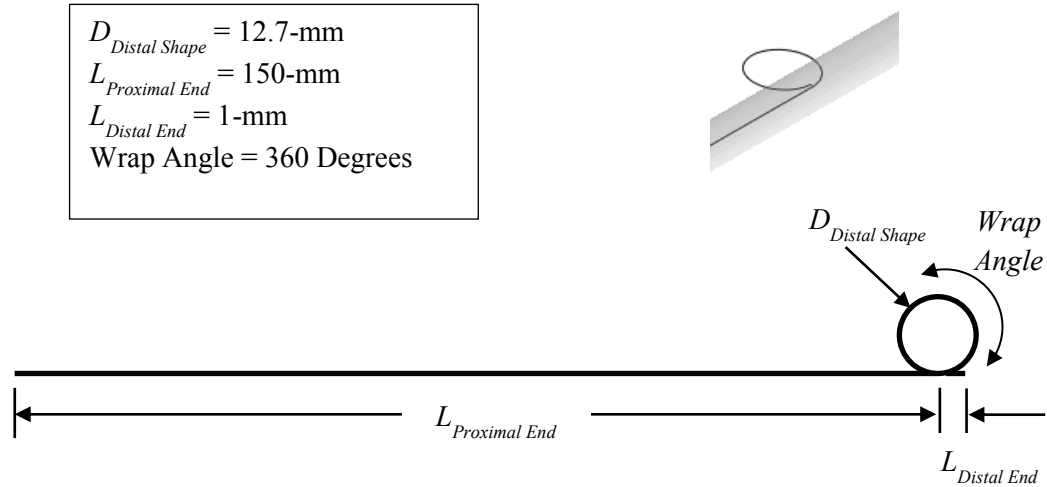


Figure 4-3 Simulation Model Geometry (Side & Isometric View)

4.3 BOUNDARY AND LOADING CONDITIONS

The proximal end will be prevented from moving by setting all degrees of freedom, DOF, to zero. This is similar to the experimental setup in Figure 3-4. The six degrees of freedom include translation in the x, y, and z directions as well as rotation about these axes. Gravity effects are neglected. Contact surfaces between the distal shape and the rigid tube were created. Contact surfaces allow the distal shape model to move freely within the tube but not penetrate or deform the rigid tube.

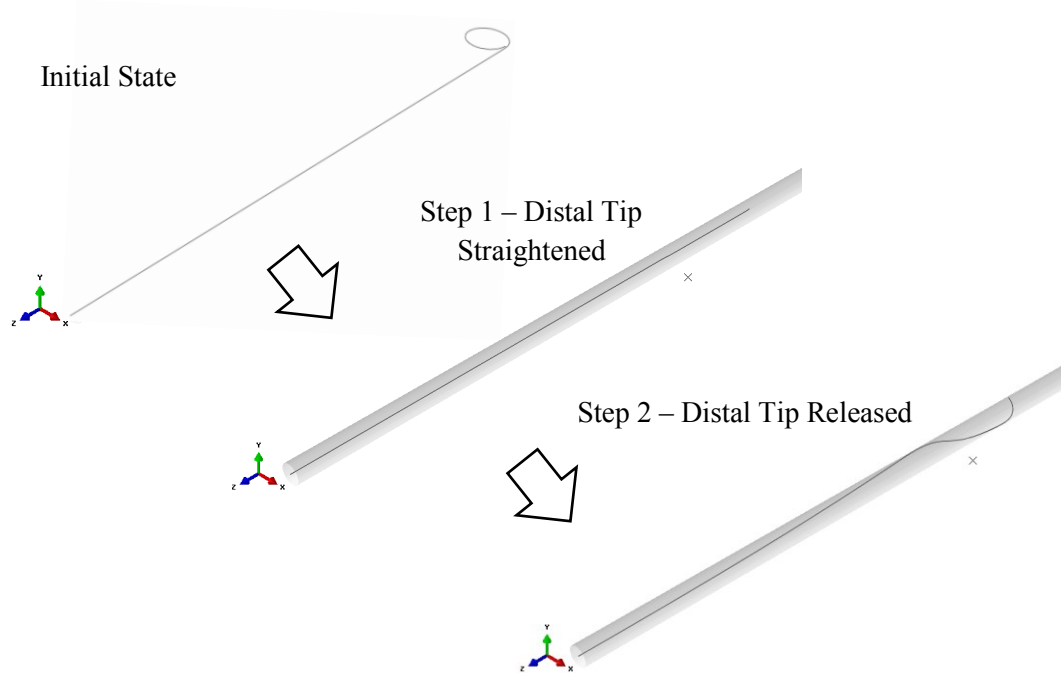


Figure 4-4 Initial State, Step 1, Step 2

Figure 4-4 illustrates the loading sequence for the model. Step 1 of the analysis is to straighten out the distal shape. This is appropriate since during the experiment this was done and this is what occurs in actual use during insertion. All contact surfaces are deactivated as the tip of the distal end is moved along the lead axis away from the proximal end.

Step 2 begins after the distal end has been straightened. The contact surfaces are activated. The distal tip is released and allowed to freely move and push against the rigid tube. The distal shape tries to return to its un-deformed shape but is prevented from doing so by the rigid tube. Once the distal shape contacts the rigid tube and reaches a final position, the displacements, and contact forces are obtained. The simulation model reports contact forces along the length of the distal shape at node locations and summing these forces results in the

total radial force. The element size used in the model was kept uniform and the same size for all the simulations. The simulation model also reports the maximum radial force.

4.4 MESH REFINEMENT EVALUATION

4.4.1 MESH BACKGROUND INFORMATION

The simulation model is discretized into elements. The size of the elements or mesh density can affect results. Accuracy of the model can usually be improved with an increase in elements or a refined mesh in the area of interest but at the expense of computer resources. The adopted model allows nonlinear geometry or large deformations, which can be computationally costly, so that a minimum number of elements is desirable to minimize run times.

Various meshes were evaluated and the radial forces compared to determine an appropriate mesh density. If the changes in forces between mesh densities is less than 5% it was assumed that the model is reasonable and sufficient. This 5% criterion is arbitrary but should be sufficient for comparisons with the experimental results. Also, when comparing results among simulation models, the change in the results as a function of mesh density or element size is not as critical since the same mesh is being used for all the models.

The initial global element size was 10-mm and was subsequently reduced to 2.5-mm. The highest deformation case will be evaluated as worst case, which is when the distal shape is inside the smallest tube diameter of 2-mm. Coil A will be used for this evaluation since it is

typical of the three designs being evaluated. Friction will also be assumed to be zero or frictionless for this case but will be evaluated later.

4.4.2 MESH REFINEMENT RESULTS

The total radial force and maximum radial force were determined for various global element or mesh sizes. The mesh size started at 10-mm and was progressively decreased to 2.5-mm. Table 4-4 lists the radial forces and their change as a function of mesh size.

Table 4-4 Mesh Refinement Results

Global Element Size	Total Radial Force	Total Radial Force Change from Preceding Element Size	Maximum Radial Force	Maximum Radial Force Change from Preceding Element Size
(mm)	(N)	(%)	(N)	(%)
10 mm	0.186	NA	0.0662	NA
7.5 mm	0.201	8.2	0.0683	3.3
5.0 mm	0.199	-1.0	0.0655	-4.1
2.5 mm	0.195	-2.2	0.0653	-0.4

Figure 4-5 is a plot of the data in Table 4-4 and shows that the change between meshes is small as mesh refinement is increased.

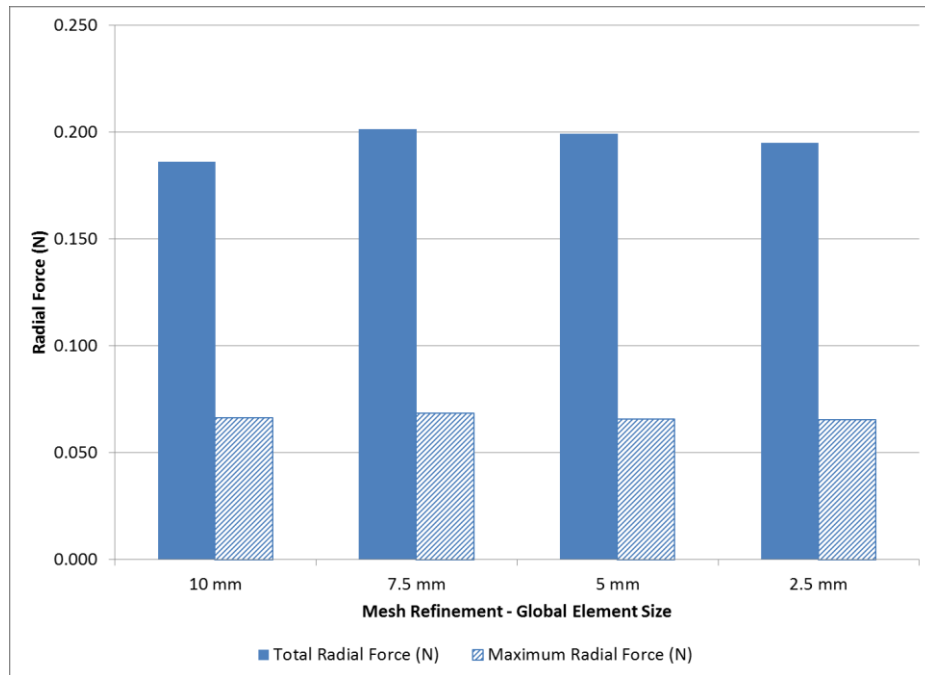


Figure 4-5 Comparison of Radial Forces with Global Element Size

A plot of the deformed distal shape (Figure 4-6) shows that the initial circular distal shape does not uniformly conform to the 2-mm tube after insertion but instead contacts the tube at four different locations. The distal shape contacts the tube in the same plane as does the initial circular shape. The deformation plot also shows the location and direction of the radial forces.

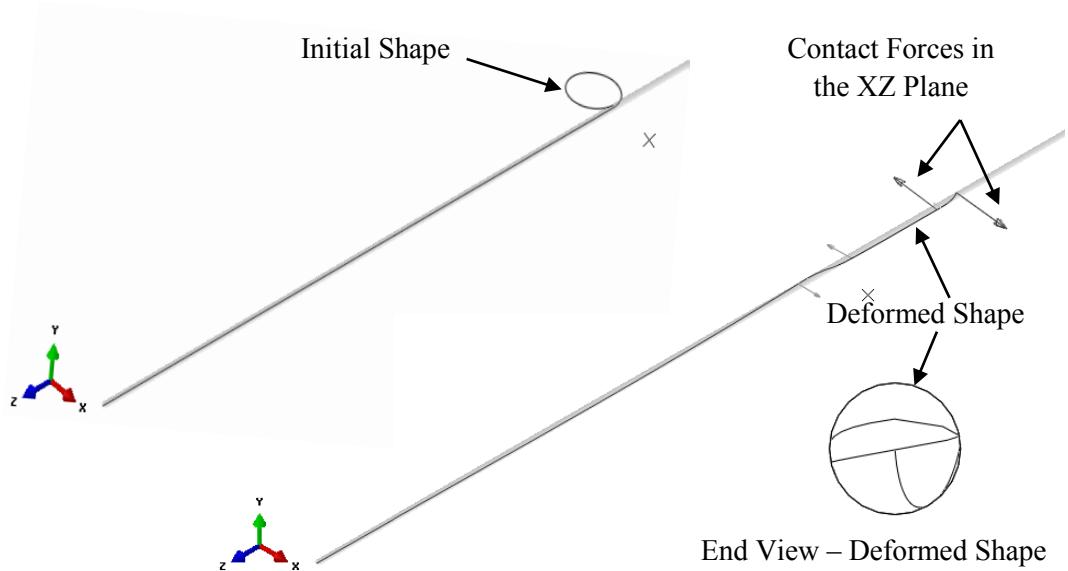


Figure 4-6 Deformed Distal Shape with Contact Forces – Coil A (2-mm Diameter Tube)

Figure 4-7 shows a plot of the radial force magnitude along the distal end of the model (z-axis). This line plot displays the radial force at each nodal location and then connects each data point with a line for visualization. The total radial force is the sum of all the radial forces along the distal end at these nodal locations. Only the 2.5- and 10-mm global element sizes are shown to maintain clarity. This plot also shows that the maximum radial force occurs at the tip of the distal shape.

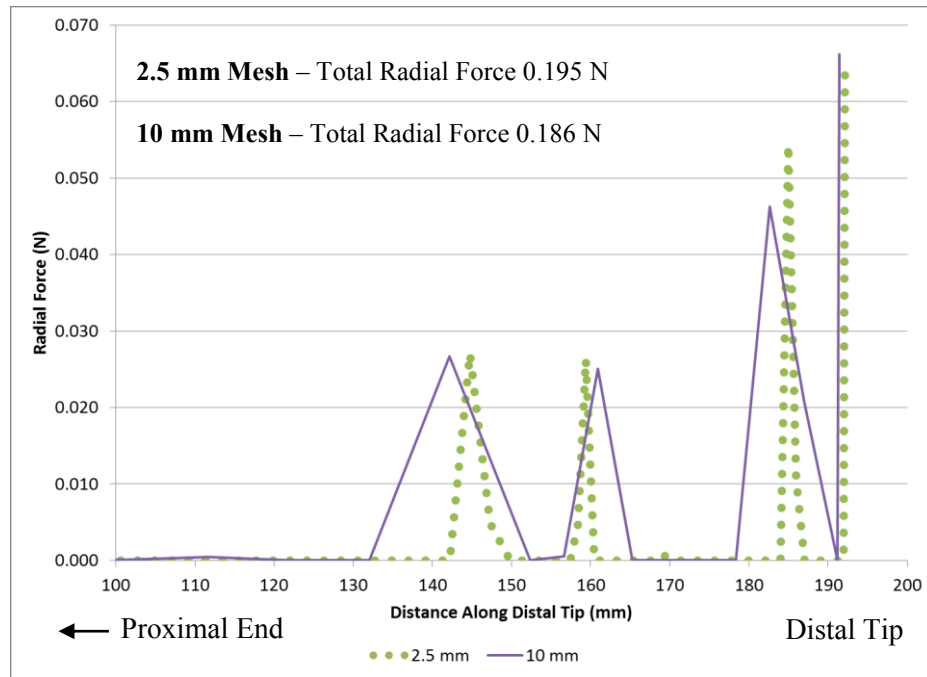


Figure 4-7 Radial Force Distribution along the Axial Direction (Mesh Refinement)

The global element size results (Table 4-4) start at 10.0-mm and show that when the element size is reduced from 7.5- to 5.0- mm the change in total radial force is -1.0 % which meets the criterion of less than 5%. For the maximum radial force, when the element size is reduced from 10- to 7.5-mm, the change is 3.3 % which meets the criterion of less than 5%. Since total radial force requires a smaller element size, 5.0-mm, to meet this criterion, a global element size of 5.0-mm or less will be used for subsequent models.

4.5 FRICTION EVALUATION

4.5.1 FRICTION BACKGROUND INFORMATION

Friction between the distal shape and the rigid tube was evaluated to determine its effect on radial force. Coefficients of friction are difficult to determine and are affected by many

variables, contact pressure, humidity, lubricants, surface finish, velocity, and temperature.

The friction conditions between *in-vivo* and *in-vitro* conditions are very different. The present evaluation is only to determine how sensitive the model is to friction and to gain a general understanding of its effect.

Coefficients of friction between two materials can vary widely [42, 43]. Static coefficients of friction were tentatively assigned as 0.1, 0.5, and 1.0 to compare with the frictionless model. These friction values cover a wide range of materials and conditions. The frictionless model may be more appropriate since for lead design, it is desirable to have the lowest coefficient of friction possible to allow easy delivery as it slides through the veins for implantation and to avoid abrasion with tissue and other leads [44 – 46].

To evaluate the friction effect, a simulation model of the distal shape interacting with a 6-mm tube was chosen. The 6-mm tube diameter was chosen since it is between the minimum, 2-mm, and maximum, 8-mm, tube sizes. Coil A will be used for this evaluation since it is typical of the three designs being evaluated.

4.5.2 FRICTION RESULTS

The total radial force and maximum radial force were determined for various coefficients of friction. The initial model was frictionless and then the friction coefficient was increased. Table 4-5 lists the radial forces and their changes as the coefficient of friction is increased.

Table 4-5 Friction Evaluation Results

Static Coefficient of Friction	Total Radial Force (N)	Total Radial Force Change from Frictionless (%)	Maximum Radial Force (N)	Maximum Radial Force Change from Frictionless (%)
Frictionless	0.141	NA	0.0406	NA
0.1	0.114	-19	0.0369	-9
0.5	0.076	-46	0.0288	-29
1.0	0.056	-60	0.0235	-42

The addition of friction to the simulation model reduces the radial forces. As the coefficient of friction increases the total and maximum radial forces decrease. Figure 4-8 displays the data in Table 4-5 and shows how friction reduces both the total radial force and maximum radial force. The friction has more of a reduction on the total radial force than on the maximum radial force.

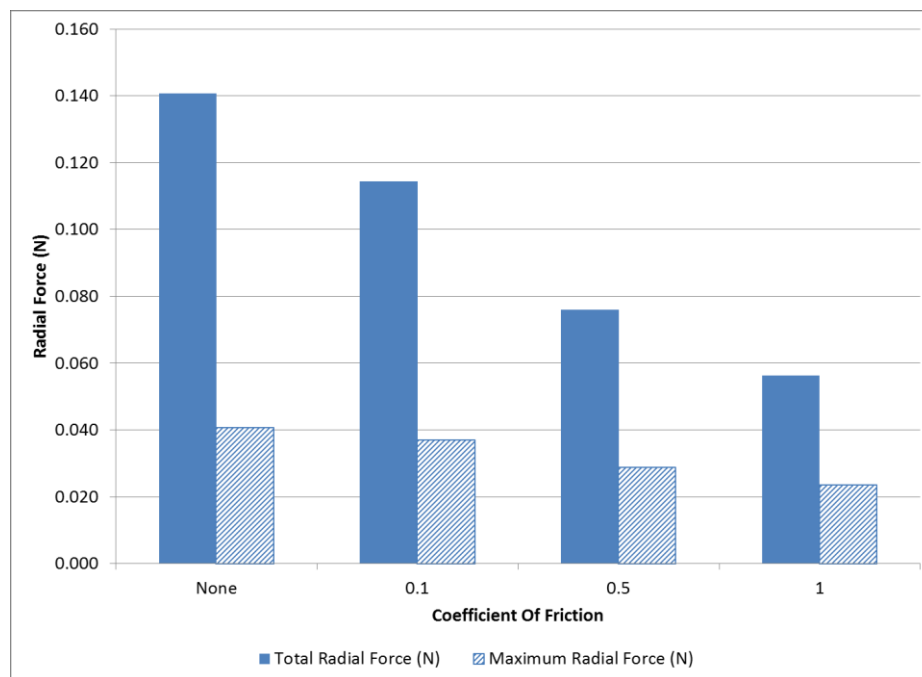
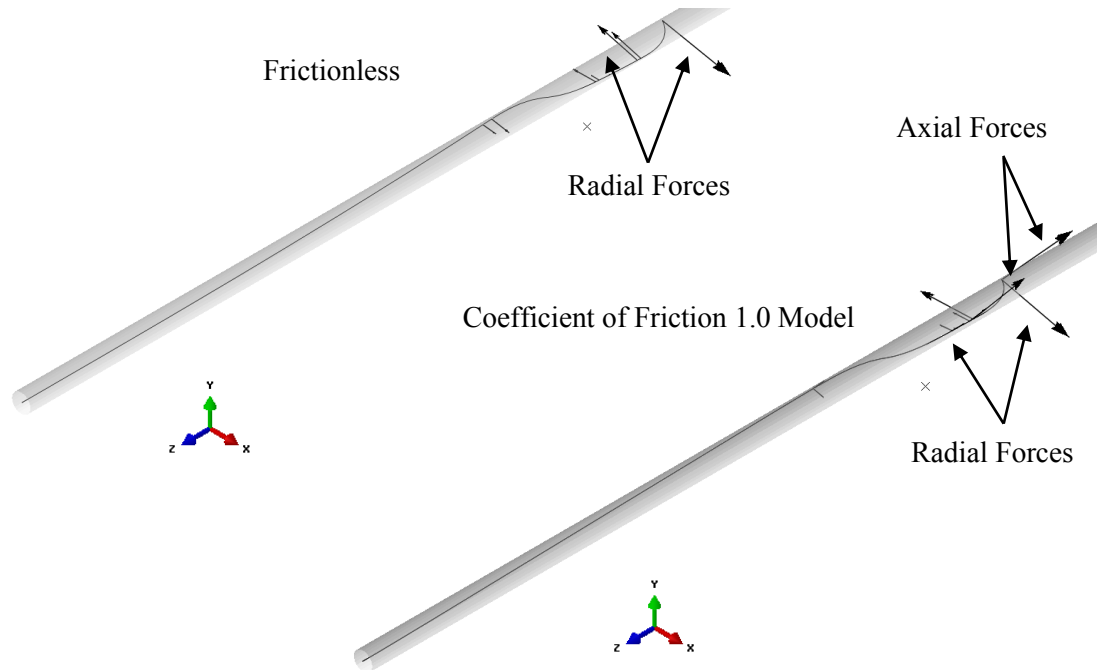


Figure 4-8 Comparison of Radial Forces for Different Coefficients of Friction

A plot of the deformed shape (Figure 4-9) shows that the deformed distal shape is similar with or without friction. Without friction the only contact forces interacting with the tube act radially. Friction creates shear forces at the tube contact surface which act in the axial direction which reduce the radial forces.



**Figure 4-9 Deformed Distal Shape with Contact Forces for Coil A (6 -mm Diameter Tube)
(Deformed Model with and without Friction)**

Figure 4-10 shows a plot of the radial force magnitude along the distal end of the model (z-axis). This line plot displays the radial force at each nodal location and then connects each data point with a line for visualization. The total radial force is the sum of all the radial forces along the distal end at these nodal locations. Only two models (frictionless and friction with a coefficient of 1.0) are shown for clarity. Again this plot shows that the maximum radial force occurs at the tip of the distal shape. Figure 4-10 shows that friction decreases the radial forces

that the distal shape exerts on the tube. With friction, the radial force is distributed further towards the proximal end and the location of the forces changes.

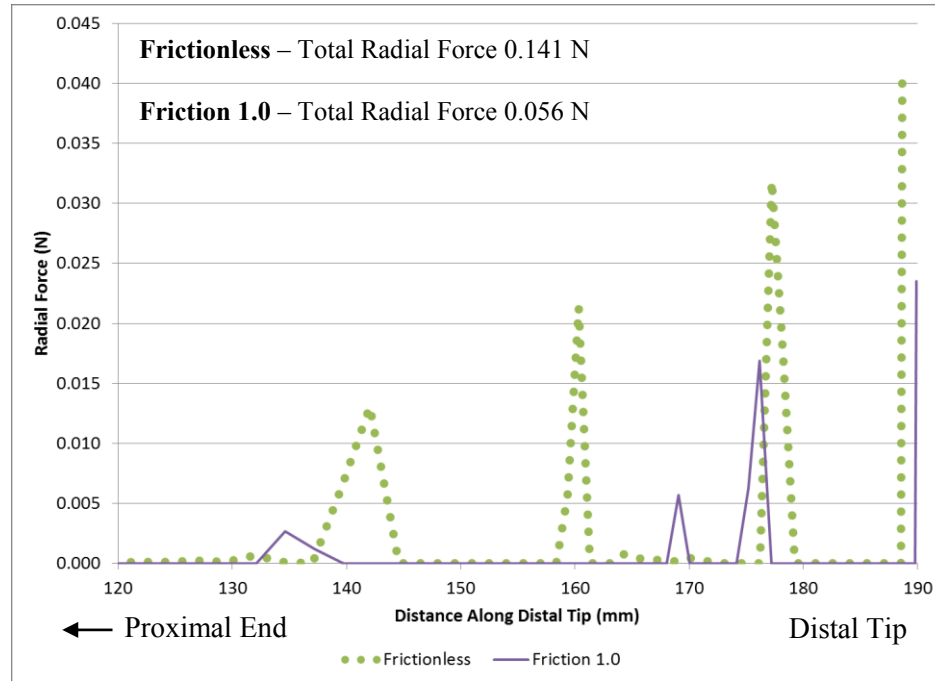


Figure 4-10 Radial Force Distribution along the Axial Direction with and without Friction

Strain energy explains why friction reduces the radial forces that the distal shape exerts on the tube. In the frictionless case, most of the strain energy occurs in bending as the distal shape pushes radially on the tube. With friction, the strain energy is distributed between bending and axial stretching of the distal shape. The axial forces are due to the shear forces inherent in friction. Figure 4-9 illustrates these shear forces acting along the axis of the tube (z-axis). These shear forces axially stretch the distal shape further than the frictionless model. This stretching is shown in Figure 4-10 by the proximal-end radial force being shifted towards the proximal end of the model. Both models have similar amounts of strain energy in their

deformed states but friction reduces the amount of strain energy available for bending so that some of this strain energy is used to axial stretch the model in its final state.

For subsequent models, the interface between the distal shape and the tube will be assumed frictionless. This assumption is made since the purpose of the models is to evaluate distal shape designs and compare them to each other. Another reason is that determining the correct coefficient of friction to use for these simulation models is highly error prone. Also, the goal of most lead designs is to achieve a low friction design for easy sliding through the veins during implantation and to avoid abrasion with tissue and other leads [44 – 46].

4.6 PROXIMAL STRAIGHT-END LENGTH EVALUATION

4.6.1 PROXIMAL STRAIGHT-END LENGTH BACKGROUND

For both the experimental samples (Section 3.3.2) and the simulation models (Section 4.3), the end of the proximal straight length is held and fixed in position. The length of the proximal end should be long enough that the proximal end does not influence distal-tip radial forces. In the simulation model, the proximal end will be prevented from moving by setting all degrees of freedom, DOF, to zero. Various proximal straight end lengths were evaluated and the radial forces compared to determine an appropriate length. If the change in radial forces for successively prescribed lengths is less than 5% the model will be assumed to be reasonable and sufficient. This 5% criterion is arbitrary but should show reasonable agreement with the experimental results.

Proximal straight-end lengths of 25-, 75-, and 150-mm were evaluated. A simulation model with the distal shape interacting with a 6-mm diameter tube was chosen. The 6-mm diameter tube size was chosen since it is between the minimum, 2-mm diameter, and maximum, 8-mm diameter, tube sizes. Coil A will be used for this evaluation since its stiffness is similar to the three designs being evaluated. The coefficient of friction was assumed to be zero.

4.6.2 PROXIMAL STRAIGHT-END LENGTH RESULTS

The total radial force and maximum radial force were determined for various proximal straight-end lengths. The initial proximal straight-end length was 25-mm long, and then it was increased to 150-mm. Table 4-6 lists the radial forces and their change as proximal straight-end length is increased.

Table 4-6 Proximal Straight-End Length Results

Proximal Straight-End Length	Total Radial Force	Total Radial Force Change from Preceding Length	Maximum Radial Force	Maximum Radial Force Change from Preceding Length
(mm)	(N)	(%)	(N)	(%)
25	0.122	NA	0.040672	NA
75	0.140	14.8	0.040609	0.02
150	0.141	0.7	0.040614	0.00

The proximal straight-end length change from 75- to 150-mm met the criterion of a less than 5% change in the total radial force. Figure 4-11 displays the data in Table 4-6 and shows that after the proximal straight-end length increases above 75-mm the radial forces change less than 1%. The maximum radial force occurs at the distal tip (Figure 4-12) and is not affected by the length change since it is the farthest point away from the proximal end.

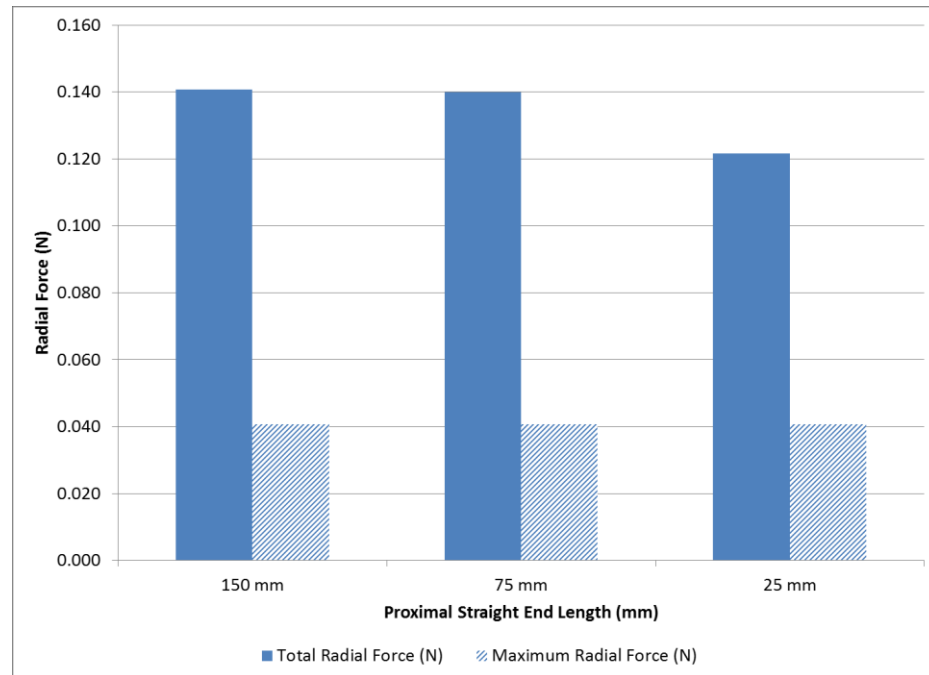


Figure 4-11 Comparison of Distal-End Radial Forces with Proximal Straight-End Length

Figure 4-12 shows a plot of the radial force magnitude along the distal end of the model along (z-axis). This line plot displays the radial force at each nodal location and then connects each data point with a line for visualization. The total radial force is the sum of all the radial forces along the distal end at these nodal locations. The change in the proximal straight end length has little effect on the radial forces at the distal end. The effect on the proximal end of the distal shape (25- to 55-mm range in Figure 4-12) can be significant. For a very short length (25-mm), a radial force of 0.004 N is obtained from the model at the 40-mm location while for other longer proximal end lengths radial forces at the 35-mm location are significantly higher at 0.013 N. This plot also shows that the maximum radial force occurs at the tip of the distal shape.

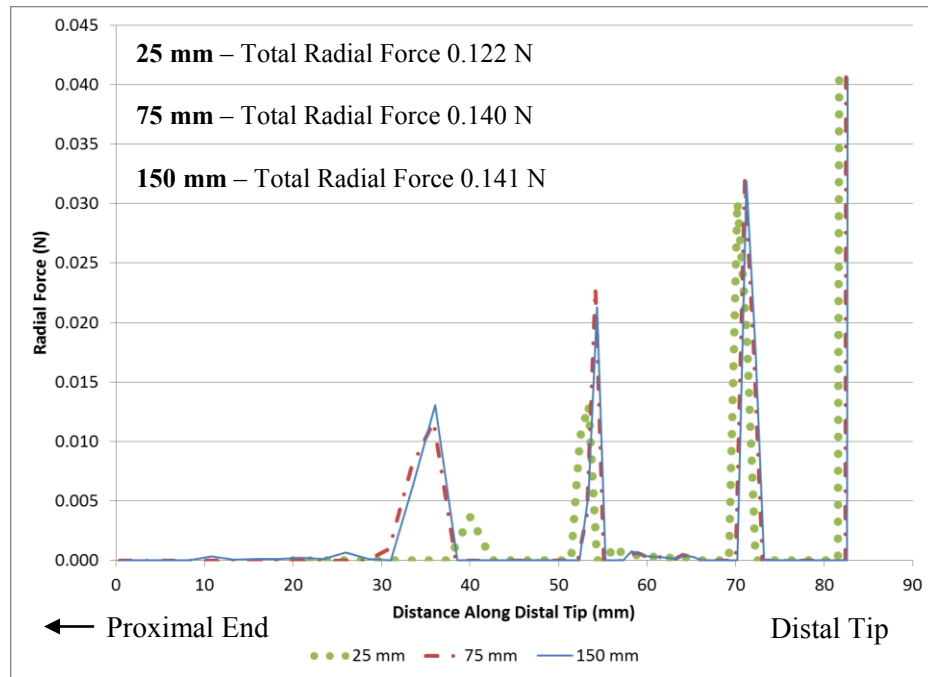


Figure 4-12 Radial Force Distribution along the Axial Direction for Parametric Values of the Proximal Straight-End Length

The proximal straight-end length results (Table 4-6) start at length of 25-mm and show that when the length is increased from 75- to 150-mm the change in total radial force is 0.7% which meets the criterion of less than 5%. For the maximum radial force, when the proximal straight end length is increased from 25- to 75-mm, the change is 0.02% which meets the criterion of less than 5%. Since the total radial force requires a longer proximal end, a length of 150-mm will be used for subsequent models.

4.7 EXPERIMENTAL VALIDATION OF SIMULATION MODEL

4.7.1 EXPERIMENTAL VALIDATION BACKGROUND

A simulation model was used to evaluate the radial force of the distal shape and compared with the previous experimental results (Section 3.4). The model was based upon the previous

evaluations on mesh refinement (Section 4.4), friction (Section 4.5), and proximal straight-end length (Section 4.6). The three coil designs were modeled using a global element size of 2.5-mm. The models were frictionless and the proximal straight-end length was 150-mm. These assumptions are based on the results of the previous sections to allow comparisons among designs. For the simulation model, radial force measurements were extracted at discrete tube diameters of 2-, 4-, 6-, and 8-mm.

4.7.2 EXPERIMENTAL VALIDATION OF SIMULATION MODEL RESULTS

In the simulation model, the deformed geometry and radial forces were determined for all three coil designs at discrete tube diameters of 2-, 4-, 6-, and 8-mm. The simulation model simulates the experiment completed in Chapter 3. Figure 4-13 shows a plot of the deformed geometry for Coil A at various tube diameters. The left side of Figure 4-13 shows an isometric view of the deformed mode with a corresponding end view (not to scale) on the right. The tube prevents the distal shape from returning to its initial two-dimensional circular shape (Figure 4-6). The end view shows that as the tube increases in diameter, the distal shape starts to take on a three-dimensional shape conforming and pushing against the tube. This deformed shape is similar for all three coil designs (Coil A, B, and C).

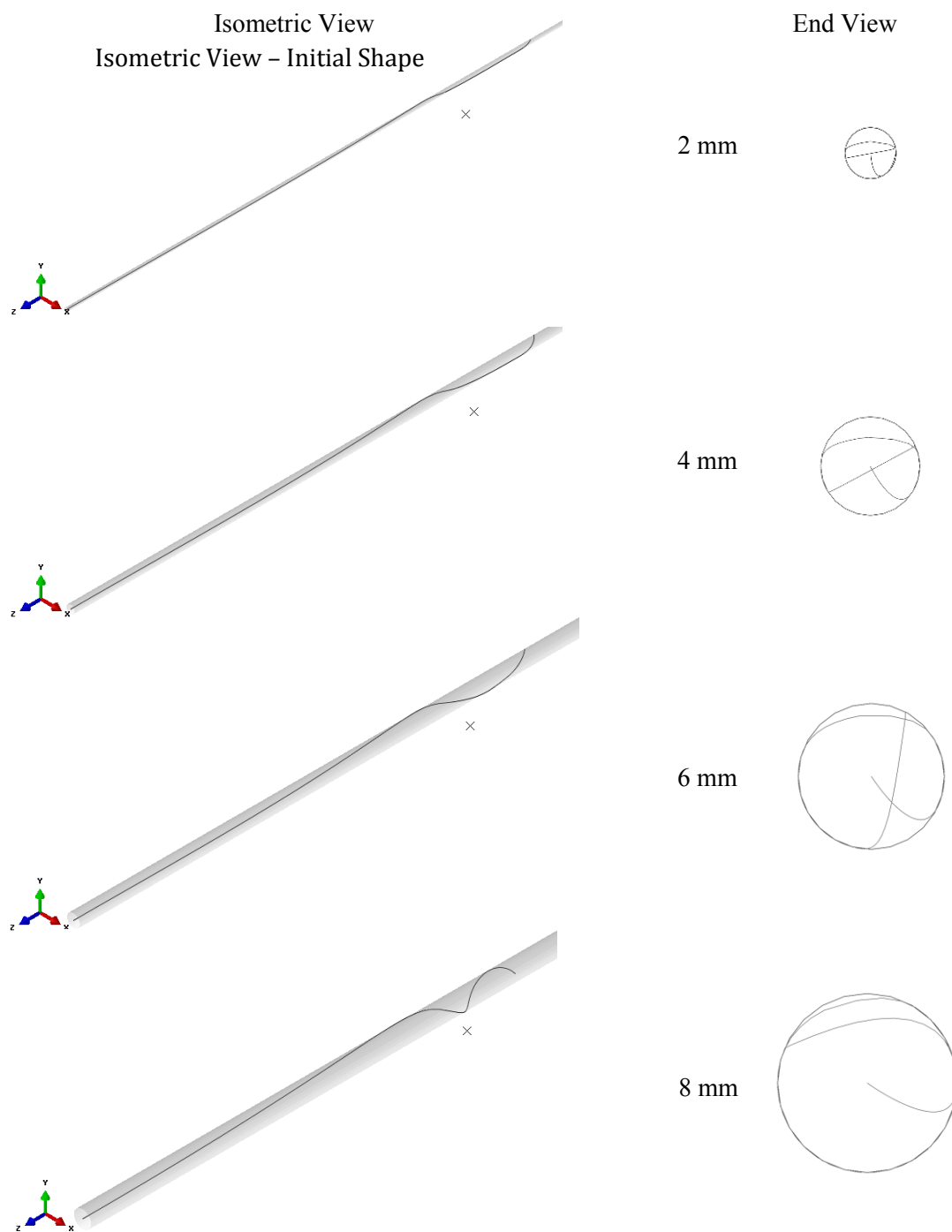


Figure 4-13 Deformed Distal Shape for Various Tube Diameters (Coil A)

The total radial force and maximum radial force were determined for all three coil designs at discrete tube diameters of 2-, 4-, 6-, and 8-mm. Table 4-7 lists the total radial force and how the total radial force decreases from Coil A to Coil C. The change in total radial force matches the change in stiffness among designs as shown previously in Table 4-3 which shows that Coil A is stiffer than Coil B and Coil B is stiffer than Coil C.

Table 4-7 Total Radial Force – Coil Design vs. Tube Diameter

Coil Design	2-mm	4-mm	6-mm	8-mm	Change from Coil A (%)
	(N)	(N)	(N)	(N)	
Coil A	0.195	0.136	0.141	0.237	NA
Coil B	0.151	0.106	0.111	0.189	22%
Coil C	0.126	0.088	0.092	0.158	35%

Figure 4-14 displays the data of Table 4-7 and shows how the coil design and tube diameter affect the total radial force. The radial force decreases from 2- to 4-mm and this is the result of the initial distal shape being allowed to expand further in the larger 4-mm tube. The models then show the radial forces increase with larger diameters after 4-mm. The plot of deformed geometry in the 6- and 8-mm diameter tube in Figure 4-13 suggests that this increase in radial force from 6- to 8-mm diameter tube in may be due to the distal shape within the tube changing from a two-dimensional shape to a conforming three-dimensional shape.

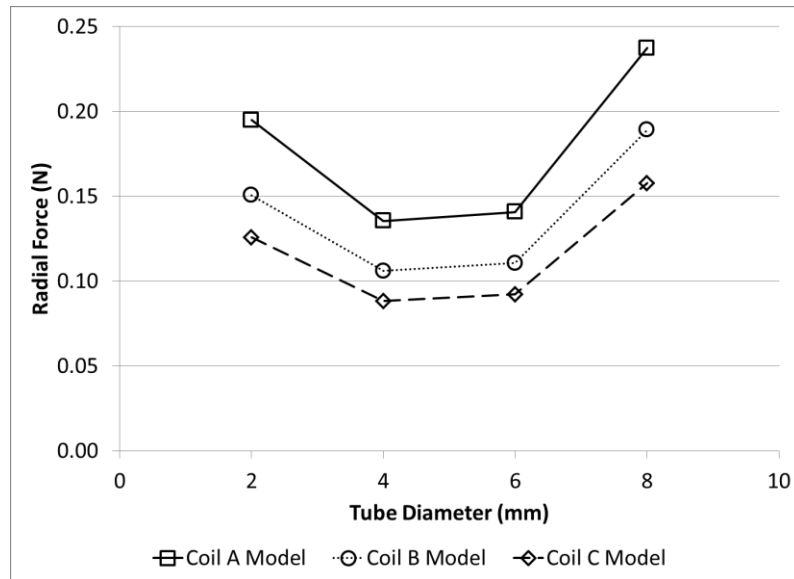


Figure 4-14 Comparison of Total Radial Force with Coil Design and Tube Diameter

Table 4-8 lists the maximum radial forces and their change as compared to Coil A. The change in the maximum radial force matches the change in stiffness among, designs as shown previously in Table 4-3.

Table 4-8 Maximum Radial Force (Distal Tip) – Coil Design vs. Tube Diameter

Coil Design	2-mm (N)	4-mm (N)	6-mm (N)	8-mm (N)	Change from Coil A (%)
Coil A	0.065	0.045	0.041	0.054	NA
Coil B	0.051	0.035	0.032	0.039	23%
Coil C	0.042	0.029	0.026	0.032	36%

Figure 4-15 exhibits the data in Table 4-8 and shows how the coil design and tube diameter affect the maximum radial force. The maximum radial force decreases from 2- to 6-mm and then increase with larger diameters greater than 6-mm.

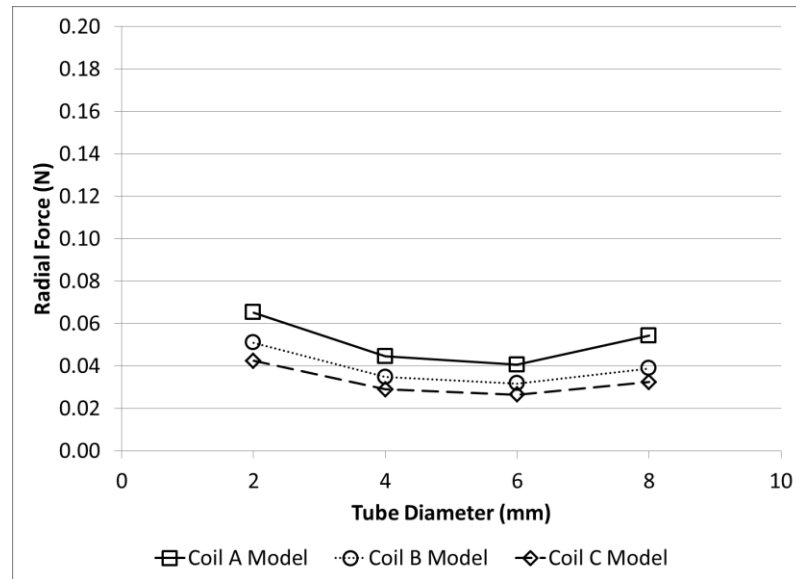


Figure 4-15 Comparison of Maximum Radial Force with Coil Design and Tube Diameter

Figure 4-16 shows a plot of the radial force magnitude along the distal end of the model (z-axis) for Coil A. This line plot displays the radial force at each nodal location and then connects each data point with a line for visualization. The total radial force is the sum of all the radial forces along the distal end at these nodal locations. For the tube diameters of 2-, 4-, and 6-mm, the maximum radial force is at the distal tip on the right side of the plot. Although not shown, all trends for Coil A are similar to those for Coil B and C. Figure 4-16 shows that distal shape contacts the tube at four points for the tube diameters of 2-, 4-, and 6-mm. For the 8-mm diameter tube, the radial force changes from four distinct contact points to multiple contact points with a pressure distributed from 160- to 170-mm. Also, the maximum radial force occurs away from the distal tip. With a larger tube diameter, the distal shape can expand more radially which allows the distal shape to retract axially or shrink in the z-axis.

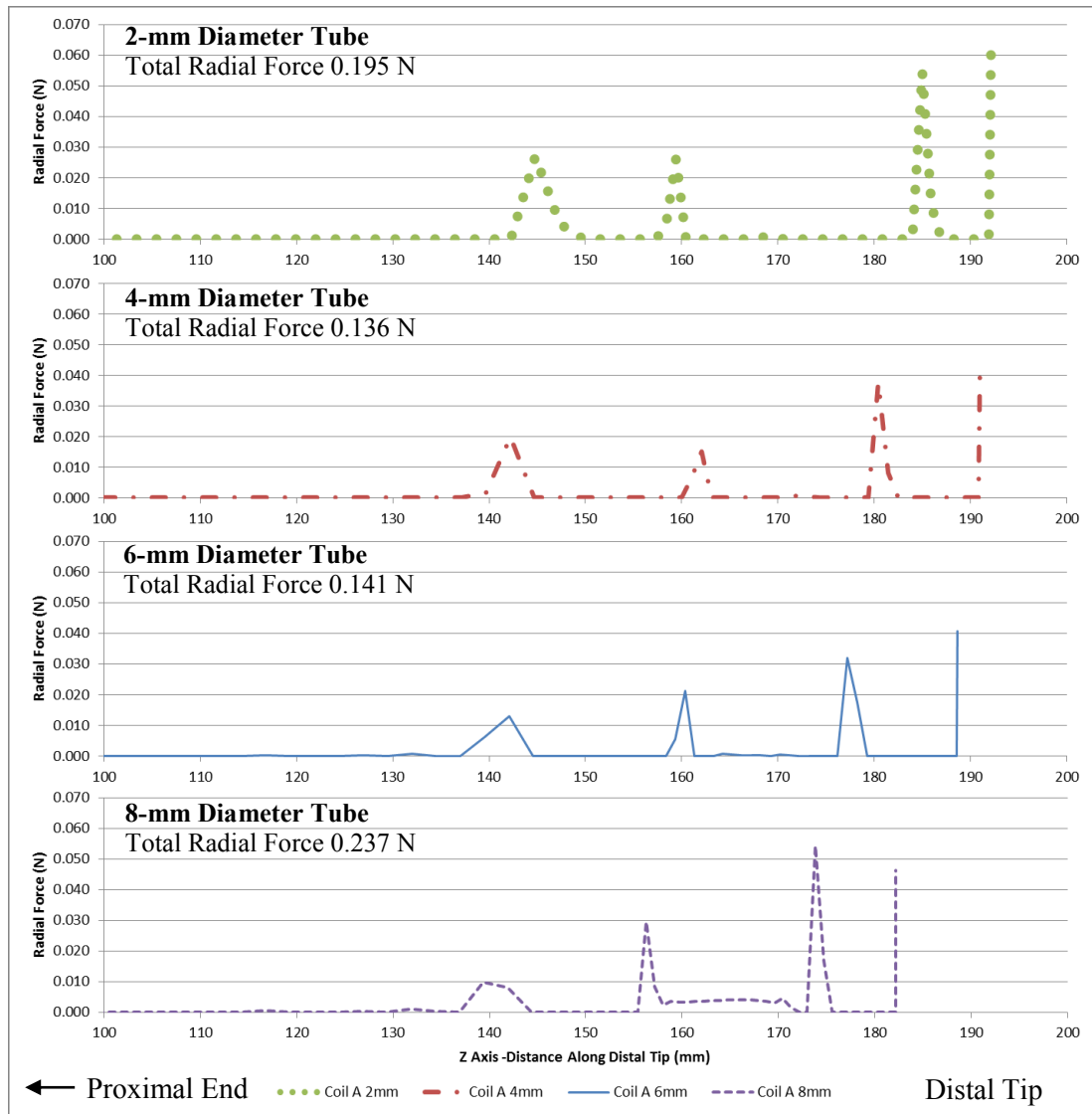


Figure 4-16 Radial Force Distribution along the Axial Direction (Coil A)

Table 4-9 lists the length of contact between the distal shape and the tube. Note that this contact length is taken along the tube axis and not along the distal shape. Therefore for the large tube diameters where the distal shape conforms to the tube, this contact length could be

underestimated. The increase in contact length as tube diameter increases indicates that the distal shape conforms to the tube.

Table 4-9 Axial Tube Length of Contact – Coil Design vs. Tube Diameter

Coil Design	2-mm (mm)	4-mm (mm)	6-mm (mm)	8-mm (mm)
Coil A	22.1	38.3	45.3	52.1
Coil B	24.6	38.3	46.3	51.9
Coil C	24.6	38.3	45.3	51.9

The total radial force for each coil design as predicted by simulation was then compared to experimental results from Chapter 3. Figure 4-17 through Figure 4-19 compare the experimental total radial force with that from the simulations. Inspection of these figure show that both the numerical predictions and the experimental radial forces decrease in the range of tube diameter from 2- to 4-mm but for tube diameters in the 4- to 6-mm range simulation results show higher radial force increase from 6- to 8-mm, but the experimental results show a decrease in that range. The figures also reveal that the experimental results display both contraction and expansion of the radial force as described in Section 3.3.3.

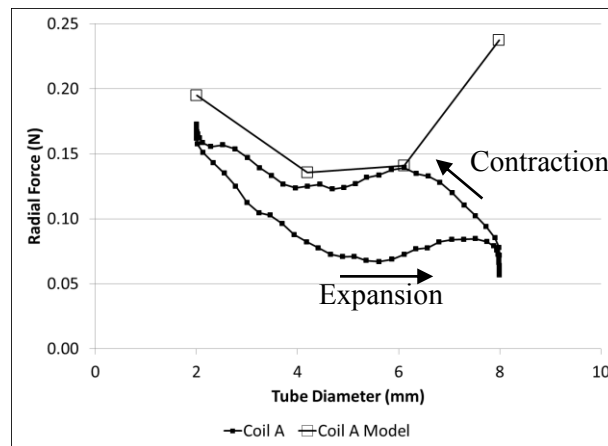


Figure 4-17 Total Radial Force Simulation Model and Experimental (Coil A)

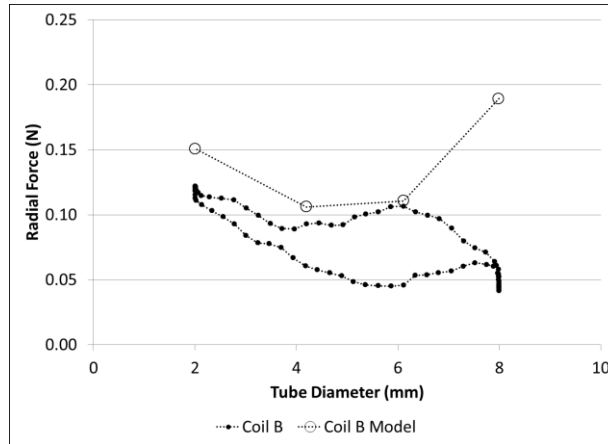


Figure 4-18 Total Radial Force Simulation Model and Experimental (Coil B)

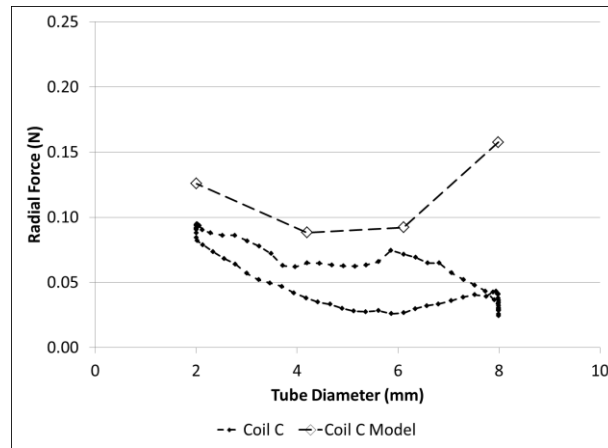


Figure 4-19 Total Radial Force Simulation Model and Experimental (Coil C)

As shown on the right side in Figure 4-13, the simulation model shows a three-dimensional deformed shape in the 8-mm tube. When the tube diameter changes from 4- to 8-mm, the deformed distal shape of the model transitions from a two-dimensional shape that is primarily in bending to a three-dimensional shape that is both in bending and torsion. The higher total radial force in the 8-mm tube could be due to the increase in strain energy from the addition of torsional strain along with the bending strain. The lack of higher radial forces in the

experimental results for the 8-mm diameter may be that the experimental samples did not transition from a two-dimensional deformed distal shape to a three-dimensional shape. The simulation models are frictionless but friction does exist in the experimental setup between the silicone tubing and the radial force tester. Friction between the samples and the mechanical tester could have prevented this three-dimensional deformed distal shape from occurring which would result in lower forces. The friction evaluation completed in Section 4.5 showed that friction will reduce the radial forces.

As noted earlier, the experimental measurements show both contraction and expansion of the mechanical iris (see Figure 4-17 through Figure 4-19). The contraction and expansion radial force values at 2-, 4-, 6-, and 8-mm were averaged and then compared to the simulation model predictions in Figure 4-20 through Figure 4-22 to directly compare the experiment to the simulation model. A numerical comparison of the same information is presented in Table 4-10 through Table 4-12.

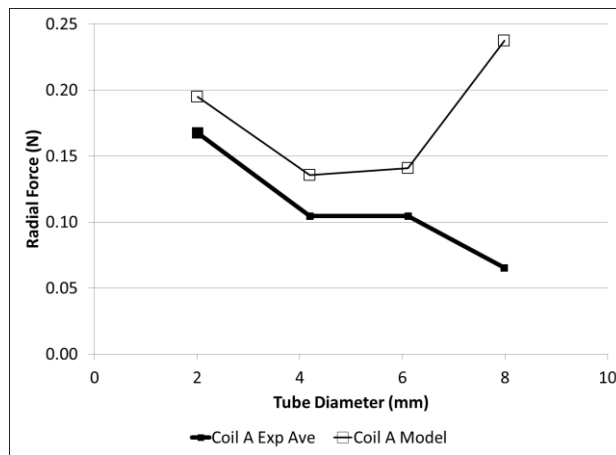


Figure 4-20 Total Radial Force Simulation Model and Experimental Average (Coil A)

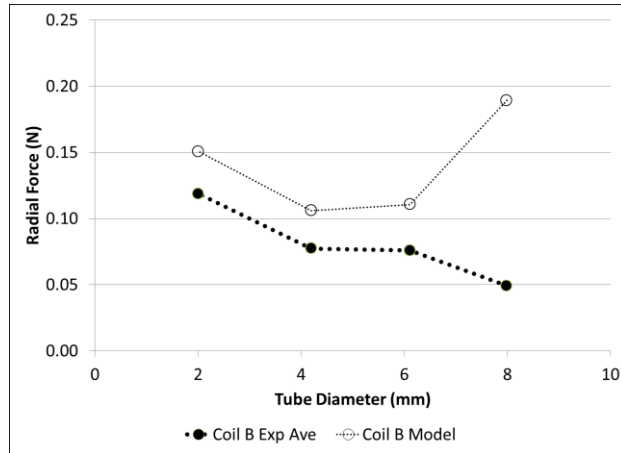


Figure 4-21 Total Radial Force Simulation Model and Experimental Average (Coil B)

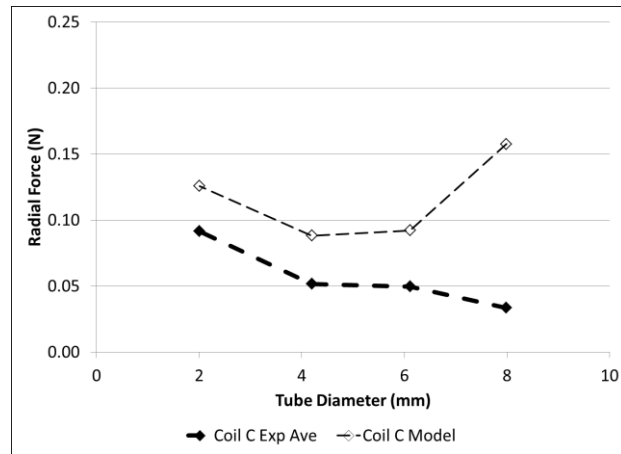


Figure 4-22 Total Radial Force Simulation Model and Experimental Average (Coil C)

Table 4-10 Total Radial Force Simulation Model vs. Experimental Average (Coil A)

Tube Diameter (mm)	Simulation Model (N)	Experimental Average (N)	Change from Experimental (%)
2	0.195	0.167	16
4	0.136	0.105	30
6	0.141	0.105	35
8	0.237	0.065	263

Table 4-11 Total Radial Force Simulation Model vs. Experimental Average (Coil B)

Tube Diameter (mm)	Simulation Model (N)	Experimental Average (N)	Change from Experimental (%)
2	0.151	0.119	27
4	0.106	0.077	37
6	0.111	0.076	46
8	0.189	0.049	284

Table 4-12 Total Radial Force Simulation Model vs. Experimental Average (Coil C)

Tube Diameter (mm)	Simulation Model (N)	Experimental Average (N)	Change from Experimental (%)
2	0.126	0.092	37
4	0.088	0.052	71
6	0.092	0.050	86
8	0.158	0.034	369

With regard to the tabulated results, it may be noted that the stiffness of the coils decreases from Coil A to Coil C. The radial force results also decrease from Coil A to Coil C for both the experiment and the simulation model (Table 4-10 through 4-12). For the smaller tube diameters (2- to 6-mm) the simulation models and experiment show a decrease in radial forces.

The difference between the simulation model and the experimental results (Table 4-10 through 4-12) varies from 16% to 86% for the tube diameters from 2- to 6-mm. When comparing the differences between coil designs, or stiffness, the lower stiffness coil design (Coil C) has larger differences between the simulation model and experiment. This could be attributed to the simulation model allowing a three-dimensional deformed distal shape versus the experiment with friction that allows the deformed distal shape to remain two-dimensional.

The three-dimensional deformed distal shape conforms to the curved tube wall allowing higher radial forces in the simulation model versus the experiment.

Figure 4-20 through 4-22 show that for the 8-mm tube diameter the radial forces for the simulation model increase and deviate from the experimental results which decrease. The difference between the simulation model and experiment radial forces increases to 263% to 369% for an 8-mm tube diameter. The lack of friction in the simulation model could cause this deviation from experiment if the simulation model allows the distal shape to revert to a three-dimensional shape instead of a two-dimensional one.

4.7.3 SIMULATION MODEL UPDATED WITH FRICTION

The frictionless simulation model of the distal shape deviated from the experimental at larger tube diameters. To determine if the lack of friction is the cause for this discrepancy, the simulation models of Coil A were reevaluated with friction. Ideally, it would be desirable to determine the coefficient of friction directly from the test setup, but the original setup is not available and the coefficients of friction are difficult to determine. Another approach is to use the friction evaluation results of Section 4.5 to estimate the coefficient of friction within the experimental setup.

Coil A will be reevaluated with friction and compared with experimental results. Coil A was chosen since it was used in the friction evaluation of Section 4.5 when friction was varied for Coil A in a 6-mm tube. Review of Table 4-5 showed that with a coefficient of friction of 0.1

to 0.5 the total radial force of the simulation model (0.114 to 0.076 N) almost matched the experimental measurement (0.105 N) for the 6-mm tube.

4.7.4 SIMULATION MODEL RESULTS WITH FRICTION

The total radial force was determined for Coil A with an assumed coefficient of friction of 0.1 and 0.5 for the tube diameters and compared to the experiment. Table 4-13 shows the simulation model with a coefficient of friction of 0.5 is within 5% of the experimental measurements, except for the 6-mm tube diameter.

Table 4-13 Total Radial Force with Simulation Model Updated with Friction (Coil A)

Tube Diameter	Experimental Average	Simulation Model Frictionless	Simulation Model Coefficient of Friction 0.1	Simulation Model Coefficient of Friction 0.5	Difference between Experimental and Model with 0.5 Coefficient of Friction
(mm)	(N)	(N)	(N)	(N)	(%)
2	0.167	0.195	0.187	0.163	-2
4	0.105	0.136	0.124	0.100	-5
6	0.105	0.141	0.114	0.076	-27
8	0.065	0.237	0.135	0.068	4

Figure 4-23 displays the data in Table 4-13 and shows how the simulation models with friction match the experimental measurements. The model with the 0.5 coefficient of friction matches the best and shows the decrease in radial force at 8-mm that is shown in the experimental measurements.

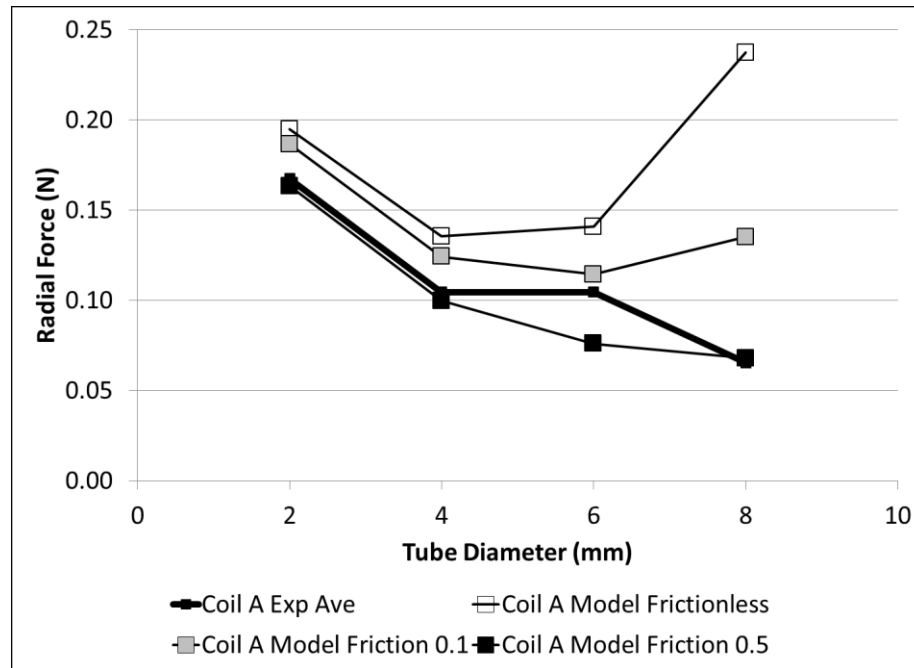


Figure 4-23 Total Radial Force Simulation Model with Friction and Experimental Average

Figure 4-24 shows the deformed distal shape for the three different coefficient of friction of Coil A. The isometric view of the frictionless model shows that the deformed distal shape conforms to the tube in the shape of a three-dimensional spiral for the frictionless case. Friction causes the deformed shape to contact the tube in a two-dimensional shape with lower radial force. As discussed in Section 4.5.2, strain energy explains why friction reduces the radial forces on the deformed shape since friction prevents the distal shape from sliding and conforming to the tube in a three-dimensional shape. The three-dimensional spiral shape adds torsional twisting to the deformed shape. The conforming shape of the distal shape influences the total radial force exerted against the tube.

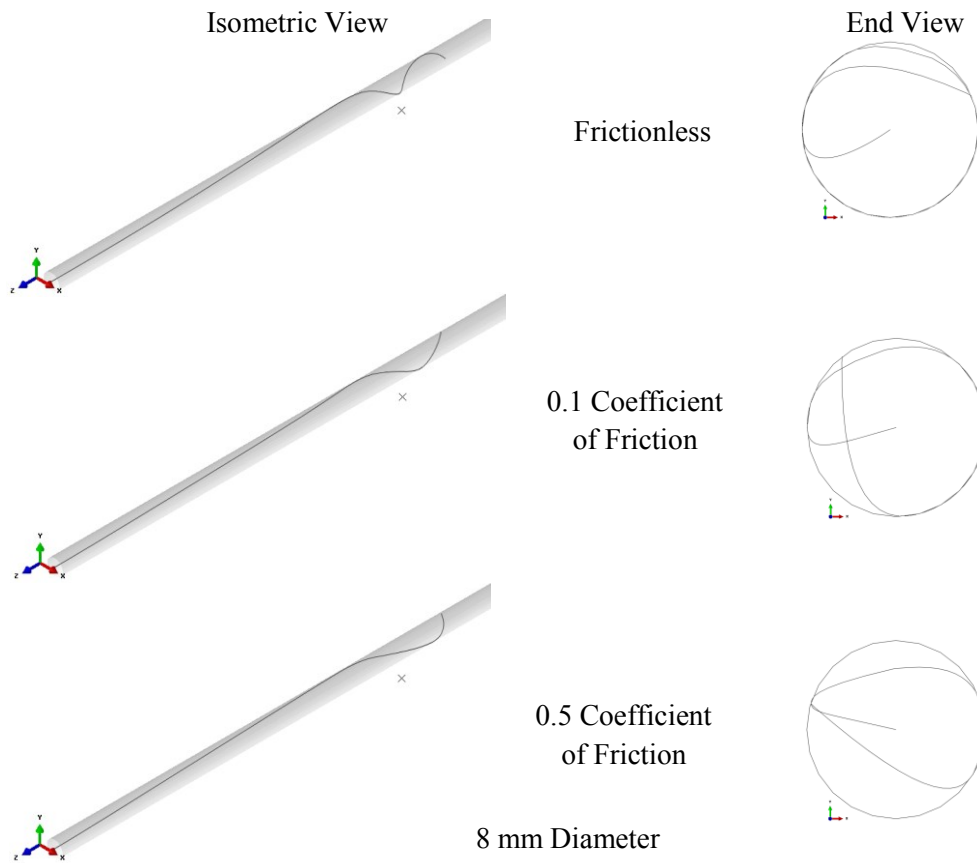


Figure 4-24 Deformed Distal Shape for Various Coefficients of Friction (Coil A)

4.8 SIMULATION MODEL FOR SPIRAL EVALUATION

4.8.1 SIMULATION MODEL FOR SPIRAL EVALUATION BACKGROUND

A goal for the distal shape is to achieve high radial forces for fixation and a low distal tip force. The previous section showed the radial forces for a distal shape pre-formed into a two-dimensional circular shape. The results showed that when the deformed shape was three-dimensional, whether due to a larger tube diameter or friction, higher radial forces were

exerted. These results indicate a pre-formed distal spiral shape or helix as being desirable to achieve higher radial forces.

The spiral distal shape was modeled as a helix with a given radius, r_{spiral} , and pitch, P_{spiral} .

Figure 4-25 shows what a helix looks like in three-dimensional space.

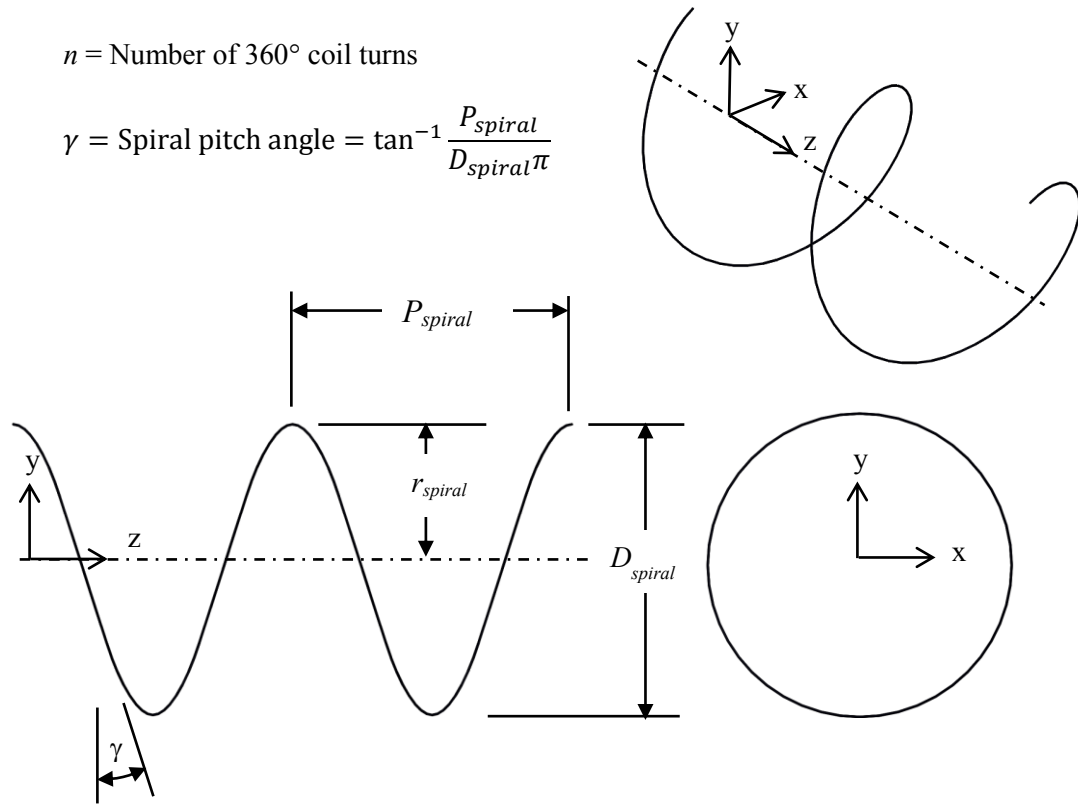


Figure 4-25 Helix Geometry

A helix is mathematically defined by Eq. (4-1) [47, 48]. The domain of this function is denoted with t which represents time.

$$x = r_{spiral} \cos t \qquad y = r_{spiral} \sin t \qquad z = P_{spiral} t \qquad (4-1)$$

The curvature, κ , for the helix is a function of both the pitch and radius Eq. (4-2).

$$\kappa = \frac{r_{spiral}}{r_{spiral}^2 + P_{spiral}^2} = \frac{1}{r_{curvature}} \quad (4-2)$$

The length of the helix L_{spiral} is determined by

$$L_{spiral} = L_{curvature} = n * \sqrt{(2\pi r_{spiral})^2 + P_{spiral}^2} = n * 2\pi r_{spiral} \sec \gamma \quad (4-3)$$

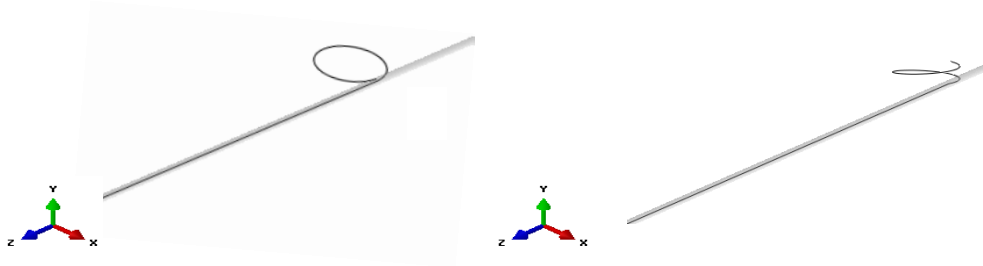
A simulation model compared the three-dimensional spiral pre-shape to the original two-dimensional circular shape. To compare the three-dimensional shape with the two-dimensional circular shape, the length of curvature $L_{curvature}$ will be the same for both models. The radius of curvature $r_{curvature}$ between the two models will also be the same. The previous two-dimensional circular shape has a small pitch equal to the diameter of the coil (0.6-mm). Table 4-14 lists the parameters for the two-dimensional circular shape modeled previously and the new three-dimensional spiral to be compared with. Figure 4-26 shows what the initial models look like. The elastic stiffness of Coil A will be used in both models for comparison.

Table 4-14 Geometry of Distal Shape

Distal Shape	$D_{Distal Shape}$ (mm)	$P_{circular}$ (mm)	$r_{curvature}$ (mm)	$L_{curvature}$ (mm)	P_{spiral} (mm)	r_{spiral} (mm)	Wrap Angle (degrees)
2D Circular	12.7	0.6	6.35	39.9	NA	NA	360
3D Spiral	NA	NA	6.35	39.9	2.54	5.08	450

Isometric View – Initial 2D Circular Shape

Isometric View – Initial 3D Spiral Shape

**Figure 4-26 Initial Distal Shape**

4.8.2 SIMULATION MODEL FOR SPIRAL EVALUATION RESULTS

The deformed geometry and radial forces were determined for the spiral distal shape and compared to the circular distal shape at discrete tube diameters of 2-, 4-, and 6-mm. The decrease in the radial size of the spiral distal shape caused it to return to its original shape in the larger 8-mm tube diameter which prevented the simulation model from giving results at this diameter. The spiral geometry should be chosen to avoid this issue. Figure 4-27 shows a plot of the deformed geometry at various tube diameters. The tube prevents the distal shape from returning to its initial three-dimensional spiral shape. The end view on the right side shows that the initial spiral shape helps it conform to the tube walls even with the smaller tube diameters.

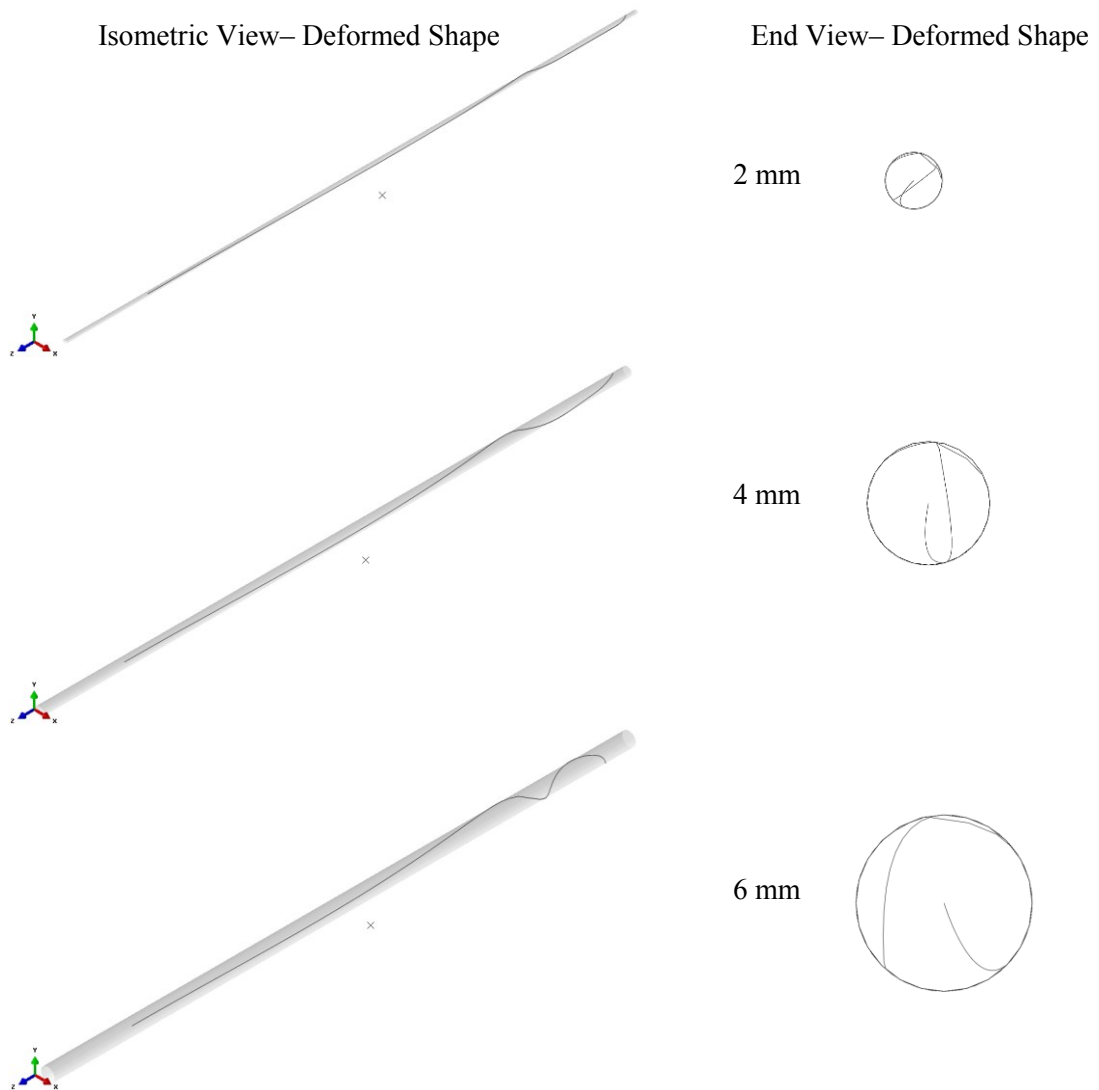


Figure 4-27 Deformed Spiral Distal Shape for Various Tube Diameters (Coil A)

The total radial force was determined for the spiral distal shape and compared to the circular distal shape. Table 4-15 lists the total radial force and the difference between a two dimensional circular shape and a three dimensional spiral shape. The results show that just

changing the distal shape to a spiral can increase the radial force from 56% to 268% depending on the tube diameter.

Table 4-15 Total Radial Force Comparison between Circular and Spiral Distal Shape

Tube Diameter (mm)	Circular Distal Shape Simulation Model (N)	Spiral Distal Shape Simulation Model (N)	Change from Circular to Spiral (%)
2	0.195	0.304	56
4	0.136	0.263	94
6	0.141	0.518	268

Figure 4-28 displays the data in Table 4-15 and shows that the spiral shape increases the radial force over a two-dimensional circular shape.

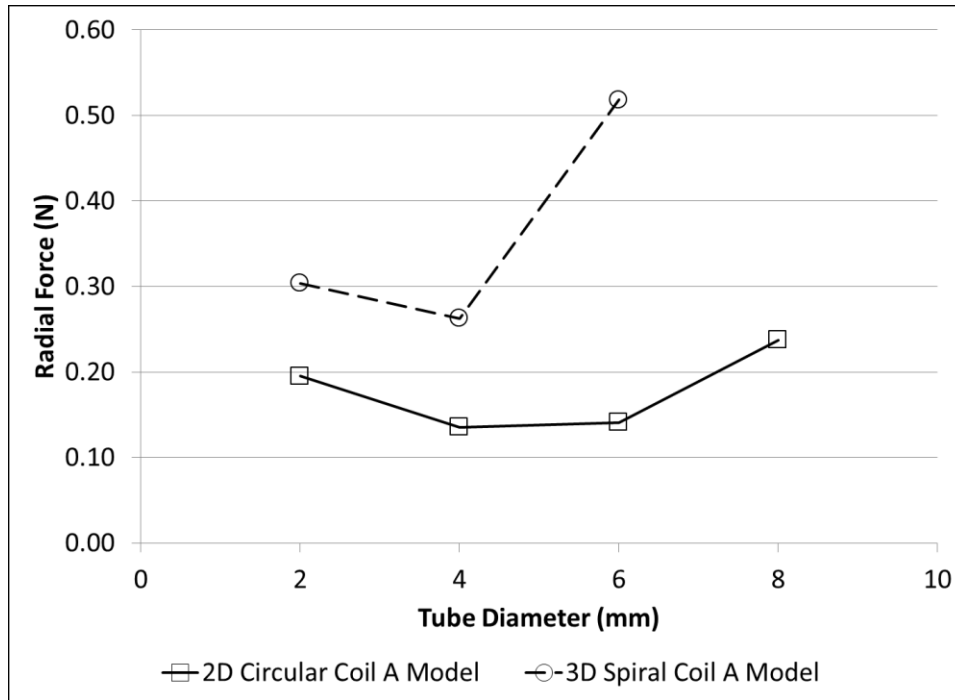


Figure 4-28 Comparison of Total Radial Force between Circular and Spiral Distal Shape

Figure 4-29 shows a plot of the radial force magnitude along the distal end of the models (z-axis) for both distal shapes. This line plot displays the radial force at each nodal location and then connects each data point with a line for visualization. The total radial force is the sum of all the radial forces along the distal end at these nodal locations. The two-dimensional circular shape contacts the tube at four discrete points. In the 6-mm tube, the three-dimensional spiral distributes contact along the tube between the 155- and 175-mm. The maximum radial force still occurs at the tip for both the 2- and 4-mm tube but at 6-mm the maximum shifts away from the distal tip. In the 6-mm tube, the distal tip of the spiral is pulled back along the z-axis and the model has a length of 183-mm instead of 190-mm for the circular shape. This shows as diameter increases the spiral can pull back within the tube as it tries to return to its original shape.

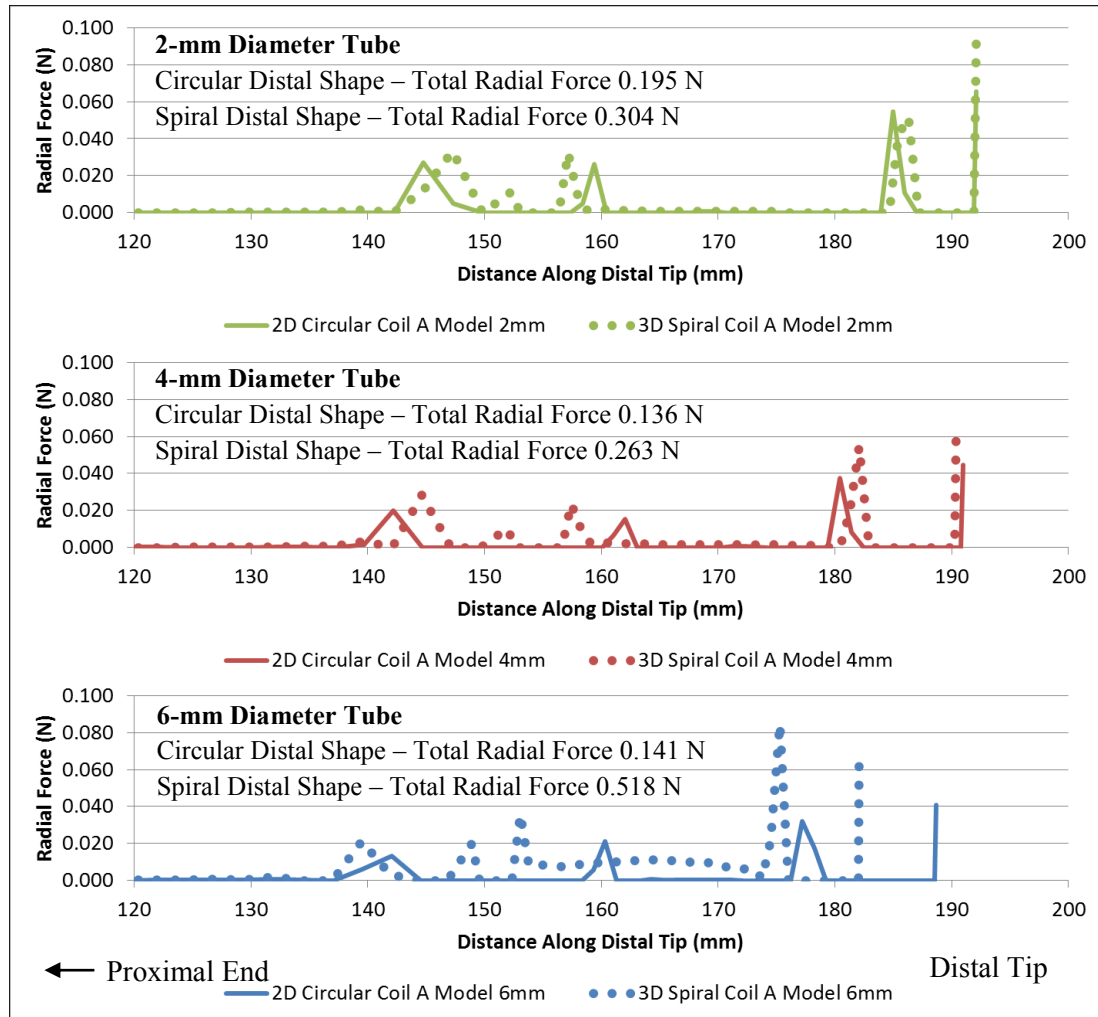


Figure 4-29 Radial Force Distribution along the Axial Direction (Coil A)

Table 4-16 lists the length of contact between the distal shape and the tube. Note that this contact length is taken along the tube axis and not along the distal shape. Therefore for the cases where the distal shape conforms to the tube, this contact length could be underestimated. The spiral shape shows a 31% to 197% increase in contact length compared with that of the circular shape. The contact length for the spiral shape shows a decrease as the tube diameter increases but this is because only the axial length is reported and not the true length along the

distal shape. The spiral shape retracts axially as it conforms to the larger diameter as illustrated in Figure 4-29 which underestimates the length of contact.

Table 4-16 Axial Tube Length of Contact Comparison between Circular and Spiral Distal Shape

Tube Diameter (mm)	Circular Distal Shape Simulation Model (mm)	Spiral Distal Shape Simulation Model (mm)	Change from Circular to Spiral (%)
2	22.1	65.7	197
4	38.3	64.1	67
6	45.3	59.3	31

4.9 SPIRAL SHAPE DOE

4.9.1 SPIRAL SHAPE DOE BACKGROUND

The spiral shape was evaluated to determine what factors influence total radial force and tip force. The goal is to have high radial forces for fixation and a low tip force to avoid the tip perforating tissue. The total radial force and tip force were evaluated using simulation models. To reduce the number of computer models, a design and analysis of experiments (DOE) methodology will be used [49, 50]. Instead of experiments, simulation models will be used to evaluate the design variables or factors.

A two-level, full factorial design for three factors (2^3 design) was used. This allowed three factors to be evaluated and each factor will have two levels (high and low). The factors to evaluate were the spiral's radius r_{spiral} , pitch P_{spiral} , and straight distal tip length $L_{distal\ tip}$. Also a constraint will be imposed that the length $L_{curvature}$ from the distal tip to the end of the curvature will be 40 mm, which is illustrated in dark gray in Figure 4-30. The experimental samples and computer model previously had a curved length of 39.9-mm (Table 4-14). A

review of the literature [51, 52] showed that within this 40-mm length is where electrodes are placed for pacing and where contact occurs with the heart.

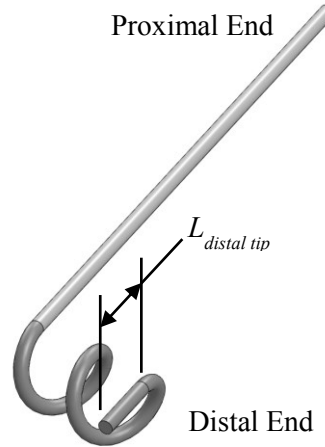


Figure 4-30 Spiral Distal Shape Representation with Distal Length

The high and low values were chosen by reviewing the spiral evaluated in Section 4.8. Table 4-17 shows the three factors with their high and low values. A center point value is also included to check the linearity assumption in the factor effects and whether there is curvature.

Table 4-17 Factors with High and Low Values

Factors	Units	Low	Center	High
r_{spiral}	(mm)	4	6	8
P_{spiral}	(mm)	2	4	6
$L_{distal\ tip}$	(mm)	1	5	9

Table 4-18 lists the parameters for the each spiral design to be evaluated. The stiffness used will be for Coil A (Table 2-3). The simulation model used a tube diameter of 4-mm that the distal shape will interact with. The 4-mm diameter was chosen since it was evaluated previously and is the middle tube diameter evaluated in Section 4.8.

Table 4-18 Spiral Designs

Spiral Design	r_{spiral} (mm)	P_{spiral} (mm)	$L_{distal\ tip}$ (mm)	$L_{curvature}$ (mm)	Wrap Angle (degrees)
1	4	2	1	40	557
2	8	2	1	40	279
3	4	6	1	40	543
4	8	6	1	40	277
5	4	2	9	40	443
6	8	2	9	40	222
7	4	6	9	40	432
8	8	6	9	40	220
9	6	4	5	40	332

4.9.2 SPIRAL SHAPE DOE RESULTS

The total radial force and the tip force were determined for all the spiral designs. Table 4-19 lists the radial forces.

Table 4-19 Spiral Design DOE Results

Spiral Design	r_{spiral} (mm)	P_{spiral} (mm)	$L_{distal\ tip}$ (mm)	Total Radial Force (N)	Radial Tip Force (N)
1	4	2	1	0.508	0.102
2	8	2	1	0.094	0.031
3	4	6	1	0.771	0.101
4	8	6	1	0.101	0.031
5	4	2	9	0.399	0.027
6	8	2	9	0.070	0.019
7	4	6	9	0.585	0.033
8	8	6	9	0.080	0.019
9	6	4	5	0.156	0.039

A cube plot (Figure 4-31) shows the same data graphically of all three variables at their high and low values with the result at each corner of the cube. The center point value is also included.

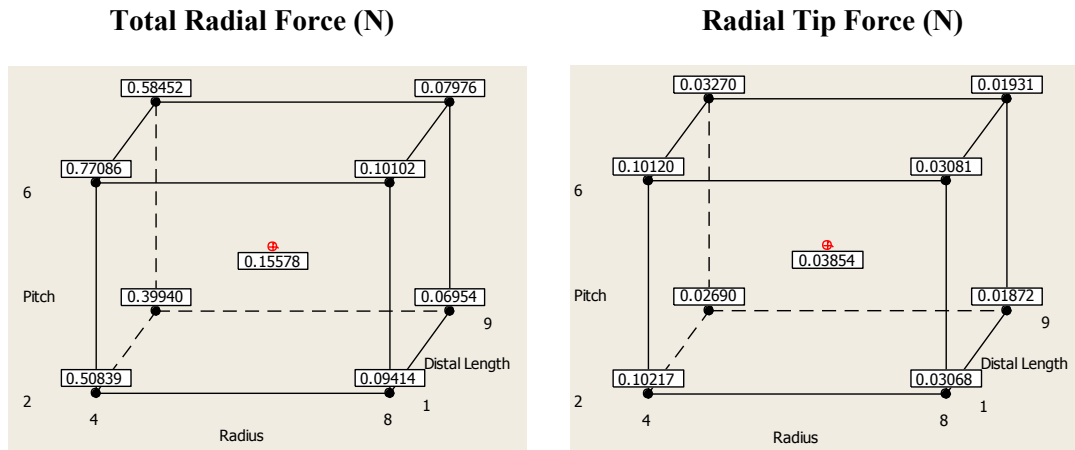


Figure 4-31 Cube Plot for DOE Results in a 4-mm Diameter Tube

The total radial force results from the cube plot (Figure 4-31) show an increase in total radial force as the spiral's radius r_{spiral} is decreased from 8- to 4-mm. This decrease in spiral radius r_{spiral} increases the stiffness of the spiral as described in Section 2.2 in Eq. (2-14). The decrease in spiral radius r_{spiral} is limited by the tube size, since if the spiral radius is smaller than the tube diameter it will pull back within the tube and return to its original shape as discussed in Section 4.8.2.

The radial tip force results from the cube plot (Figure 4-31) show a decrease in radial tip force as the spiral's distal tip length $L_{distal\ tip}$ is increased from 1- to 9-mm. The longer tip length allows the tip to conform to the tube wall and lower the force at the tip.

Analyzing the factorial design gave indications of significant factors and interactions between the factors affecting the radial force results. Simulation models were used, so there is only a

single run or replicate is at each design point [53]. This single run or replicate gave information on main effects and interactions.

4.9.2.1 Total Radial Force Factorial Analysis

The DOE factorial analysis shows a Pareto chart (Figure 4-32) of the main effects and interactions for total radial force. The spiral radius r_{spiral} is the significant factor affecting the total radial force.

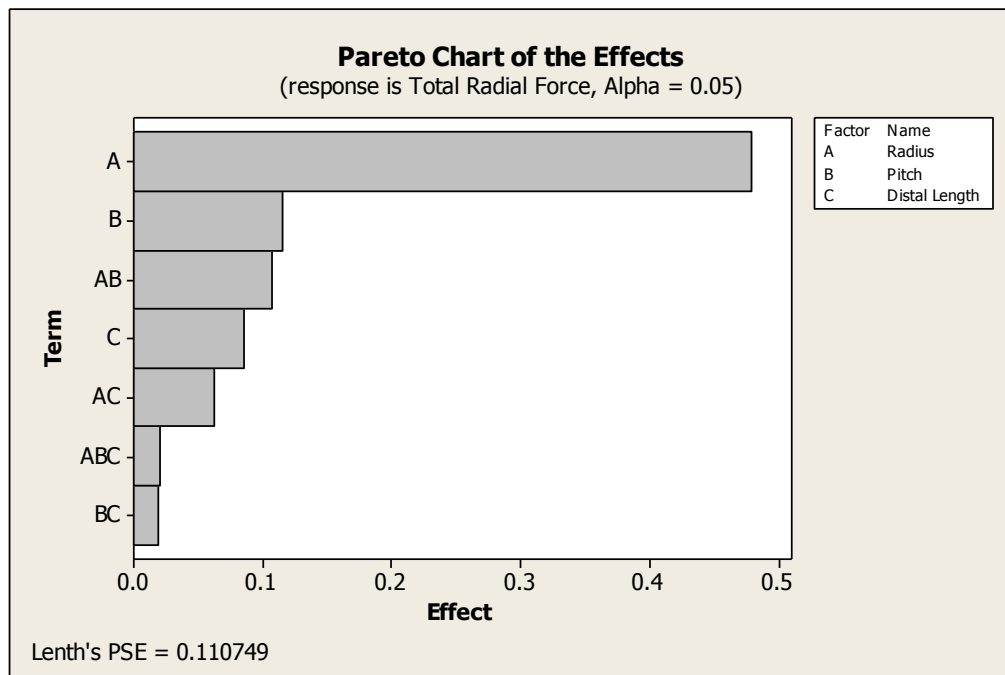


Figure 4-32 Pareto Chart of Effects for Total Radial Force

Figure 4-33 shows the main effects plot for the factors affecting the total radial force. The decrease in radius r_{spiral} from 8- to 4-mm shows the total radial force increasing from 0.1 to

0.6 N. Since the center point does not lie on the main effects line the linearity assumption in the factors is not true and curvature exists in the relationship.

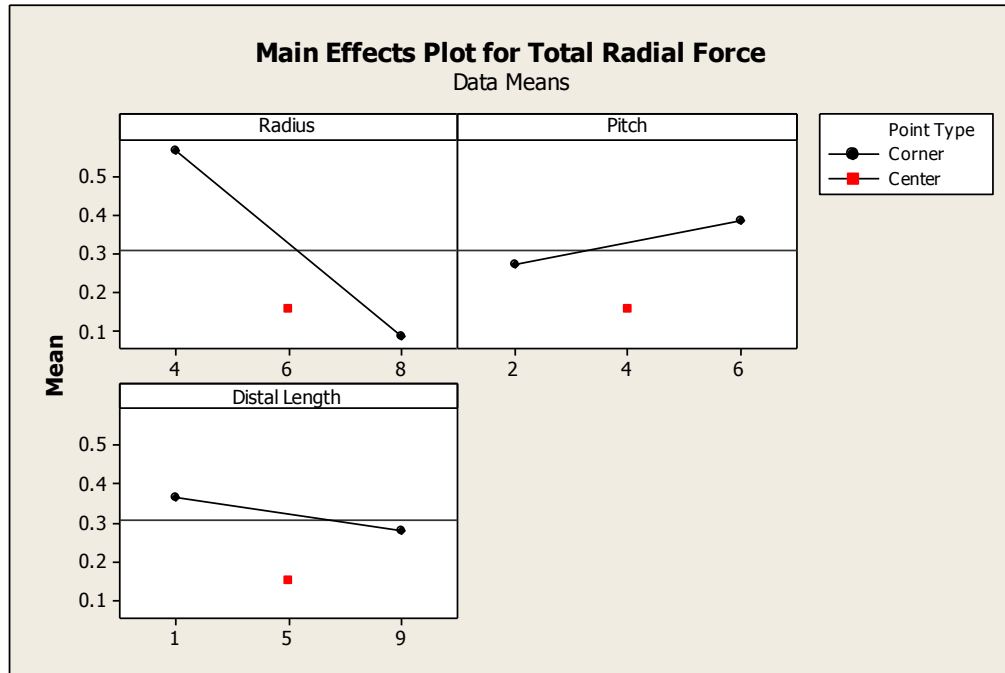


Figure 4-33 Main Effects Plot of Total Radial Force with Center Points

For interactions, parallel lines in an interaction plot indicate no interaction. The more that lines are less parallel, the higher the degree of interaction. The Pareto chart (Figure 4-32) indicated that there were not significant interactions when compare to all the factors. The interaction plot (Figure 4-34) for the total radial force shows lines that are not parallel, so there is some interaction between the radius r_{spiral} and pitch P_{spiral} . There is also some interaction between the radius r_{spiral} and distal tip length $L_{distal\ tip}$.

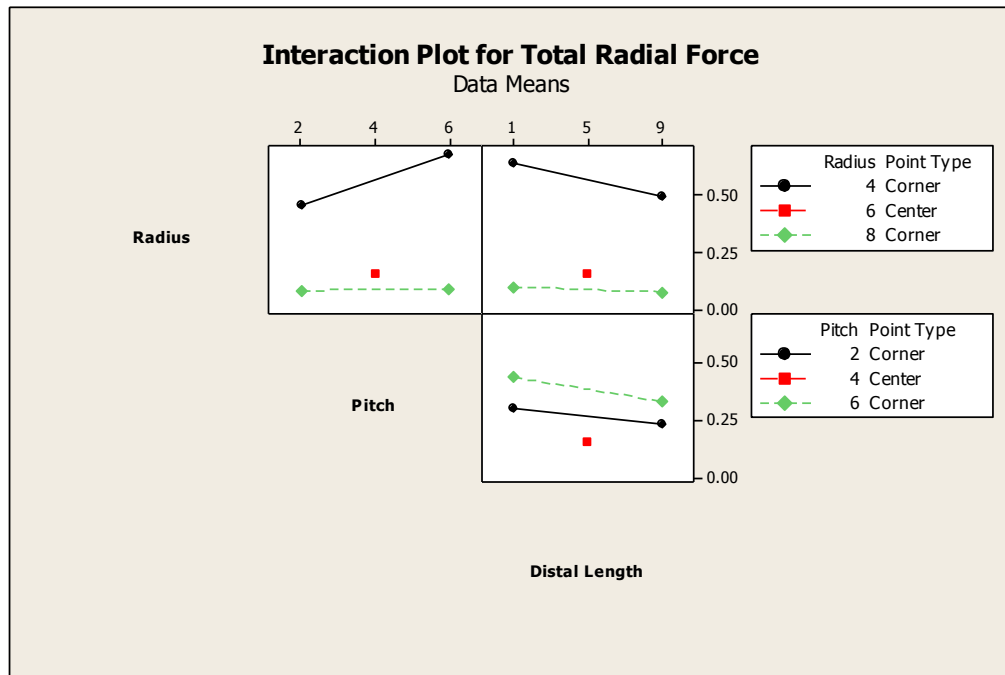


Figure 4-34 Interaction Plot of Total Radial Force with Center Points

The factorial analysis has shown that the spiral radius r_{spiral} has the most significant effect on the total radial force. The main effects plot (Figure 4-33) shows that to maximize the total radial force, the spiral radius r_{spiral} needs to be small (4-mm). The interaction plot shows some interaction between factors and indicates that for a small radius (4-mm) the pitch should be large (6-mm) and the distal length small (1-mm).

A contour plot of the results can graphically show how to maximize the total radial force also. Again the main effects show that to maximize total radial force, the radius needed to be small, so a contour plot was created with the radius held at a constant 4-mm. The lower right corner of Figure 4-35 shows the same result from the interaction graphs that the maximum total radial

force occurs when the radius is small (4-mm), pitch is large (6-mm), and the distal length is small (1-mm).

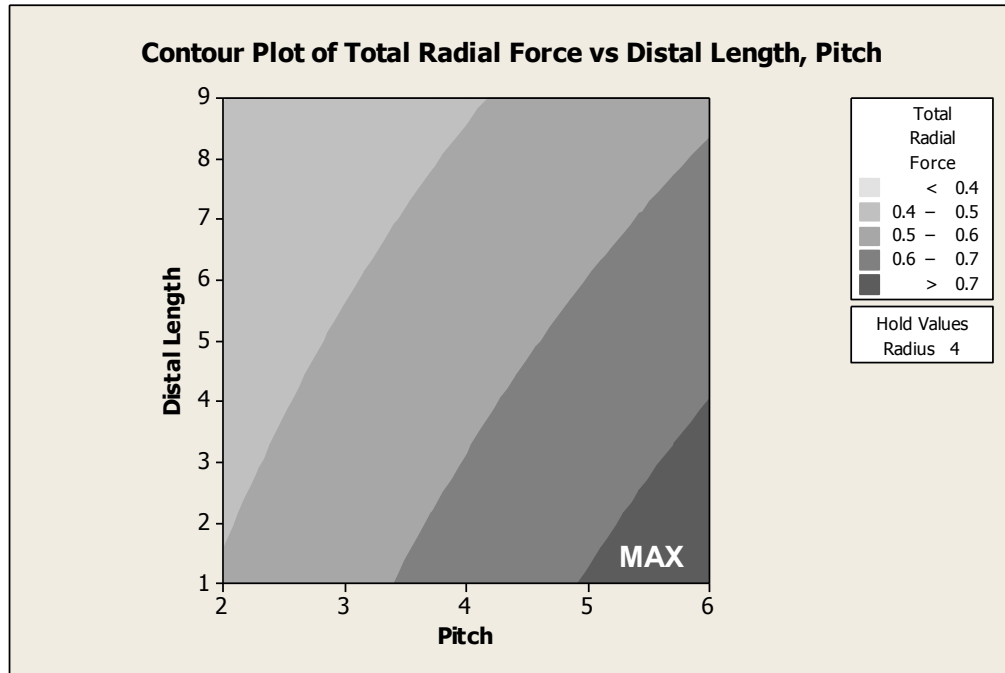


Figure 4-35 Contour Plot for Total Radial Force with Radius Held Constant at 4 mm

4.9.2.2 Radial Tip Force Factorial Analysis

The DOE factorial analysis shows a Pareto chart Figure 4-36 of the main effects and interactions for radial tip force. The spiral radius r_{spiral} and distal tip length $L_{distal\ tip}$ with their interaction are the significant factors affecting the radial tip force.

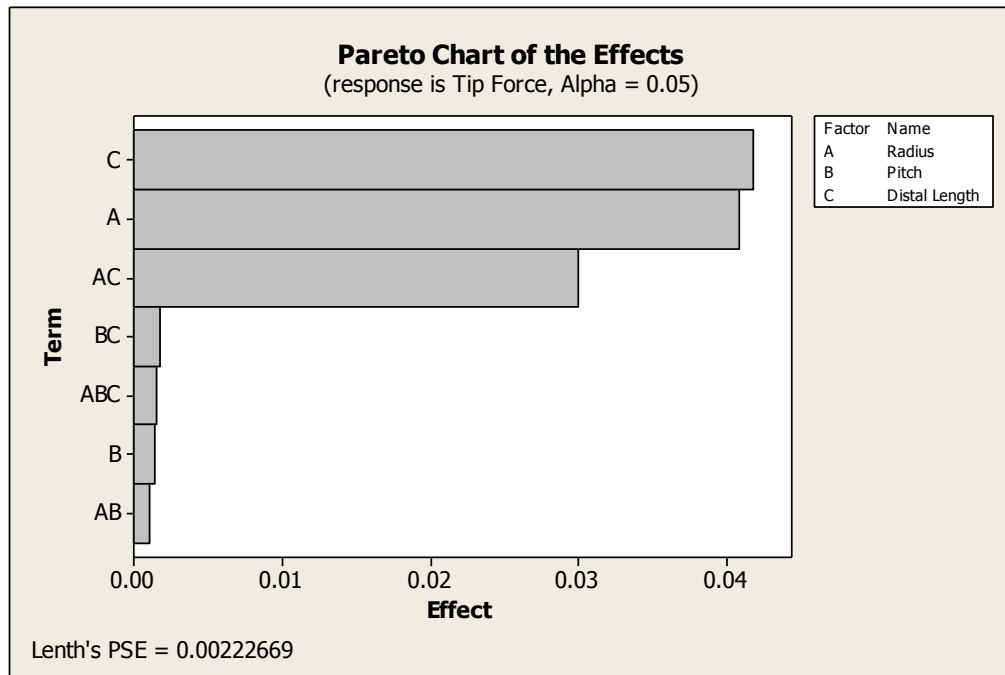


Figure 4-36 Pareto Chart of Effects for Radial Tip Force

Figure 4-37 shows the main effects plot for the factors affecting the radial tip force. The increase in radius r_{spiral} from 4- to 8-mm shows the radial tip force decreasing from 0.065 to 0.025 N. The increase in distal length $L_{distal\ tip}$ from 1- to 9-mm shows the radial tip force decreasing from 0.065 to 0.025 N. The change in pitch P_{spiral} does not change the radial tip force and stays around 0.045 N. Since the center point does not lie on the main effects line the linearity assumption in the factors is not true and curvature exists in the relationship.

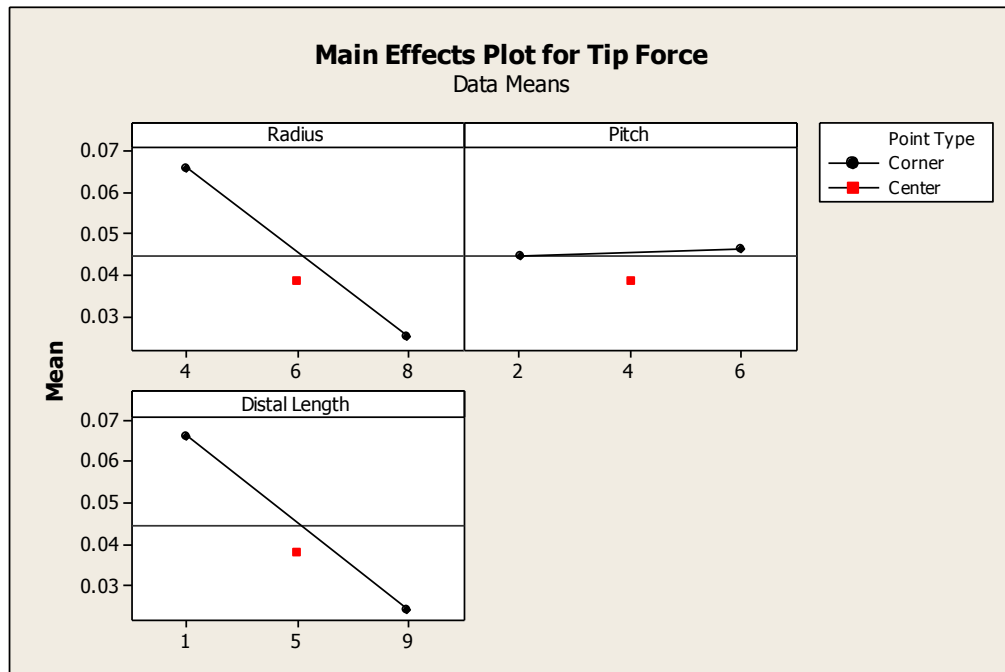


Figure 4-37 Main Effects Plot of Radial Tip Force with Center Points

For interactions, parallel lines in an interaction plot indicate no interaction. The more that lines are less parallel, the higher the degree of interaction. The Pareto chart (Figure 4-36) indicated that there were was a significant interaction between radius r_{spiral} and distal tip length $L_{distal\ tip}$. The interaction plot (Figure 4-38) for the radial tip force shows an interaction effect between the radius r_{spiral} and distal tip length $L_{distal\ tip}$ since the lines are not parallel. The other interaction plots are parallel which indicates very little interaction.

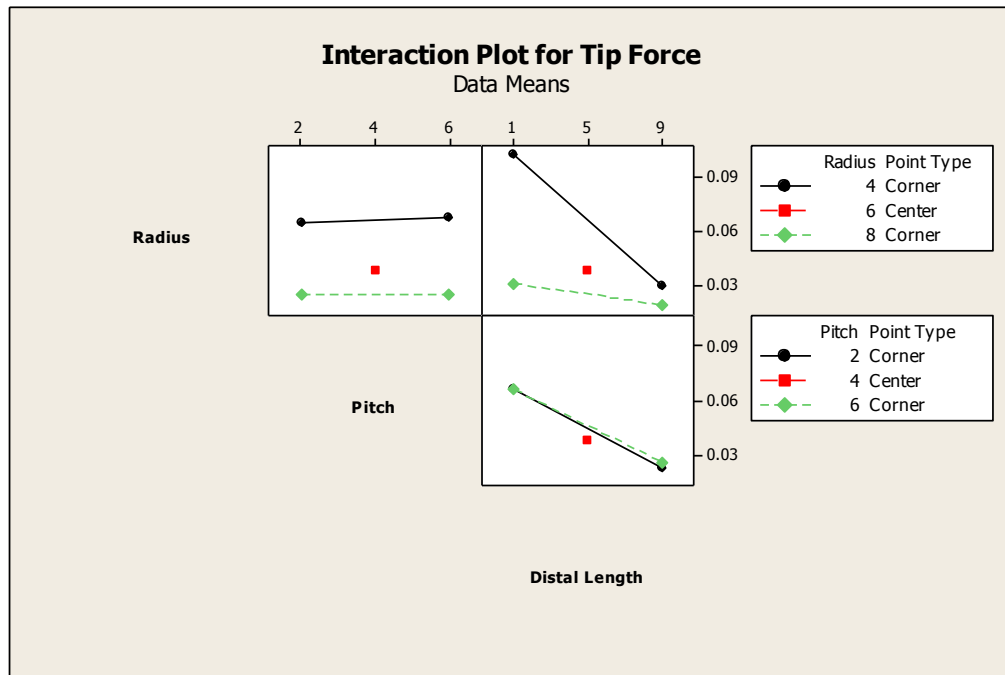


Figure 4-38 Interaction Plot of Radial Tip Force with Center Points

The factorial analysis has shown that the spiral radius and the distal tip length with their interaction have the most significant effect on the total radial tip force. The main effects plot (Figure 4-37) show that to minimize the radial tip force the spiral radius r_{spiral} needs to be large (8-mm) and the distal length $L_{distal\ tip}$ needs to be large (9-mm). The interaction plot shows interaction effect between the radius r_{spiral} and distal tip length $L_{distal\ tip}$. To minimize the radial tip force, a large radius (8-mm) and distal length (9-mm) should be used.

A contour plot of the results can graphically show how to maximize the radial tip force also. Both the main effects (Figure 4-37) and interaction (Figure 4-38) plots show that pitch does not affect the radial tip force significantly, so a contour plot was created with the pitch held constant at the center point 4-mm. The upper right corner of Figure 4-39 shows the same

result from the interaction graphs that the minimum radial force occurs when the radius is large (8-mm) and the distal length (9-mm) is large for any pitch.

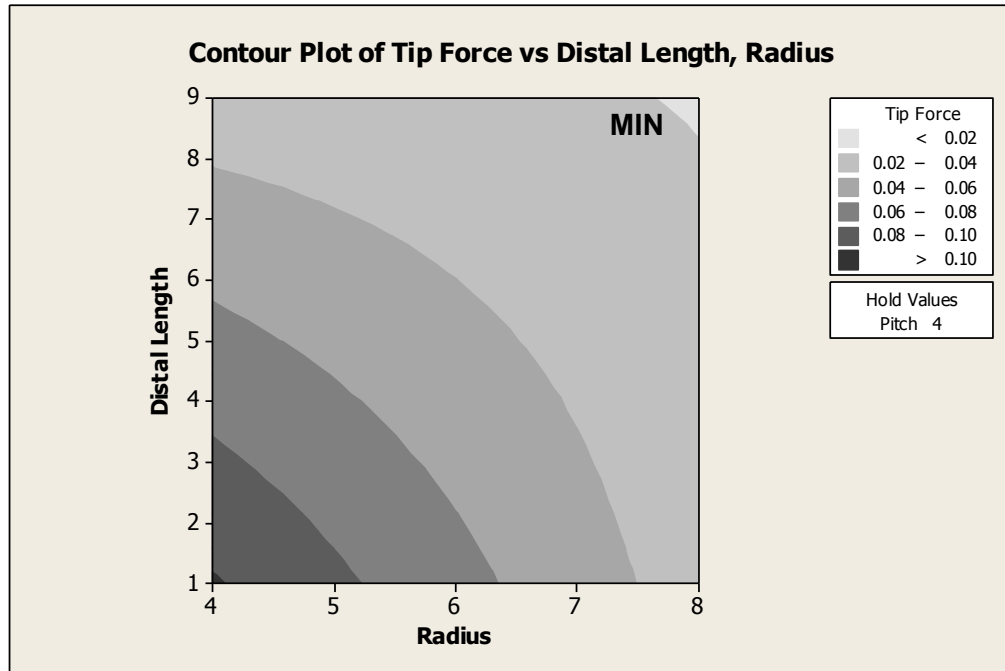


Figure 4-39 Contour Plot for Radial Tip Force with Pitch Held Constant at 4-mm

4.9.2.3 Optimal Spiral Shape for Total Radial Force and Tip Force

The previous sections have identified the factors and their values to maximize the total radial force and minimize the radial tip force but these factors conflict with each other (Table 4-20).

The maximum total radial force occurs when the radius is small (4-mm), pitch is large (6-mm), and the distal length is small (1-mm). The minimum radial force occurs when the radius is large (8-mm) and the distal length (9-mm) is large for any pitch.

Table 4-20 Spiral Designs for Maximum Total Radial Force & Minimum Tip Force

Spiral Design	r_{spiral} (mm)	P_{spiral} (mm)	$L_{distal\ tip}$ (mm)	Total Radial Force (N)	Radial Tip Force (N)
Maximum Total Radial Force Spiral Design	4	6	1	0.771	0.101
Minimum Tip Force Spiral Design	8	2	9	0.070	0.019
Minimum Tip Force Spiral Design	8	6	9	0.080	0.019

The DOE factorial analysis for the two goals or responses can be combined and optimized. This optimization is only local or within the range that the factors were evaluated. When two goals or responses are being optimized, the importance of the response compared to the other needs to be considered. The primary goal was chosen to maximize radial force for fixation, with the secondary goal to minimize radial tip force. With the primary goal of maximizing total radial force, the spiral should have a small radius r_{spiral} . Pitch P_{spiral} does not affect the tip force significantly (Figure 4-37) but does increase total radial force when the pitch is large so the pitch should be large. The distal length does significantly affect the tip force (Figure 4-37) but it affects the total radial force to a lesser extent (Figure 4-33) so the distal length $L_{distal\ tip}$ should be large.

The optimal design to maximize total radial force and minimize the tip force is when the radius is small (4-mm), pitch is large (6-mm), and the distal length is large (9-mm) for the range of variables examined in this DOE (Table 4-21). This is only a local optimum within the range of variables evaluated.

Table 4-21 Locally Optimized Three-Dimensional Spiral

Spiral Design	r_{spiral} (mm)	P_{spiral} (mm)	$L_{distal\ tip}$ (mm)	Total Radial Force (N)	Radial Tip Force (N)
Locally Optimized Spiral	4	6	9	0.585	0.033

Table 4-22 lists the length of contact between the distal shape and the tube for the optimized spiral. Note that this contact length is taken along the tube axis and not along the distal shape. Therefore for the spiral distal shape that conforms to the tube, this contact length could be underestimated.

Table 4-22 Axial Tube Length of Contact for Locally Optimized Three-Dimensional Spiral

Tube Diameter (mm)	Locally Optimized Spiral (mm)
4	59.9

4.10 SUMMARY

Numerical simulation was used to determine the force between the distal shape and tube wall. Experimental validation of the computer model was shown. Various distal shape design variables were then evaluated to maximize the total radial force and minimize the radial tip force. Figure 4-40 shows the progression of how the distal shape changed from a two-dimensional circular shape to a three-dimensional spiral.

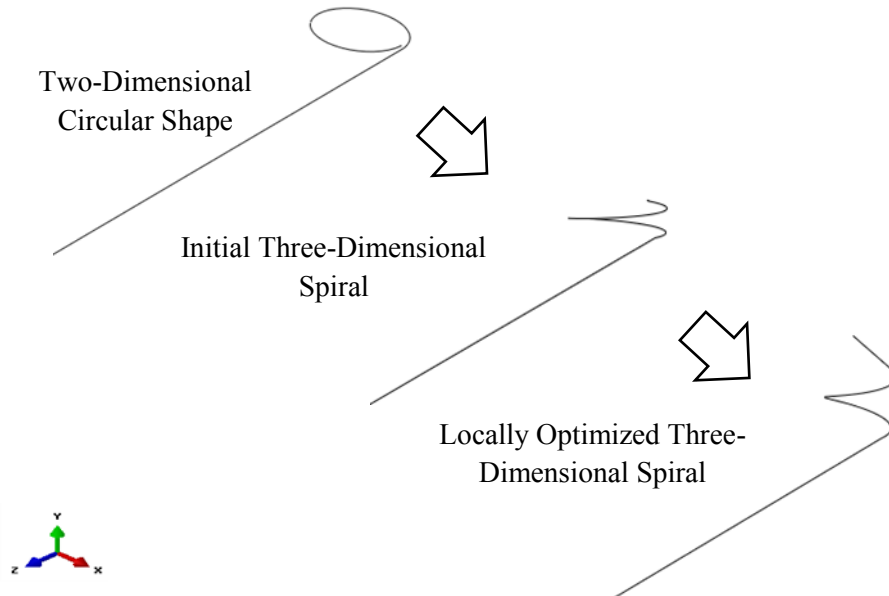


Figure 4-40 Progression of Distal Shape to Maximize Total Radial Force and Minimize Tip Force

The total radial force and radial tip force were determined for various distal shapes (Section 4.7 through 4.9). Figure 4-41 shows a plot of the radial force magnitude along the distal end of the model (z-axis) for the three distal shapes. This line plot displays the radial force at each nodal location and then connects each data point with a line for visualization. The total radial force is the sum of all the radial forces along the distal end at these nodal locations. The local optimized three-dimensional spiral at the bottom of the figure shows that the maximum radial force has been shifted away from the tip. This spiral shape also contacts the tube at multiple points from 155- to 185-mm. Also included in the figures is a line for the 90th percentile force which shows that approximately 90% of the total force lies below this value.

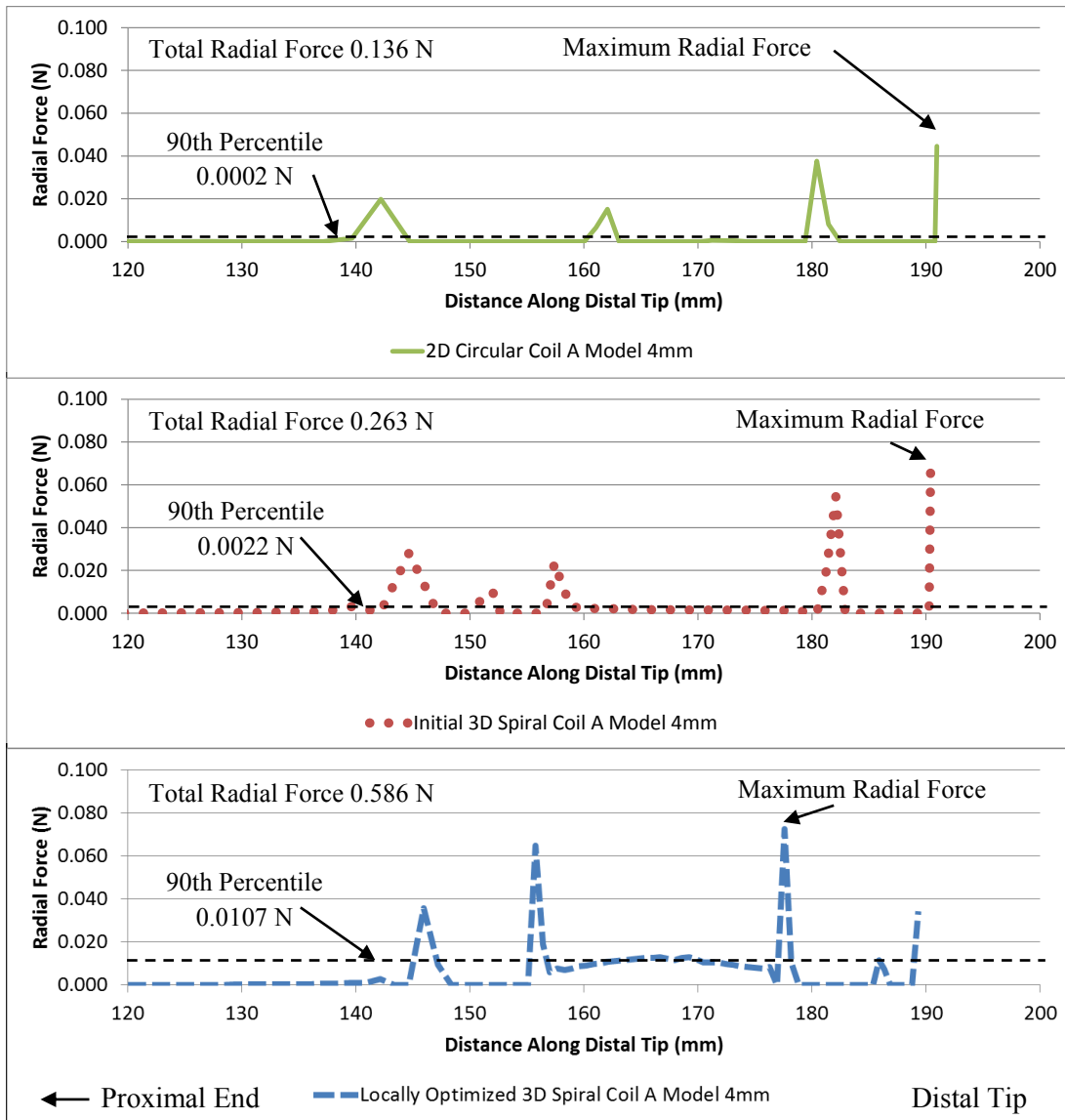


Figure 4-41 Radial Force Distribution along the Axial Direction for Distal Shapes

Table 4-23 describes the distal shapes with the radial forces, and Figure 4-42 displays this data. The local optimized three-dimensional spiral has improved on the initial two-dimensional circular design. The total radial force has been increased by over 430% and the radial tip force has decreased by 26%.

Table 4-23 Distal Shapes and Radial Forces (4-mm Tube)

Distal Tip Shape	$r_{\text{spiral or circle}}$ (mm)	P_{spiral} (mm)	$L_{\text{distal tip}}$ (mm)	$L_{\text{curvature}}$ (mm)	Total Radial Force (N)	Radial Tip Force (N)
2D Circular	6.35	0.6	1	39.9	0.136	0.045
Initial 3D Spiral	5.1	2.54	1	39.9	0.263	0.066
Locally Optimized Spiral	4	6	9	40	0.586	0.033

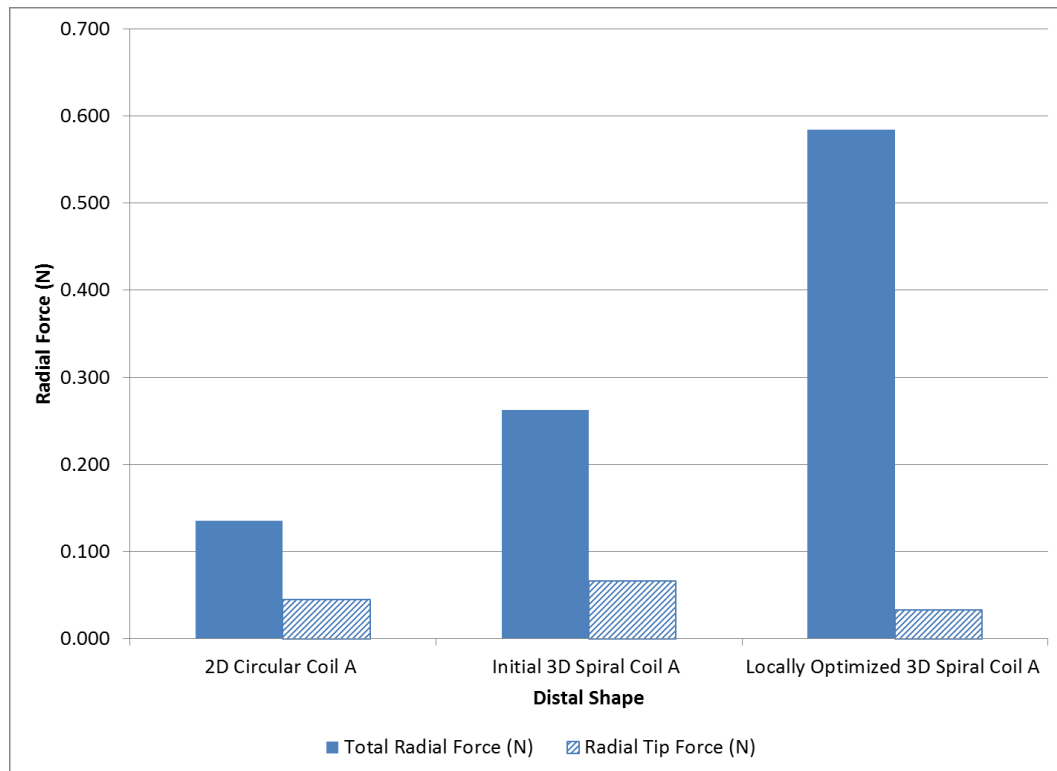


Figure 4-42 Comparison of Radial Forces between Distal Designs

Table 4-24 lists the length of contact between the distal shape and the tube. Note that this contact length is in the axial tube length and not along the distal shape so for cases where the

distal shape conforms with the tube this contact length could be underestimated. The locally optimized spiral retracts axially as it conforms to the tube as illustrated in Figure 4-41.

Table 4-24 Axial Tube Length of Contact Comparison between Distal Shapes (4-mm Tube)

Distal Tip Shape	Axial Tube Length of Contact (mm)
2D Circular	38.3
Initial 3D Spiral	64.1
Locally Optimized Spiral	59.9

Table 4-25 list the length of contact between the distal shape and the tube but includes the 90th and 80th percentile force with their corresponding length of contact. For example, the locally optimized spiral has a maximum force of 0.0724 N and the length of contact is 59.9-mm for any contact force. The 90th percentile force is lower at 0.0107 N and the length of contact for any force greater than 0.0107 N is 16.2-mm. The 80th percentile force is at 0.0075 N and the length of contact for any force greater than 0.0075 N is 29.0-mm. The spiral shapes have a more distributed contact force along the distal shape for a greater length of contact compared to the circular distal shape.

Table 4-25 Axial Tube Length of Contact with Percentile for Distal Shapes

Distal Tip Shape	100 th Percentile Force (N)	Length of Contact (mm)	90 th Percentile Force (N)	Length of Contact (mm)	80 th Percentile Force (N)	Length of Contact (mm)
2D Circular	0.0446	38.3	0.0002	18.0	0.0000	38.2
Initial 3D Spiral	0.0664	64.1	0.0022	20.6	0.0015	31.3
Locally Optimized Spiral	0.0724	59.9	0.0107	16.2	0.0075	29.0

A potential next step to determine a global optimum, which is not presented here, is to use this locally optimized design point as a new starting point to perform another DOE to evaluate these factors and responses again.

CHAPTER 5

NUMERICAL SIMULATION MODEL OF CURVED BLOOD VESSELS

5.1 INTRODUCTION

Numerical simulation will be used to determine the force between the distal shape of the lead and the wall of a curved cardiac vein. The previous numerical simulation (Chapter 4) determined the distribution of radial force along the distal shape when inserted into a straight tube. The straight tube model was then compared with the total radial force obtained by *in-vitro* experiments (Chapter 3) that used a straight tube radial force tester. The following models implemented by numerical simulation will be used to investigate the distal lead shape as it is inserted into curved tube.

5.2 CURVED TUBE BACKGROUND

The distal lead is inserted into cardiac veins that wrap around the outside of the left ventricle. The curvature of the heart is assumed to be circular and the diameters of curvature are estimated to be between 6- and 9-cm. These curvatures are based on the average adult heart size having a 12-cm length from base to apex, 9-cm at its broadest transverse diameter, and a 6-cm anteroposteriorly thickness [54, 55]. The veins into which the lead is inserted run in the transverse direction, so curvature diameters of 6- and 9-cm were selected.

To evaluate the curvature effect, a simulation model of the distal shape interacting with a 4-mm tube was chosen. The 4-mm diameter was chosen since it was evaluated previously and is the intermediate tube diameter evaluated in Section 4.8. The stiffness used will be for Coil A (Table 2-3). Friction will also be assumed to be zero (frictionless). The proximal end will be prevented from moving by setting all degrees of freedom (DOF) to zero. For a straight tube, the orientation of the initial distal shape about its lead axis does not affect how the distal shape deforms in the straight tube. With a curved tube, the orientation of the initial distal shape about its lead axis could affect how the distal shape deforms in the tube. The lead orientation of the initial shape about its lead axis will be evaluated to determine its effect on radial forces.

The radial forces for the two-dimensional circular distal shape (Section 4.7) and the three-dimensional locally optimized spiral distal shape (Section 4.9) will be obtained by means of numerical simulation. The geometry for the distal shape will be the same as the previous models. Table 5-1 lists a summary of the geometry for the considered distal shapes.

Table 5-1 Distal Shapes

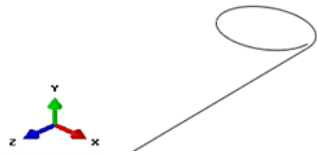
Distal Tip Shape	$r_{\text{spiral or circle}}$ (mm)	P_{spiral} (mm)	$L_{\text{distal tip}}$ (mm)	$L_{\text{curvature}}$ (mm)
Two-Dimensional Circular	6.35	0.6	1	39.9
Three-Dimensional Locally Optimized 3D Spiral	4	6	9	40

The radial forces corresponding to the distal shapes will be compared with each other. The radial forces that are obtained for the 6- and 9-cm diameter curved tubes will then be compared to the results of the straight tube (Section 4.7 and 4.9).

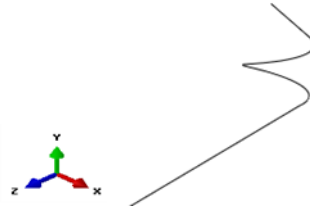
5.3 CURVED TUBE RESULTS

The deformed geometry and radial forces were determined for the two-dimensional circular distal shape and the three-dimensional locally optimized spiral distal shape within a 4-mm diameter tube that had curvature diameters of 6- and 9-cm. The upper part of Figure 5-1 shows the initial distal shapes before insertion into a curved tube, while the lower portion of the figure displays the deformed distal shapes in the tube with a 6-cm diameter curvature. On the left side of Figure 5-1, the tip of the two-dimensional circular distal shape is pushing directly down into the tube. Figure 5-2 shows deformed distal shapes in the tube with a 9-cm diameter curvature. For each respective distal shape, their deformed shape within the curved tubes is similar.

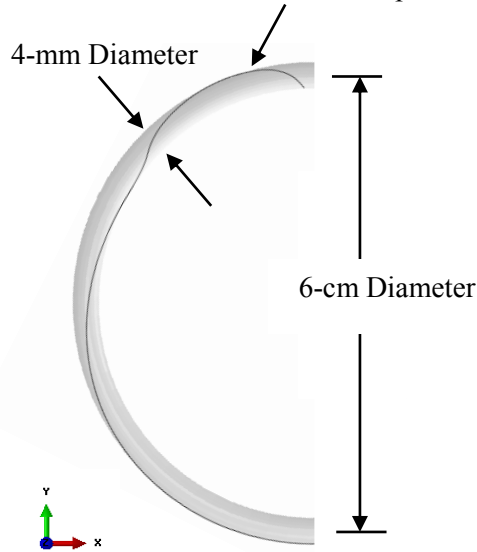
Initial Two-Dimensional
Circular Distal Shape



Initial Three-Dimensional Locally
Optimized Spiral Distal Shape



Deformed Two-Dimensional
Circular Distal Shape



Deformed Three-Dimensional
Spiral Distal Shape

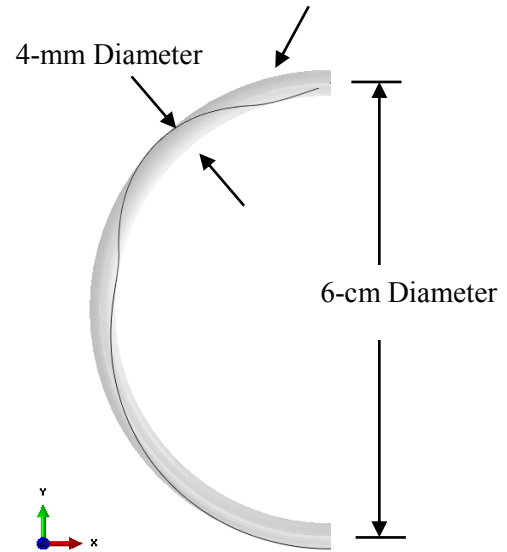


Figure 5-1 Deformed Distal Shapes Inside 4-mm Diameter Tube with a 6-cm Diameter Curvature

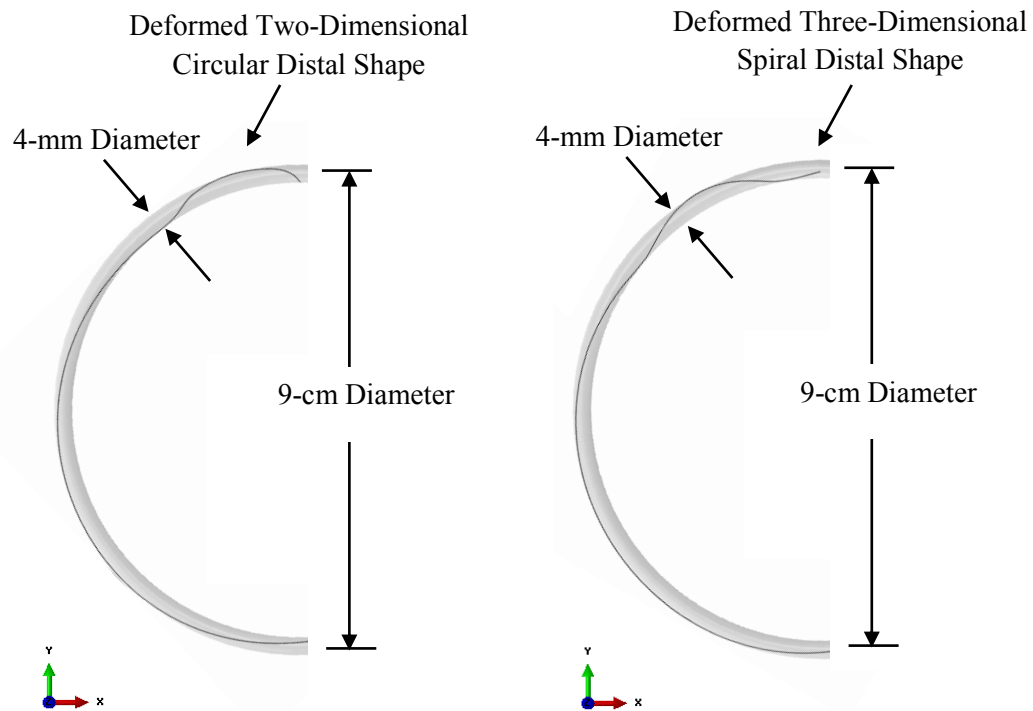


Figure 5-2 Deformed Distal Shapes Inside 4-mm Diameter Tube with a 9-cm Diameter Curvature

The orientation of the initial distal shape with respect to the curved tube was varied and it was determined that the distal shape would always twist to the same deformed shape. The axial torsional stiffness of the distal shape is not high enough to resist the orientation of the final deformed distal shape. The radial forces were not impacted by orientation of the initial distal shape to the curved tube as well.

Table 5-2 lists the total radial force and radial tip force for the two-dimensional circular distal shape that has been inserted into a 4-mm diameter tube. The straight tube simulation results (Section 4.7) are also listed and then the simulations with tube curvature are added. The total

and radial tip forces are greater for the tube with-curvature case relative to those for the straight tube. Figure 5-3 displays the data in Table 5-2 and shows that both the total and radial tip forces decreased when the tube curvature diameter was decreased from 9- to 6-cm.

Table 5-2 Circular Distal Shape Radial Forces within Straight and Curved Tubes

Tube Curvature Diameter (cm)	Total Radial Force (N)	Radial Tip Force (N)
Straight	0.136	0.045
9	0.278	0.084
6	0.254	0.077

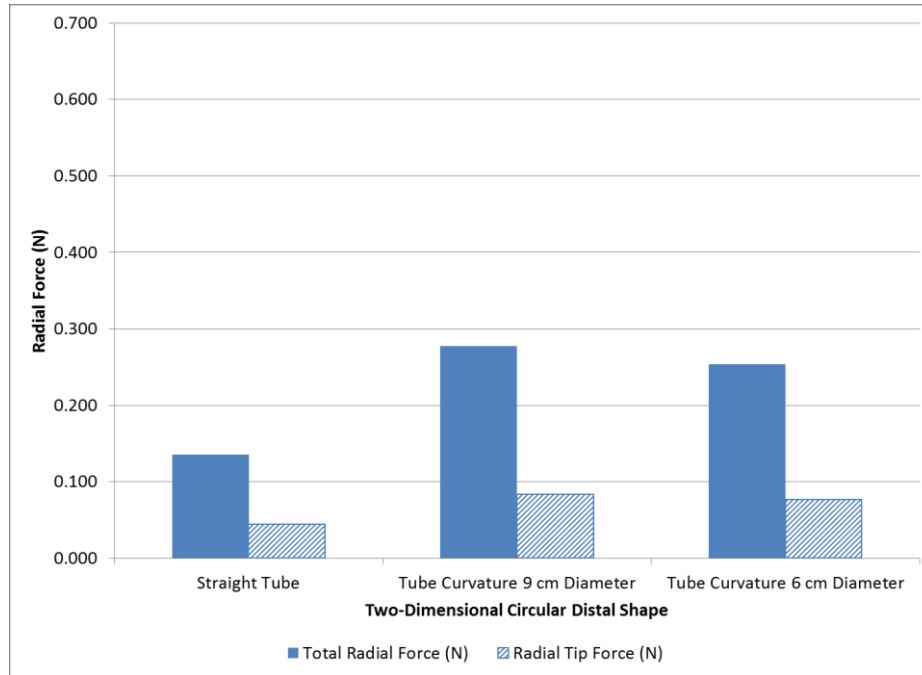


Figure 5-3 Comparison of Circular Distal Shape Radial Forces For Curved and Straight Tubes

Figure 5-4 shows a plot of the radial force magnitude along the distal end of the model (z-axis) for the two-dimensional circular distal shape when it is inserted into a straight 4-mm tube, a curved 4-mm tube with a curvature diameter of 9-cm, and a curved 4-mm tube with a

curvature diameter of 6-cm. This line plot displays the radial force at each nodal location and then connects each data point with a line for visualization. The total radial force is the sum of all the radial forces along the distal end at these nodal locations. The length of the deformed circular distal shape is shorter within the curved tube (180-mm) than within the straight tube (193-mm) as shown by the distal tip force location in Figure 5-4. The curved tube allows the two-dimensional circular distal shape to retract into the tube and thereby allows the distal shape to conform to the tube walls in a three-dimensional shape. The conforming of a distal shape against the tube walls with a three-dimensional shape has been shown to increase radial force (Section 4.7.2) which explains the higher radial force for a two-dimensional circular distal shape when inserted into a curved tube.

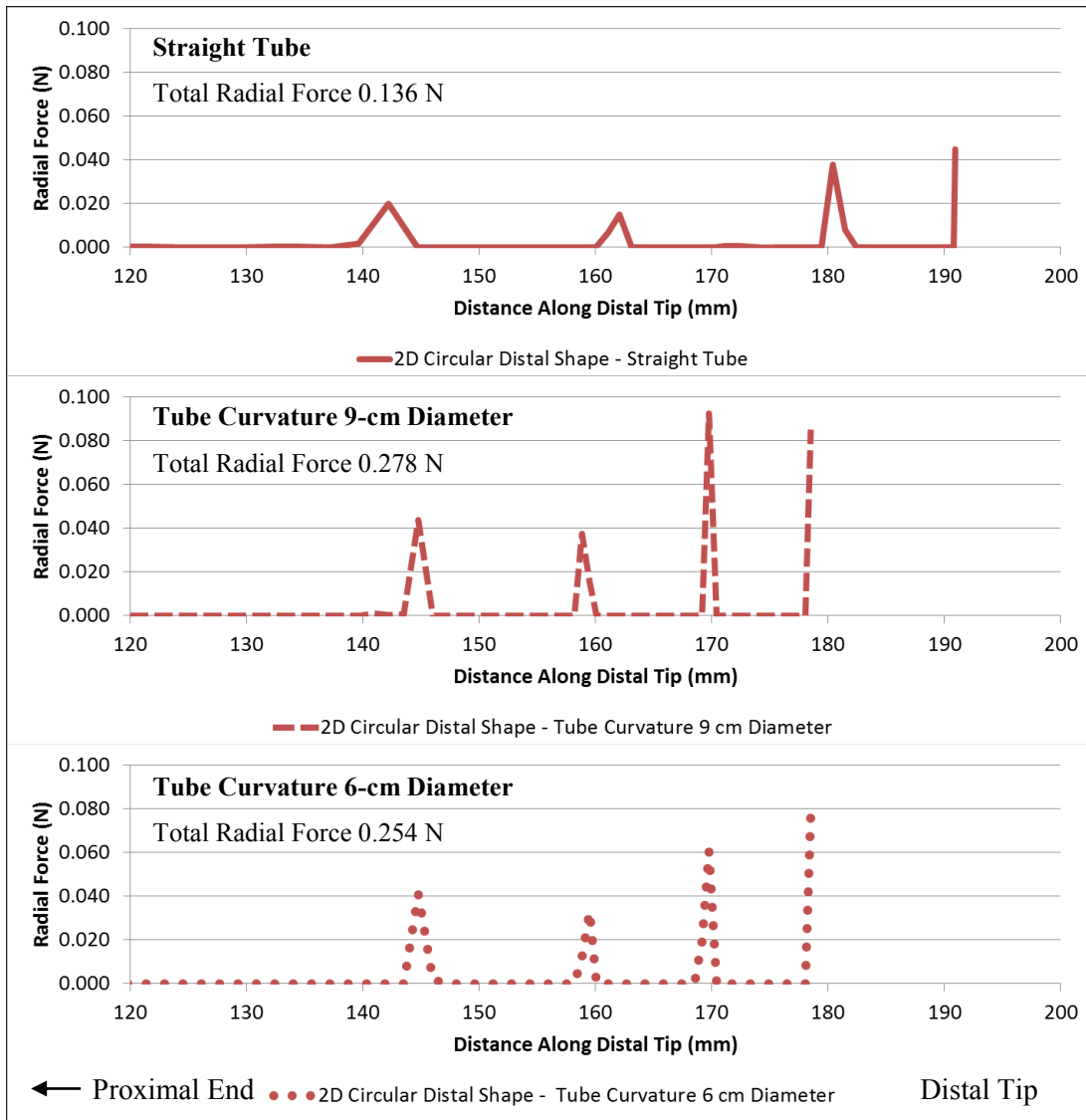


Figure 5-4 Radial Force Distribution along the Axial Direction for a Circular Distal Shape (4-mm Tube)

Table 5-3 lists the total radial force and radial tip force for the three-dimensional locally optimized spiral distal shape that has been inserted into a 4-mm diameter tube. The straight tube simulation results (Section 4.9) are listed and then the simulation results with tube curvature are included. The total and maximum radial forces are larger for the straight model

and then decrease with curvature. Figure 5-5 displays the data in Table 5-3 and shows that both the total and radial tip forces decrease when the tube curvature diameter was decreased from 9- to 6-cm.

Table 5-3 Locally Optimized Spiral Shape within Straight and Curved Tubes

Tube Curvature Diameter (cm)	Total Radial Force (N)	Radial Tip Force (N)
Straight	0.585	0.033
9	0.325	0.030
6	0.269	0.025

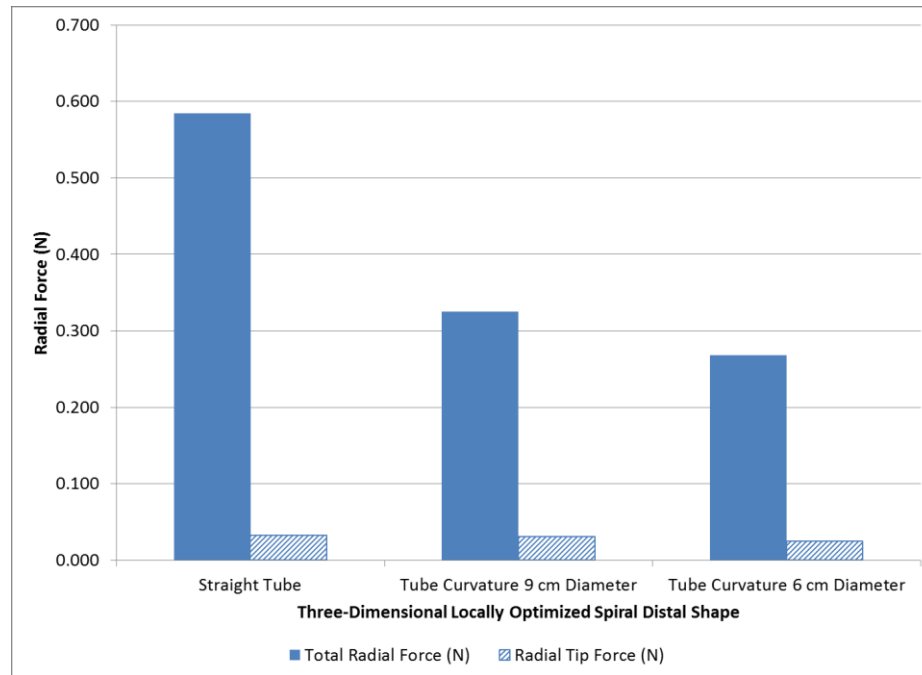


Figure 5-5 Comparison of Spiral Distal Shape Radial Forces for Curved and Straight Tubes

Figure 5-6 shows a plot of the radial force magnitude along the distal end of the model (z-axis) for the three-dimensional locally optimized spiral distal shape when it is inserted into a straight 4-mm tube, a curved 4-mm tube with a curvature diameter of 9-cm, and a curved

4-mm tube with a curvature diameter of 6-cm. This line plot displays the radial force at each nodal location and then connects each data point with a line for visualization. The total radial force is the sum of all the radial forces along the distal end at these nodal locations. The length of the deformed spiral distal shape increased slightly within the curved tube (193-mm) compared with the straight tube (190-mm) as shown by the distal tip force location in Figure 5-6. This slight increase in length indicates that the spiral distal shape is not conforming as well to the curved tube as it does to the straight tube which could explain why the radial forces decrease when tube curvature is added.

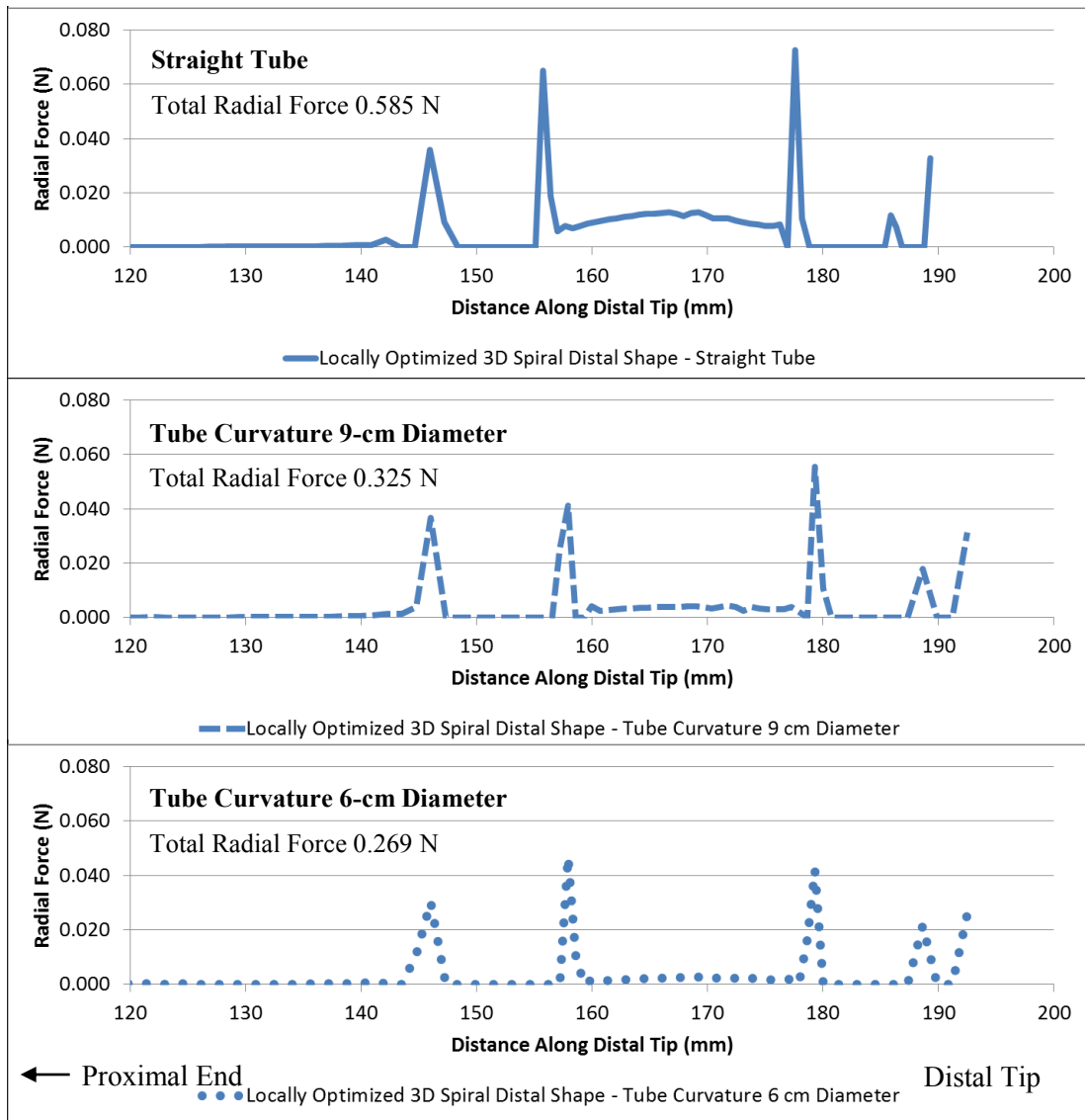


Figure 5-6 Radial Force Distribution along the Axial Direction for a Spiral Distal Shape (4-mm Tube)

5.4 SUMMARY

The involvement of curved geometry into which the distal shape is inserted adds complexity to determining the optimal distal shape to maximize the total radial force and minimize the

radial tip force. For a given distal shape, radial forces can increase or decrease when a distal shape is inserted into a curved tube versus a straight tube. The use conditions or geometry under which the distal shape will be inserted are important for distal shape optimization. The three-dimensional spiral distal shape model still had a higher total radial force and a lower radial tip force than did the two-dimensional circular shape model (Figure 5-3 and Figure 5-5). The three-dimensional spiral distal shape examined here was optimized for a straight tube (Section 4.9). The results based on the curved tube models suggest that optimization of the spiral shape should be based upon the curved tube models instead of the straight tube models. This updated optimization of the distal shape using curved tube models is out of the present scope.

CHAPTER 6

ANALYTICAL APPROXIMATION FOR FIXATION FORCE

6.1 INTRODUCTION

Using a spiral or helix shape for the distal end of a lead to fixate or push against the inside of a tube is analogous to a spring clutch that uses a helical coil wrapped around a shaft. The distal shapes examined previously are spirals that have a diameter larger than that of the tube into which they are inserted. After the spiral has been straightened out and inserted into the smaller diameter tube, the tube walls create a radial force pressing against the distal shape by preventing the spiral from returning to its original diameter. A spiral clutch is similar but instead the spiral has a diameter smaller than that of the shaft over which it is assembled. The outer cylinder walls create a radial force against the spiral clutch by preventing it from returning to its original diameter. This analogy will allow an analytical derivation of the radial force a spiral exerts inside a tube.

An analytical derivation using strain energy and Castigliano's theorem will be used to calculate the radial force or pressure for a two-dimensional circular shape pushing against the inside of a tube. This analytical model allows a simple calculation of the radial force that may be useful as a quick design tool. The results of this analytical model will be compared to a simulation model to check for accuracy.

The derivation of the radial force for a spring clutch is commonly found in machine design textbooks [56]. In this reference, Burr derives the equation to calculate the force as a spring diameter is increased to fit over a larger diameter shaft. The following derivation is a generalization to calculate the radial force as the spring diameter is decreased to fit within a smaller diameter tube. The derivation assumes that the spring maintains its circular two-dimensional shape with a very small axial pitch and end effects are neglected.

6.2 ANALYTICAL DERIVATION

Strain energy and Castigliano's theorem provides a means to calculate the radial force as illustrated by Burr [56]. Figure 6-1 shows the axial view of the coil with the original unconstrained dimensions identified with a subscript of zero. Burr's derivation is modified and the coil is assumed to have a circular cross section as shown in Section A – A of Figure 6-1. The diameter d of the circular cross section will be assumed to be much smaller than the coil radius r_0 , so this diameter d is assumed to be unity in this derivation. The coil material is assumed to be linear elastic material.

The wire length L of the arc is bounded by the angle θ_0 . Burr's derivation is modified to have the coil compressed radially and the wire length L stays the same but is bounded by a larger angle θ . A pressure P and an internal moment M develop when the coil is compressed radially from the original radius r_0 to the final radius r . The pressure P is force per linear length.

Another assumption is that the coil maintains a two-dimensional shape and does not expand axially. Small displacements and frictionless conditions are assumed.

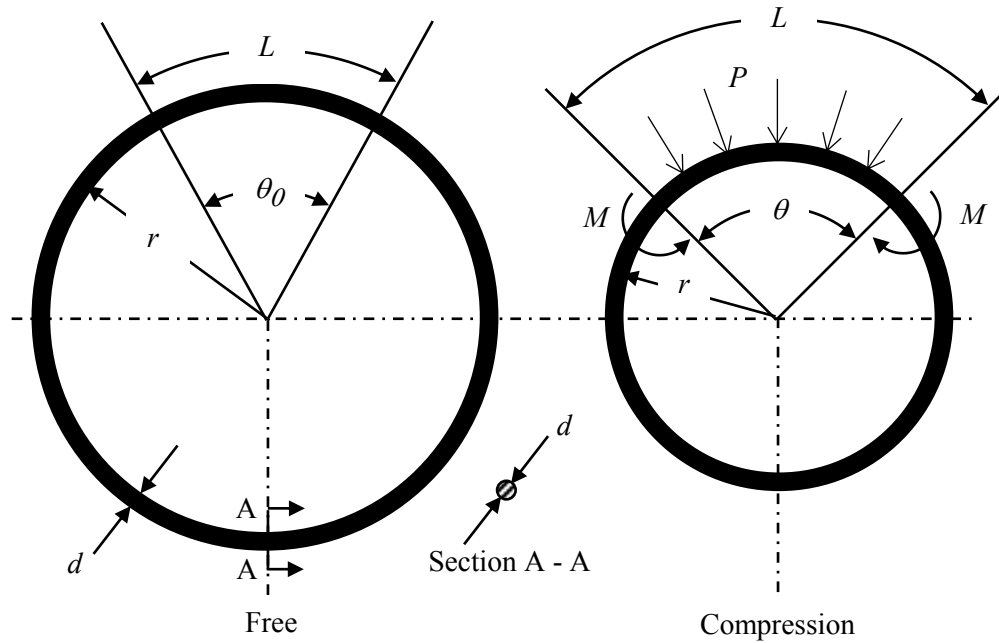


Figure 6-1 Axial View of Coil Before and After Radially Compression

When a curved beam changes curvature, the moment M is defined as the change in curvature times the bending stiffness EI as given by

$$M = EI \left(\frac{1}{r} - \frac{1}{r_0} \right) \quad (6-1)$$

where E is the modulus of elasticity and I is the moment of inertia of the wire.

If the bending moment is constant, the total strain energy U from bending [34] is

$$U = \frac{M^2 L}{2 E I} \quad (6-2)$$

The strain energy as a function of curvature is obtained when the moment M from Eq (6-1) is substituted into Eq (6-2) with the result

$$U = \frac{E I L}{2} \left(\frac{1}{r} - \frac{1}{r_0} \right)^2 \quad (6-3)$$

A pressure P compresses the coil radially and performs work in the same direction r . Burr [56] illustrates that this work dU is equal to the pressure P acting over the length L through a small displacement dr so that

$$dU = P L dr \quad (6-4)$$

The derivative of the strain energy Eq (6-3) can be taken with respect to the radius r with the outcome

$$\frac{dU}{dr} = \frac{E I L (r_0 - r)}{r_0 r^3} \quad (6-5)$$

Substituting the equation for work Eq (6-4) into the foregoing derivative and rearranging gives the pressure P per linear length as a function of the change in coil radius r .

$$P = \frac{E I (r_0 - r)}{r_0 r^3} \quad (6-6)$$

This derivation is a simplified version of Burr's pressure calculation for spring clutch [56] but for a spring compressed within a tube instead.

6.3 COMPARISON OF ANALYTICAL AND SIMULATION MODEL

The accuracy of the foregoing analytical model was compared with a simulation model. For this comparison, the previous geometry and stiffness of Coil A for a two-dimensional circular shape (Section 4.2) was used in both the analytical and simulation models. Coil A had a modulus of elasticity E of 363 MPa (Table 2-3), and the initial diameter of the two-dimensional circular shape was 12.7-mm (Figure 4-3).

A new simulation model is used to calculate the radial pressure in a two-dimensional circular coil with an initial diameter of 12.7-mm (6.35-mm radius) that is compressed radially to a given radii r of 5-, 4-, and 3-mm. The loading condition for this simulation model is different from the previous models (Section 4.3) since this model is not straightened out before insertion into a tube. Also this simulation model does not include the end effects that occur as shown in the previous models. These assumptions are the same ones used in the analytical model and were chosen to provide a fairer comparison with the analytical model.

Table 6-1 lists the radial pressures calculated from Eq (6-6) and obtained from the simulation models. Figure 6-2 displays the data in Table 6-1 and shows how the radial pressure increases as the coil is radially compressed.

Table 6-1 Comparison of Radial Forces from the Analytical and Simulation Models

Coil A Elastic Modulus	Initial Diameter	Initial Radius	Final Radius	Radial Force per Linear Length	Radial Force per Linear Length	Difference between Analytical and Simulation Models
E_{beam} (MPa)	D_0 (mm)	r_0 (mm)	r (mm)	Analytical Model Chapter 6 $P_{analytical}$ (N/mm)	Simulation Model Chapter 6 $P_{computer}$ (N/mm)	(%)
363	12.7	6.35	5.0	0.00493	0.00497	0.8
363	12.7	6.35	4.0	0.01676	0.01698	1.3
363	12.7	6.35	3.0	0.05664	0.05793	2.2

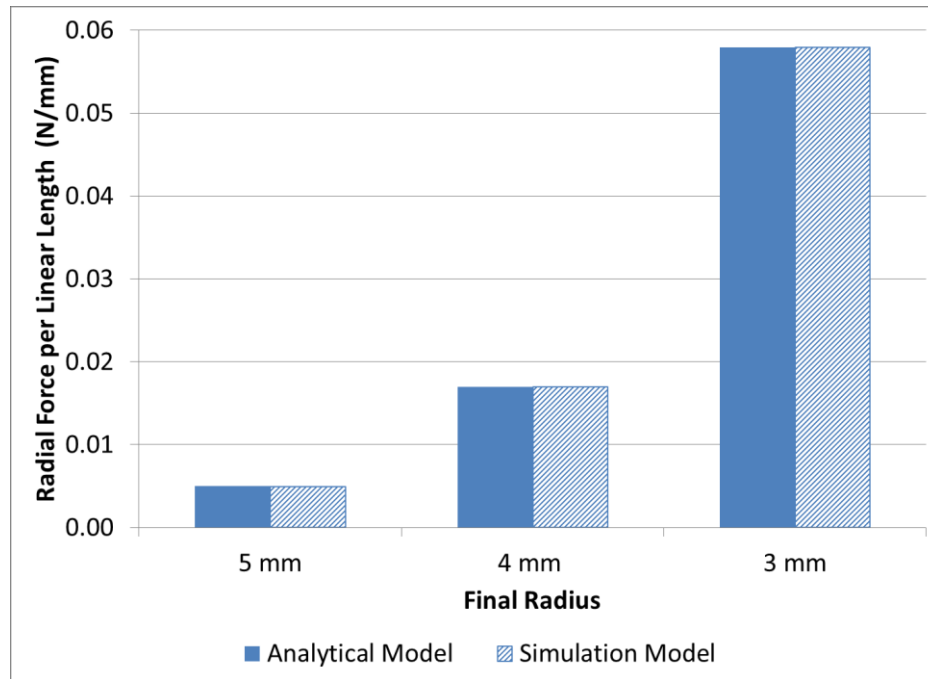


Figure 6-2 Comparison of Radial Force between Analytical and Simulation Model

When the coil is radially compressed from a radius of 6.35- to 5-mm, the analytical and simulation model results deviated by 0.8%. As the radial compression is increased, the deviation was found to increase. A 2.2% deviation occurs when the coil is compressed from a radius of 6.35- to 3-mm. This deviation can be attributed to the discretization inherent in the simulation model. In particular, simulation model discretizes the curvature with small elements of a straight length. As the coil compresses to a smaller radius, smaller elements are needed. The models used here had an element size that was held constant for all three models which led to the deviation increasing as curvature was increased. This deviation would decrease if more elements were used to accurately model the curvature.

Both the analytical and simulation models presented in this Chapter 6 neglect end effects and assume the two-dimensional shape of the coil does not elongate axially. These assumptions are different from the two-dimensional circular model in Chapter 4 where the distal shape had a given length (40-mm) with end effects and axial elongation within the tube.

6.4 COMPARISON OF MODELS

Table 6-2 compares the results of the total radial force from the previous models in Chapter 4 with the analytical model used in the current chapter. The total radial force for the analytical model is obtained by multiplying the radial pressure per linear length by the length of curvature (40-mm) for the model in Chapter 4. Table 6-2 compares the total radial force when the two-dimensional circular shape interacts with 8- and 6-mm tubes.

Table 6-2 Comparison of Total Radial Force between Chapter 6 and Chapter 4 Models

Tube Diameter	Total Radial Force	Total Radial Force	Difference between Analytical and Simulation Models
(mm)	Analytical Model Chapter 6 (N)	Simulation Model Chapter 4 (N)	(%)
8.0	0.67	0.237	183
6.0	2.27	0.141	1510

The radial forces deviate between the different models. In Chapter 4, the two-dimensional circular distal shape was straightened out and inserted into a tube. That model had a given finite length and allowed end effects. The analytical and simulation models in this chapter assume that the two-dimensional circular shape stays circular and planar as it compresses to a smaller radius or diameter, but this may be an unrealistic assumption for large radial compression. These are significant differences in the loading conditions and these models should not be compared with each other. For lead fixation, where the distal shape of the lead is straightened and inserted the simulation model presented in Chapter 4 is appropriate.

The analytical model of this chapter does provide a very simple and quick way to determine the radial force for a coil compressed in a tube, but it must be used with the appropriate loading conditions. In a case where the two-dimensional shape of the coil is maintained and does not elongate axially, this analytical model would be appropriate. The technique of using strain energy and Castigliano's theorem is another tool that can provide structural understanding on the fixation of leads within a cardiac vein but it must be applied appropriately.

CHAPTER 7

CONCLUDING REMARKS

7.1 INTRODUCTION

This thesis has focused on how various engineering tools, experimentation, numerical simulation, optimization and mathematical analysis, can be applied to improve the fixation of a left-ventricle lead within a cardiac vein by maximizing the radial fixation force and minimizing the tip force. Left-ventricle cardiac leads for implantable pacemakers can lose their fixation within a cardiac vein and dislodge. Dislodgement requires the patient to return to the hospital for a surgical lead revision that involves repositioning of the lead within the cardiac vein.

A common lead-fixation mechanism for left-ventricle leads is a two- or three-dimensional shape at the distal end. Since the lead and the distal end are constructed from a metal coil, this two- or three-dimensional distal shape can be pre-formed into the coil. During implantation inside the cardiac vein, the distal end is straightened by inserting a guidewire or stylet through the coil. Once the lead distal end is positioned within the cardiac vein, the wire is removed and the distal shape pushes against the vein as it tries to return to its original shape.

7.2 ANALYTICAL BEAM APPROXIMATION OF A COIL

In Chapter 2, the elastic coil stiffnesses were derived analytically so different coil samples could be experimented on to investigate whether coil stiffness is directly related to radial force. Deriving the bending, torsional, and axial elastic stiffness of a coil allowed simulation models using three-dimensional beam elements to be created. Beam elements with these elastic stiffnesses are line elements used to create a one-dimensional idealization of a three-dimensional structure or distal shape. This simplification removed the necessity of creating models that had the geometry of the actual coils. Beam elements with their equivalent stiffnesses were used in the models instead.

The elastic stiffnesses of the coil can be controlled by the geometry and material properties. They are functions of the pitch angle γ , the number of filars in the coil N , filar modulus of elasticity E_{filar} , filar shear modulus G_{filar} , filar moment of inertia I_{filar} , and filar polar moment of inertia J_{filar} .

7.3 EXPERIMENTATION

A series of experiments presented in Chapter 3 used a radial force tester that measured the total radial force that a distal shape exerts on a straight cylindrical tube. The radial force tester used a mechanical iris that contracts and expands radially around the distal lead shape. The mechanism of the mechanical iris limited the experiments to only straight tubes.

Coil stiffness was varied in the experiment and found to directly correlate to radial force. The samples used in the experiment consisted of a coil covered with silicone tubing with the distal

end having a two-dimensional circular shape. When this circular distal shape was deformed within the radial force tester the radial forces were obtained. Three different coil stiffnesses were experimented with and the total radial force was found to increase with increasing stiffness.

The radial force tester has some limitations but allows radial forces to be measured directly. One limitation is that it can only allow distal shapes to be measured in a straight tube. Also the mechanical iris contains numerous mechanical parts that slide against each other during contraction and expansion which result in different radial forces being measured depending upon whether the tester was contracting or expanding. An average radial force between the contraction and expansion values was used to compensate for this. The numerous mechanical parts within the radial force tester also generate noise in the measurement but this was reduced by using a moving average on the data.

7.4 NUMERICAL SIMULATION

Simulation models allowed various distal shapes to be quickly evaluated for their total radial force as well as the distribution of these radial forces along the distal shape. The simulation models in Chapter 4 were created to simulate the previous experiments. The models evaluated the radial forces for a two-dimensional circular distal shape.

Initial simulations of the simulation models evaluated the assumptions used in the model. The first assumption was that the element size used to discretize the model was appropriate. Various element sizes were evaluated (Section 4.4) to determine the maximum element size

where the radial force results would not change significantly (less than 5%). An element size of 5.0-mm or less met this criterion and was used for all subsequent simulation models.

The effect of friction on the radial forces within the simulation model was determined for the two-dimensional circular distal shape (Section 4.5). It was found that friction reduces the radial forces around the distal shape. Friction adds shear forces between the distal shape and tube wall that cause the distal shape to axially stretch. Radial forces are generated by bending and torsion loads where the distal lead contacts the tube walls. The axial stretching caused by friction reduces the amount of bending and torsion within the distal shape and also reduces the radial force. Determining friction coefficients can be highly error prone, especially within a cardiac vein. Most lead designs try to achieve low friction that allows for easy sliding within a vein and to avoid abrasion. For subsequent models, the interface between the distal shape and the tube was assumed frictionless.

Another assumption in the simulation model was that the proximal end length was long enough that it does not influence the radial forces at the distal tip. Various proximal end lengths were evaluated (Section 4.6) to determine the minimum length for which the radial force results would not change significantly (less than 5%). A proximal length of 150-mm or greater met this criterion and was used for all subsequent simulation models.

7.5 NUMERICAL SIMULATION VALIDATION WITH EXPERIMENTS

The simulation model with a two-dimensional circular distal shape determined the deformed geometry and radial forces for all three coil designs at discrete straight tube diameters of 2-,

4-, 6-, and 8-mm (Section 4.7). The model simulated the experiment that was presented in Chapter 3. The simulation model also provided a distribution of the radial force along the distal shape, which experimentation could not provide. The simulation model gave the radial force at the distal tip which is useful information since high tip forces could cause perforation within a cardiac vein. The simulation models determined that the radial forces decreased as the tube diameter was increased from 2- to 6-mm which agreed with the experiment. The simulation model determined that radial forces increased as the tube diameter was increased from 6- to 8-mm which deviated from the experiment only at these larger tube diameters. This deviation was examined to determine the cause.

The frictionless simulation model of the distal shape deviated from the experiments at larger tube diameters. The simulation model of the two-dimensional circular distal shape was reevaluated with friction. When friction was included into the simulation model the radial forces results were very similar to those of the experiment (Chapter 3). The friction in the experiment could be significant since the samples were coils inside silicone tubing that moved against the metal iris of the radial force tester. The actual friction between the distal lead shape and a cardiac vein will be different from this *in-vitro* experiment.

7.6 NUMERICAL SIMULATION OF A SPIRAL DISTAL SHAPE

The simulation models indicated that as a deformed two-dimensional circular conformed more to the tube higher radial forces occurred which is desirable. A three-dimensional spiral distal shape was chosen since it would conform more against the walls within a tube. A three-dimensional spiral distal shape was evaluated against the original two-dimensional circular

shape to determine if the total radial force could be increased (Section 4.8). The three-dimensional spiral distal shape was shown to have significantly higher radial forces (56% to 268%) when compared with the two-dimensional circular distal shape.

The three-dimensional spiral distal shape was then optimized using numerical simulation to maximize the total radial force for fixation and minimize the radial tip force to avoid perforation. A design of experiment (DOE) methodology was used with numerical simulation to optimize the distal shape geometry (Section 4.9). The simulation models used a straight tube. The locally optimized three-dimensional spiral distal shape had a total radial force that was 330 % higher than the original two-dimensional circular distal shape and the radial tip force was reduced by almost 29%.

Since actual cardiac veins are curved, a curved tube was evaluated with numerical simulation to determine how the distal shapes would perform in Chapter 5. The radial force distributions within a distal shape were similar whether the tube was straight or curved, but the total and radial tip force were different depending upon the distal tip shape. For the two-dimensional circular distal shape, the total and radial tip force increased from the straight tube results when curvature is added. For the three-dimensional spiral distal shape the opposite occurred and the total and radial tip force decreased from the straight tube results when curvature is added.

Tube curvature added complexity to the distal shape evaluation to determine the optimal distal shape to maximize total radial force and minimize radial tip force. The three-dimensional spiral distal shape still had a higher total radial force and a lower radial tip force when compared to the two-dimensional circular distal shape in the curved tube simulation model.

The results of the curved tube models show that the radial force that the distal shape exerts on

the tube wall is dependent on both the distal tip shape and the shape of the tube into which it is inserted.

7.7 MATHEMATICAL ANALYSIS

A mathematical analysis using engineering principles was presented in Chapter 6 to derive the radial force that a distal shape exerts against a tube after insertion. This analytical approach using strain energy and Castigliano's theorem allows fundamental engineering principles to be applied to understand how a coil's material and geometry affect the radial force. This relationship between the coil and radial force was inferred from the previous simulation models in Chapter 4 but the mathematical analysis clearly shows how the bending stiffness and radius affect the radial force.

Assumptions and idealizations used in the mathematical model lead to deviations between it and the simulation model used in Chapter 4. To mathematically derive the radial force simplifying assumptions were made that the coil compress radially and does not expand axially. This assumption that the coil stays within a two-dimensional circular shape does not simulate the actual use condition of the cardiac lead being straightened as it is inserted. The simulation model in Chapter 4 simulates this use condition which matches the experiment in Chapter 3. The mathematical analysis does provide a fundamental understanding and can provide a radial force if used in the appropriate case.

7.8 CONCLUSION

The methodology shown in this thesis demonstrates how experimentation and numerical simulation can be used synergistically to optimize the lead distal shape to maximize the total radial force for fixation and minimize the radial tip force. Experiments were limited by the radial force tester to straight tubes. Simulation models were created to simulate the same experiments. The experiments and correlating simulation models provided validation and confidence that numerical simulation could provide results beyond what was tested. The simulation models were then updated to evaluate and optimize the distal lead shape for radial force. Finally, since the cardiac veins into which the distal lead shape is inserted are curved, the models were updated again to evaluate the distal lead shape inserted into a curved tube.

Bibliography

- [1] J. Cleland, J.-C. Daubert, E. Erdmann, N. Freemantle, D. Gras, L. Kappenberger and L. Tavazzi, "Longer-term effects of cardiac resynchronization therapy on mortality in heart failure," *European Heart Journal*, vol. 27, no. 16, pp. 1928-1932, 2006.
- [2] E. Lau, "Achieving permanent left ventricular pacing-options and choice," *Pacing Clin. Electrophysiol*, vol. 32, no. 11, pp. 1466-1477, 2009.
- [3] G. Lin, N. Anavekar, T. Webster, R. Rea, D. Hayes and P. Brady, "Long-term stability of endocardial left ventricular pacing leads placed via the coronary sinus," *Pacing Clin. Electrophysiol*, vol. 32, no. 9, pp. 1117-1122, 2009.
- [4] A. Bulava and J. Luki, "Single-centre experience with coronary sinus lead stability and long-term pacing parameters," *Europace*, vol. 9, no. 7, pp. 523-527, 2007.
- [5] J. Meagher and P. Altman, "Stress from flexure in composite helical implantable leads," *Medical Engineering & Physics*, vol. 19, no. 7, pp. 668-673, 1997.
- [6] P. Altman, J. Meagher, D. Walsh and D. Hoffman, "Rotary bending fatigue of coils and wires used in cardiac lead design," *Journal of Biomedical Materials Research*, vol. 43, no. 1, pp. 21-37, 1998.
- [7] M. E. Helguera, J. D. Maloney, S. L. Pinski, J. R. Woscoboinik, B. L. Wilkoff and L. W. Castle, "Long term performance of endocardial pacing leads," *PACE*, vol. 17, no. 56, pp. 56-64, 1994.
- [8] A. Scheiner and T. J. Mortimer, "A study of the fatigue properties of small diameter wires used in intramuscular electrodes," *J. Biomed. Mater. Res.*, vol. 25, pp. 589-608, 1991.
- [9] P. Comte, E. Gysin and T. Baehni, "Fatigue performance of stimulating electrodes," *Biomed. Tech.*, vol. 28, 1983.
- [10] P. Altman and D. Hoffmann, "Implantable conductor flexure fatigue issues," in *18th Annu. Conf. IEEE Eng. Med. Biol. Soc.*, Amsterdam, 1996.
- [11] W. Baxter and A. McCulloch, "In vivo finite element model-based image analysis of pacemaker lead mechanics," *Med. Image Anal*, vol. 5, no. 4, pp. 255-270, 2001.

- [12] Y. Liu, W. Zhang and G. Kassab, "Effects of myocardial constraint on the passive mechanical behaviors of the coronary vessel wall," *American Journal of Physiology - Heart and Circulatory Physiology*, vol. 294, no. 1, pp. H514-H523, 2008.
- [13] Z. Zhuang, T. Tang, H. Fang, X. Zhang, W. Yang and Y. Zhao, "Finite element modeling of cardiac pacing/defibrillation lead interaction with heart," *Key Engineering Materials*, vol. 306, pp. 1271-1276, 2006.
- [14] D. Cesario, M. Shenoda, R. Brar and K. Shivkumar, "Left ventricular lead stabilization utilizing a coronary stent," *Pacing And Clinical Electrophysiology*, vol. 29, no. 4, pp. 427-428, 2006.
- [15] G. Forleo, D. Della Rocca, L. Papavasileiou, A. Di Molfetta, L. Santini and F. Romeo, "Left ventricular pacing with a new quadripolar transvenous lead for CRT: early results of a prospective comparison with conventional implant outcomes," *Heart Rythm*, vol. 8, no. 1, pp. 31-37, 2011.
- [16] B. Fuertes, J. Toquero, R. Arroyo-Espliguero and I. Lozano, "Pacemaker lead displacement: mechanisms and management," *Indian Pacing Electrophysiology Journal*, vol. 3, no. 4, p. 231-238, 2003.
- [17] I. Ramachandra, "Impact of ICD battery longevity on need for device replacements—insights from a veterans affairs impact of ICD battery longevity on need for device," *Pacing and Clinical Electrophysiology*, vol. 33, pp. 314-319, 2010.
- [18] D. Katz and T. Akiyama, "Pacemaker longevity: the world's longest-lasting VVI pacemaker," *Annals of Noninvasive Electrocardiology*, vol. 12, no. 2, pp. 223-226, 2007.
- [19] F. Horlbeck, F. Mellert, J. Kreuz, G. Nickenig and J. Schwab, "Real-world data on the lifespan of implantable cardioverter-defibrillators depending on manufacturers and the amount of ventricular pacing," *Journal of Cardiovascular Electrophysiology*, vol. 23, no. 12, pp. 1336-1342, 2012.
- [20] H. Wu, P.-A. Heng and T.-T. Wong, "Cardiac motion recovery using an incompressible B-solid model," *Medical Engineering & Physics*, vol. 35, no. 7, pp. 958-968, 2013.
- [21] H. Mond, J. Helland and A. Fischer, "The evolution of the cardiac implantable electronic device connector," *Pacing and Clinical Electrophysiology*, vol. 36, no. 11, pp. 1434-1446, 2013.
- [22] T. Cohen, *Practical Electrophysiology*, Halvern: HMP Communications, 2005.

Bibliography

- [23] D. Mohrman and L. J. Heller, *Cardiovascular Physiology*, New York: McGraw-Hill, 2006.
- [24] P. Iaizzo, "Pacing and defibrillation," in *Handbook of Cardiac Anatomy, Physiology, and Devices*, Totowa, New Jersey, Humana Press Inc., 2005, pp. 323-348.
- [25] P. Iaizzo, "Biventricular pacing for congestive heart failure," in *Handbook of Cardiac Anatomy, Physiology, and Devices*, Totowa, New Jersey, Humana Press Inc., 2005, pp. 349-359.
- [26] F. Zoppo, F. Zerbo, G. Brandolino, E. Bacchiega, A. Lupo and E. Bertaglia, "Straight screw-in atrial leads "J-post shaped" in right appendage versus J-shaped systems for permanent atrial pacing: a safety comparison," *Pacing and Clinical Electrophysiology*, vol. 34, no. 3, pp. 325-330, 2011.
- [27] N. Snow, "Elimination of lead dislodgement by the use of tined transvenous electrodes," *Pacing and Clinical Electrophysiology*, vol. 5, no. 4, pp. 571-574, 1982.
- [28] G. N. Kay, K. Anderson, A. Epstein and V. Plumb, "Active fixation atrial leads: randomized comparison of two lead designs," *Pacing and Clinical Electrophysiology*, vol. 12, no. 8, pp. 1355-1361, 1989.
- [29] T. Cohen, "Cardiac resynchronization therapy," in *Practical Electrophysiology*, Malvern, PA, HMP Communications, 2005, pp. 197-205.
- [30] H. Pürerfellner, H. J. Nesser, S. Winter, T. Schwierz, H. Hörnell and S. Maertens, "Transvenous left ventricular lead implantation with the EASYTRAK lead system: the European experience," *American Journal of Cardiology*, vol. 86, no. 9, pp. K157-K164, 2000.
- [31] J. Kautzner, L. Riedlbauchova, R. Cihak, J. Bytshik and V. Vancura, "Technical aspects of implantation of LV lead for cardiac resynchronization therapy in chronic heart failure," *Pacing and Clinical Electrophysiology*, vol. 27, no. 6p1, pp. 783-790, 2004.
- [32] R. Lane, M. Cowie and A. Chow, "Chapter 7. Pacing therapies for heart failure," in *Implantable Cardiac Pacemakers and Defibrillators: All You Wanted to Know*, Oxford, Blackwell Publishing Ltd, 2007, pp. 110-133.

Bibliography

- [33] B. Hansky, J. Vogt, H. Gueldner, B. Lamp, G. Tenderich, L. Krater, J. Heintze, K. Minami, D. Horstkotte and R. Koerfer, "Left heart pacing—experience with several types of coronary vein leads," *Journal of Interventional Cardiac Electrophysiology*, vol. 6, no. 1, pp. 71-75, 2002.
- [34] E. J. Hearn, "Chapter 11 - Strain energy," in *Mechanics of Materials 1 (Third Edition)*, Oxford, Butterworth-Heinemann, 1997, pp. 254-296.
- [35] R. F. Gibson, *Principles of Composite Material Mechanics*, New York: McGraw-Hill, 1994.
- [36] J. E. Shigley and C. R. Mischke, *Mechanical Engineering Design*, New York: McGraw-Hill Book Company, 1989.
- [37] R. C. Juvinall, *Fundamentals of Machine Component Design*, New York: John Wiley, 1991.
- [38] E. J. Hearn, "Chapter 12 – Springs," in *Mechanics of Materials 1 (Third Edition)*, Oxford, Butterworth-Heinemann, 1997, pp. 297-325.
- [39] H. Isayama, Y. Nakai, Y. Toyokawa, O. Togawa, C. Gon, Y. Ito and et al., "Measurement of radial and axial forces of biliary self-expandable metal stents," *Gastrointestinal Endoscopy*, vol. 70, no. 1, pp. 37-44, 2009.
- [40] M. Gilard, J. Mansourati, Y. Etienne, J.-M. Larlet, B. Truong, J. Boschhat and J.-J. Blanc, "Angiographic anatomy of the coronary sinus and its tributaries," *Pacing and Clinical Electrophysiology*, vol. 21, no. 11, pp. 2280-2284, 1998.
- [41] B. Genç, A. Solak, N. Şahin, S. Gür, S. Kalaycıoğlu and V. Öztürk, "Assessment of the coronary venous system by using cardiac CT," *Diagnostic and Interventional Radiology*, vol. 19, no. 4, pp. 286-293, 2012.
- [42] E. Avallone and T. Baumeister III, "3.2 Friction," in *Marks' Standard Handbook For Mechanical Engineering*, New York, McGraw-Hill, 1996, pp. 3-20 - 3-29.
- [43] A. Birley, B. Haworth and J. Batchelor, "6.8.2 Other tribological properties - friction, abrasion and wear," in *Physics of Plastics, Processing, Properties and Materials Engineering*, New York, Oxford University Press, 1992, pp. 323-326.

Bibliography

- [44] K. Ellenbogen and M. Wood, "Chapter 2 - Basic concepts of pacing," in *Basic Concepts of Pacing, in Cardiac Pacing and ICDs*, Malden, Blackwell Publishing, Inc., 2007, pp. 91-93.
- [45] D. L. Hayes and P. A. Friedman, "Chapter 1. Clinically relevant basics of pacing and defibrillation," in *Clinically Relevant Basics of Pacing and Defibrillation, in Cardiac Pacing, Defibrillation and Resynchronization: A Clinical Approach*, Oxford, Wiley-Blackwell, 2009, pp. 8-11.
- [46] H. M. Haqqani and H. G. Mond, "The implantable cardioverter-defibrillator lead: principles, progress, and promises," *Pacing and Clinical Electrophysiology*, vol. 32, no. 10, p. 1336-1353, 2009.
- [47] R. Ellis and D. Gulick, "Vector-valued functions," in *Calculus with Analytic Geometry*, Orlando, Harcourt Brace Jovanovich, Inc., 1986, pp. 658-659.
- [48] P. O'Neil, "Vector calculus," in *Advanced Engineering Mathematics*, Boston, PWS Publishing Company, 1993, pp. 837-874.
- [49] D. Montgomery, *Design and Analysis of Experiments*, New York: John Wiley & Sons, Inc., 2001.
- [50] M. DeGroot and M. Schervish, *Probability and Statistics*, Boston: Addison-Wesley, 2002.
- [51] J. Sperzel, W. Danschel, K.-J. Gutleben and et al., "First prospective, multi-centre clinical experience with a novel left ventricular quadripolar lead," *European Journal of Pacing, Arrhythmias and Cardiac Electrophysiology*, vol. 14, no. 3, pp. 365-372, 2011.
- [52] M. Biffi, L. Foerster, W. Eastman and et al., "Effect of bipolar electrode spacing on phrenic nerve stimulation and left ventricular pacing thresholds: an acute canine study," *Circulation: Arrhythmia and Electrophysiology*, vol. 5, no. 4, pp. 815-820, 2012.
- [53] D. Montgomery, "A single replicate of the 2k design," in *Design and Analysis of Experiments*, New York, John Wiley & Sons, Inc., 2001, pp. 244-271.
- [54] S. Standring, "Heart and great vessels," in *Gray's Anatomy*, London, Churchill Livingstone, 2008, pp. 959-987.
- [55] S. Garg, P. Singh, A. Sharma and G. Gupta, "A gross comparative anatomical study of hearts in human," *International Journal of Medical and Dental Sciences*, vol. 2, no. 2, pp. 170-176, 2013.

Bibliography

- [56] A. Burr and J. Cheatham, "Additional ring analyses: out-of-plane loadings: the coil clutch," in *Mechanical Analysis and Design*, Englewood Cliffs, Prentice Hall, 1995, pp. 615-618.

APPENDIX

Sample Analytical Beam Approximation Calculation

Listed below is a sample analytical beam approximation calculation from Chapter 2.

Table A-1 Coil Geometry

	Number of Filars in Coil N	Wire Diameter d_{filar} (mm)	Mean Diameter of Coil D_{mean} (mm)	Coil Pitch per Filar P (mm)
Coil A	4	0.127	0.635	0.610

Table A-2 Material Properties

Material	Young's Modulus E_{filar} (GPa)	Shear Modulus G_{filar} (GPa)
MP35N	234	81

$$I_{filar} = \frac{\pi d_{filar}^4}{64} = \frac{\pi * 0.127^4}{64} = 12.77 \times 10^{-6} \text{ mm}^4$$

$$J_{filar} = 2 * \frac{\pi d_{filar}^4}{64} = 2 * \frac{\pi * 0.127^4}{64} = 25.54 \times 10^{-6} \text{ mm}^4$$

$$\gamma = \text{Coil pitch angle} = \tan^{-1} \frac{P}{D_{mean}\pi} = \tan^{-1} \frac{0.610}{0.635 * \pi} = 17 \text{ degrees}$$

Bending Stiffness	$\beta = E_{beam} I_{beam} = N * \frac{2 \tan \gamma \cos \gamma}{\left[\frac{1}{E_{filar} I_{filar}} + \frac{\sin^2 \gamma}{E_{filar} I_{filar}} + \frac{\cos^2 \gamma}{G_{filar} J_{filar}} \right]} \quad (2-14)$
$\beta = 4 * \frac{2 \tan (17 \text{ degrees}) \cos (17 \text{ degrees})}{\left[\frac{1}{234 \times 10^9 * 12.77 \times 10^{-6}} + \frac{\sin^2 (17 \text{ degrees})}{234 \times 10^9 * 12.77 \times 10^{-6}} + \frac{\cos^2 (17 \text{ degrees})}{81 \times 10^9 * 25.54 \times 10^{-6}} \right]}$ $\beta = 2.90 \text{ MPa mm}^4$	

Appendix

$$I_{beam} = \frac{\pi d_{mean}^4}{64} = \frac{\pi * 0.635^4}{64} = 7.98 \times 10^{-3} \text{ mm}^4$$

Equivalent Elastic Modulus	$E_{beam} = \frac{N}{I_{beam}} * \frac{2 \tan \gamma \cos \gamma}{\left[\frac{1}{E_{filar} I_{filar}} + \frac{\sin^2 \gamma}{E_{filar} I_{filar}} + \frac{\cos^2 \gamma}{G_{filar} J_{filar}} \right]} \quad (2-35)$
	$E_{beam} = \frac{\beta}{I_{beam}} = \frac{2.90 \text{ MPa mm}^4}{7.98 \times 10^{-3} \text{ mm}^4} = 363 \text{ MPa}$

Torsional Stiffness	$\alpha = G_{beam} J_{beam} = N * \frac{\tan \gamma \cos \gamma}{\left[\frac{\sin^2 \gamma}{G_{filar} J_{filar}} + \frac{\cos^2 \gamma}{E_{filar} I_{filar}} \right]} \quad (2-24)$
	$\alpha = G_{beam} J_{beam} = 4 * \frac{\tan (17 \text{ degrees}) \cos (17 \text{ degrees})}{\left[\frac{\sin^2 (17 \text{ degrees})}{81 \times 10^9 * 25.54 \times 10^{-6}} + \frac{\cos^2 (17 \text{ degrees})}{234 \times 10^9 * 12.77 \times 10^{-6}} \right]}$ $\alpha = G_{beam} J_{beam} = 3.37 \text{ MPa mm}^4$

$$J_{beam} = 2 * \frac{\pi d_{mean}^4}{64} = 2 * \frac{\pi * 0.635^4}{64} = 15.96 \times 10^{-3} \text{ mm}^4$$

Equivalent Shear Modulus	$G_{beam} = \frac{N}{J_{beam}} * \frac{\tan \gamma \cos \gamma}{\left[\frac{\sin^2 \gamma}{G_{filar} J_{filar}} + \frac{\cos^2 \gamma}{E_{filar} I_{filar}} \right]} \quad (2-36)$
	$G_{beam} = \frac{\alpha}{J_{beam}} = \frac{3.37 \text{ MPa mm}^4}{15.96 \times 10^{-3} \text{ mm}^4} = 211 \text{ MPa}$

Detailed Procedure For Creating And Analyzing Model in ABAQUS Standard

ABAQUS Standard finite element software (version 12-2) was used to perform the numerical simulation. ABAQUS Standard allows surface-to-node contact to be defined and includes nonlinear effects of large displacements. The steps to create the model of contact between a lead distal shape and a straight cylindrical tube follow below.

Part Module – Lead Distal Shape

The lead is constructed of a coil but can be represented using three-dimensional beam elements with a circular cross section property. The material properties of this beam have a Young's and shear moduli that are equivalent to the coil stiffness. This removes the complexity of the multi-filar coil from the model while keeping its bending and torsional stiffness characteristics intact. The distal shape is created using three-dimensional linear beam elements (B31) that have six degrees of freedom (displacement in X, Y, Z and rotations about X, Y, Z).

The lead distal shape is wireframe geometry that can be constructed in CAD and imported into ABAQUS or it can be created in the ABAQUS CAE Part Module. The part is a straight wire with one end wrapped into a 12.7-mm diameter. In the part module, create a 3D deformable wire shape part that matches the circular distal shape geometry. Create a straight wire 150 mm long. At one end create a circular helix that has a 12.7-mm diameter with a 0.6-mm pitch that translates out of plane. At the end of the helix create straight wire 1-mm in length. The out of plane pitch of 0.6-mm prevents the beam elements from overlapping.

A technique in ABAQUS CAE to create the wire geometry is to use a solid part and then extract the wire edge and delete any extra faces or edges that are not needed. First create a solid revolved with a rectangle that has an edge with a diameter of 12.7-mm that is rotated 360 degrees with a pitch of 0.6-mm. The move sketch normal to path option should be used to create a helix. At one revolved end extrude the section 150-mm. At the other revolved end extrude the section 1 mm. Next, in ABAQUS CAE create a wire by using the shape > wire > from edge and select the edges to create the wire. Delete any faces or wires not needed. This creates the wire geometry for the distal shape.

Property Module – Lead Distal Shape

Create a profile for the circular cross-section for the beam with a diameter of 0.635 mm (Coil A mean diameter). Next, create a beam section and change the section integration to before analysis (cross section change or thinning is not expected). Select the circular profile for the beam shape and in the table add the material properties (Young's Modulus 363 MPa and Shear modulus 211 MPa). Assign this section by selecting the wireframe geometry. Finally, use the assign beam orientation and select the wireframe geometry.

Straight Cylindrical Tube – Part Module

Perfectly rigid surfaces or objects can be defined by rigid elements or, if the geometry is simple, like a tube, analytically rigid surfaces can be created. These rigid surfaces do not allow any penetration or deformation. These three-dimensional analytically rigid surfaces are created by extruding, revolving, or sweeping a two-dimensional cross section. These rigid surfaces are controlled by a reference point where boundary conditions can be applied.

Appendix

In ABAQUS CAE, for a 2-mm rigid tube create a part that is a 3D analytically rigid shape by extruding a shell. Note that the circular beam element that contacts the tube does not have a geometric diameter of 0.635-mm so the actual contact is with the beam's centerline not its outer surface. To compensate, the 2-mm rigid tube has its diameter reduced by 0.635 mm to 1.365 mm. When sketching the circle to create the rigid tube, make sure that the circle is not a single continuous segment. Circular analytically rigid surfaces cannot have an arc of more than 180 degrees, so a circular sketch with three segments (each less than 180 degrees) is adequate. The extruded length is only for visualization since the actual extruded length is infinite. Finally create a reference point for the rigid surface to apply boundary conditions by using tools > reference point. Analytical rigid surfaces do not have any properties.

Assembly Module

Create an assembly with the distal shape part and analytically rigid tube by instancing them and orientating them so that the proximal end of the distal shape lies along the axis of the tube.

Step Module

Two steps were created to allow the distal shape to be straightened and then contact the tube. In the first step, all contact surfaces are deactivated and the distal shape is straightened so it fits within the tube. The second step activates the contact surfaces and then releases the distal shape.

In ABAQUS CAE, create the first step and select general procedure type with static, general option. Turn on non-linear geometry (nlgeom) and activate the automatic stabilization with the default settings. Use the automatic incrementation and leave the default time period of 1.

Change the maximum number of increments to 1000 or more. For the second step, repeat the same settings but turn off the automatic stabilization. If automatic stabilization is left on in the final step the results can be incorrect. In the step module, create a field output request and add contact force to the default output variables.

Interaction Module

In ABAQUS CAE, the contact is defined in the interaction module. Create an interaction that only occurs in the second step and select surface to surface contact. For the master surface select the rigid tube and then for the internal faces choose the inside of the tube. For the slave surface select the slave type as node region and then select the distal shape wireframe. Accept the defaults in the form but create a contact interaction property. For the interaction property choose contact and under the options select mechanical tangential behavior friction as frictionless.

Load Module

In ABAQUS CAE, the load module is where boundary conditions are created. To rigidly hold the tube, select the create boundary condition option and create an initial mechanical displacement/rotation boundary condition. Select the reference point of the rigid tube and set all six degrees of freedom (U1, U2, U3, UR1, UR2, and UR3) to zero for all the steps. To rigidly hold the proximal end of the distal shape repeat this same procedure but select the proximal end point of the distal shape and set all degrees of freedom to zero for all the steps.

To straighten the distal shape, a boundary condition will be applied to the distal end point of the distal shape in the first step. This boundary condition only allows the distal tip to travel in

the axial direction. The rotational degrees of freedom (UR1, UR2, and UR3) are free to rotate but the degrees of freedom orthogonal to the axis (U1 and U2) are set to zero. To straighten the distal shape the distal tip has a displacement of 40-mm or greater applied to it in the axial direction (UZ). The distance can be determined by the circumference of the distal shape.

This straightening is only done in the first step. After the first step all the boundary conditions at the distal tip are deactivated and the contact is activated. Automatic stabilization is also deactivated as described in the step module. The distal end contacts the tube surface as it tries to return to its original shape which results in contact forces. Since the tube is frictionless only contact forces normal to the tube surface (or radial to the tube axis) are generated.

Mesh Module

In ABAQUS CAE, the mesh module is where parts are meshed. The analytically rigid surface does not need to be meshed. The distal shape is meshed with three-dimensional linear beam elements. The distal shape is meshed by selecting it as the object to be meshed. The part had a global seed element of 2.5 mm. To insure the mesh has elements of equal size the curvature control was deactivated. The element type was assigned and two node linear shear-flexible beam elements (B31) for ABAQUS Standard were selected. The distal shape was then meshed.

Visualization Module

After the solution has been obtained the contact force along the length of the distal shape can be obtained and plotted within ABAQUS CAE or exported to EXCEL. Create a path using tools > path > create and select edge list type and then select viewport selection. Next select

edges to be inserted into the path by feature edge and select one end of the distal shape. The path should auto select from one end of the distal shape to the other. If it does not select flip button to auto chain the entire distal shape. Next create an XY data set by selecting the created path as the source using tools > XY data > create > source path. This allows XY data to be extracted from the model along the selected path. For the model shape select deformed and use the default node path points. For the X plot values use Z distance and for the Y plot values select the last frame of the last step with contact normal force vector at surface nodes as the field output variable. The contact force can then be plotted within ABAQUS CAE or then exported to excel at this point.